Synthesis, Self-Assembly, Processing and Materials Aspects of 2,6-(Bis-pyrazolyl-pyridine) Derivatives and Their Spin Crossover Compounds

A Thesis Submitted for the Degree of

DOCTOR OF PHILOSOPHY

By

AJAY KUMAR BOTCHA

School of Chemistry
University of Hyderabad
Hyderabad-500 046

INDIA

April 2015

Dedicated to my beloved mother

DECLARATION

I Ajay kumar Botcha declared that the matter presented in this thesis is carried by me at School of Chemistry, University of Hyderabad under the supervision of Assoc. Prof. Dr. Rajadurai Chandrasekar.

In keeping with the general practice of reporting scientific observations, due acknowledgements have made wherever the work described is based on the findings of other investigators. Any omission or error that might have crept in is regretted.

(AJAY KUMAR BOTCHA)

CERTIFICATE

This is to certify that the work presented in this thesis entitled **"Synthesis, Self-Assembly, Processing and Materials Aspects of 2,6-(Bis-pyrazolyl-pyridine) Derivatives and Their Spin Crossover Compounds"** has been done by Ajay kumar Botcha, under my guidance and the same has not been carried out elsewhere for any degree.

Prof. M. Durga Prasad
Dean
School of Chemistry
University of Hyderabad
Hyderabad 500 046

Assoc. Prof. Dr. R. Chadrasekar
(Thesis Supervisor)
School of Chemistry
University of Hyderabad
Hyderabad 500 046

Acknowledgements

I express my deep sense of gratitude and profound thanks to my thesis supervisor Assoc. Prof. Chandrasekar for his valuable guidance, patience, encouragement and for the freedom he gave me in carrying out research. His optimistic approach towards every aspect was admirable and inspiring. Throughout my Ph.D tenure, he is always approachable, helpful, friendly and extremely tolerant. I consider my association with him as a cherishable memory in my life.

I take this opportunity to thank Prof. M. Durga Prasad, Dean, School of Chemistry for providing us the facilities needed for our research. I extend my sincere thanks to former Deans Prof. D. Basavaiah , Prof. M. V. Rajashekaran and all the faculty members, School of Chemistry for their co-operation on various aspects.

I feel fortunate to have friends Nagarjuna (Chemistry), Kishore (Chemistry), Suresh (Physics), Suresh Katuri, Anad (Vizag), Ravindra (AU) and Rambabu (AU), Dr. Balu (SP lab), Dr. Santhosh (AS lab) and Ramana (RB lab) who have been my close friends over the years, for keeping me sane, giving me perspective and who have made the time more enjoyable.

It is great joy to thank my lab mates Dr. N. Chandrasekar, Dr. Supratim Basak and Dr. Pramithi, Nrayana, Krrishna, Ramudu, Radhika, Anjana for their help, pleasant company and cooperation during my Ph.D. tenure. From the bottom of my heart I thank to my friends Dr. Supratim Basak, Dr. Pramiti Hui, for their support throughout the tenure. Without their help and encouragement it is not possible to complete the work. I wish to thank my junior Mr. Narayana for his help when I am in need.

I would like to thank all the non-teaching staff of the School of Chemistry for their cooperation on various occasions, especially, I thank to Bhaskar garu (LCMS operator), Satyanarayana garu (NMR technician), Parveige (FTIR madam) Durgaprasad Anna (TEM operator), Pavan Garu (SEM operator), Haritha garu (UV-visible and florescence instruments in charge).

I would like to acknowledge Prof. A.V. Prasada Rao, Prof. G.Nageswar Rao, Prof. Sivarao, Prof. Vani and N. Murty sir during my post graduation at Andhra University, Visakhapatnam.

My special thanks to Jagruti-coaching center teacher Prof. Jaya Prakash, at Narayanaguda. I take this opportunity to thank all my school, college and PG teachers, Sivinnaidu (Science teacher), Manmadharao (Social teacher), Chiranjeevi (Maths teacher), Srinu Sir (Intermediate), Namaalwar Sir (degree), Satyam Narayana Sir (PG).

I am lucky enough to have support of my friends from School of Chemistry Dr. D.K Srinivas, Shesadri, Venu, Rama Krishna, Sudha Rani, Madhu, Krishna (SKD lab), Prabhu, Nagaraju, Srinuvasa Rao, Sanyasi Naidu, Sridevi akka, Dr. Banu, Dr. Mallesh, Dr. Ramu Yadav, Dr. M. Ramu, Satish Anna, Dr. Saikath (GM), Dr. Phani Pavan, Dr. Ramesh, Dr. Rambabu, Dr. Vignesh, Dr. Ganesh, Dr. Vijji, Chandu, Suresh, Sudhansun (TJ lab), Thirupathi Reddy, Ashok, Chandu, Sowmya (AS lab), Ravindra babu, Naveen, Ganesh (Rb lab), Chari, Kishore (MGS lab), Obaiah, Satish (PKP) in helping me at various times.

I also thank my Spiritual friend, Pastor Peter Samuel, Nirupama akka, Bro. Sham Kishore, my Kodanda Ram anna, Baby akka, Ashray babu, Dr. N. Sreenivasa Rao, Rajanianna, Vijaya sister, Anil anna, Kishore anna (KP), Suguna akka, Rambabu anna, Bheem anna, Prabhu anna, Manoj, Varma, Mani, Rajesh, Nagarjuna, Kiran (Agra), Andrew Anna, Vijay, L. Kanth, Ravi Kiran, Vijay Prasad Anna, Johnson, Benhur, Eswar, Neelima akka, Raj kumar, Prathyusha, Aancy, Adam Anna, Anil , Rajesh anna (staff) and Divakar Pastor for their love and spiritual support during my stay in the university of Hyderabad. My heartful gratitude to my brother Suneeth Kumar (Save A Child Founder) and sisters Ruth, Shalomi, Swaroopa, Pragathi, Samuel.

I also thank to family friends Ramakrishna, Sekhar, Jagadeesh, Rajesh, Bhaskar, Suresh, Shankar, Siva Krishna, Satyam Narayana, Thinadhi Swamy, Appa Rao, Raju Penki, Srinu karra and Manmadha Rao for their encouragement during my research.

I am pleased to show my gratitude to my family members and relatives Amma, Dad, Aunt, Sisters (Laxmi Sujatha, Neelima,), brothers (Vijay, Uday, Vinay), Venkat Rao Bava, Aadinarayana Bava, Paramanandam bava family, Kala akka family, Kamala and Narayana akka family, muddhulu mamayya family, Chinna Rao mamayya family, Appa Rao chinnanna family, Prasad Annaya family.

Ajay Kumar Botcha

LIST OF ACRONYMS

μL	Microlitre
μm	Micrometer
μM	Micromolar
^{1}H	Proton
TEM	Transmission electron microscope
AFM	Atomic force microscope
Å	Angstrom
$CDCl_3$	Deuterated chloroform
CH_2Cl_2	Dichloromethane
CH_3CN	Acetonitrile
$CHCl_3$	Chloroform
°C	Degree centigrade
cm	Centimeter
cm^{-1}	Wave number unit
CT	Charge transfer
CuI	Copper iodide
CW	Continuous wave
D	Deuterium
DCM	Dichloromethane
DDQ	2, 3-Dichloro-5,6-dicyano-1,4-benzoquinone
DMF	Dimethylformamide
DMSO	Dimethyl sulfoxide
TGA	Thermo gravimetric analysis
EBL	Electron beam lithography
EDTA	Ethylenediaminetetraacetic acid
EDXS	Energy dispersive x-ray spectroscopy
EtOH	Ethanol
$Eu(tta)_3$	tris[4,4,4-trifluoro-1-(2-thienyl)-1,3-butanediono]europium
$Fe(ClO_4)_2$	Iron perchlorate
FESEM	field emission scanning electron microscope
FRET	Forster resonance energy transfer
h	hour
H_2O	Water
HRTEM	High resolution transmission electron microscope
Hz	Hertz
hυ	Light
IR	Infrared
ISC	Intersystem crossing
K	Kelvin

K_2CO_3	Potassium carbonate
K Da	kilo dalton
KOH	Potassium hydroxide
KBr	Potassium bromide
LB	Langmuir-Blodgett
LCW	Lithographically controlled wetting
LED	Light emitting diode
LiBr	Lithiumbromide
lm W^{-1}	Lumens per watt
LPEF	Long pass edge filter
M	Molar
M.P	Melting temperature
MeOH	Methanol
mg	Milligram
MHz	Megahertz
MIMIC	Micro moulding in capillaries
mL	Millilitre
*M*n	Number average molecular weight
MSP	Metallo-supramolecular polymers
*M*w	Weight average molecular weight
NEt_3	Triethylamine
nm	Nanometer
nM	Nanomolar
NMR	Nuclear magnetic resonance spectroscopy
ns	Nanosecond
Oe	Oersted
ONRs	Organic nanorods
$Pd(PPh_3)_4$	tetrakis(triphenylphosphine)palladium (0)
PEG	Polyethylene glycol
PL	Photoluminescence
PS	Polystyrene
PPh_3	Triphenylphosphine
PVD	Physical vapor deposition
PDMS	Poly(dimethylsiloxane)
RPM	Revolutions per minute
RT	Room temperature
SAED	Selected area electron diffraction
SAMs	Self assembled monolayers
SCO	Spin crossover
SEM	Scanning electron microscope
SERS	Surface-enhanced Raman spectroscopy
SPR	Surface plasmon resonance
ST	Spin transition

STM	Scanning tunneling microscopy
ST-NPs	Spin transition nanoparticles
T	Temperature
t	Time
TEM	Transmission electron microscope
Terpy	Terpyridine
TGA	Thermogravimetric analysis
THF	Tetrahydrofuran
$T_{1/2}$	Spin transition temperature
UV	Ultraviolet
UV-Vis	Ultraviolet-visible
WOLED	White organic light-emitting diode
WPLED	White polymer organic light-emitting diode
X_n	Number-average degree of polymerization
$Fe(ClO_4)_2$	Ironperchlorate
Δ	Heat
δ	NMR chemical shift reported in ppm
Δλ	Change in wavelength of emission or absorption
λ	Wavelength
λ_{max}	wavelength of emission or absorption maximum
π-π	pi-pi
χT	Molar magnetic susceptibility

CONTENTS

Declaration I
Certificate II
Acknowledgements III
List of Acronyms V

Chapter 1 Introduction

1.1 Introduction to nanoscience and nanotechnology 1

1.2 Methods for fabrication of nanomaterials 2

1. 2. 1 Top-down approach 2

1.2.1.1 Lithographic controlled wetting (LCW) 3

1.2.1.2 Micro transfer molding (μTM) 3

1.2.1.3 Micromolding in capillaries 4

1.2.1.4 Photolithography 4

1.2.2 Bottom-up approach 5

1.3 Self-assembly 7

1.3.1 van der Waal forces 7

1.3.2 Hydrogen bonding 8

1.3.3 π-π interactions 10

1.3.4 Solvophobic forces: Hydrophobic effect 11

1.4 Nanomaterials 12

1.4.1 Zero-dimensional (0-D) materials 13

1.4.2 One-dimensional (1-D) materials 13

1.4.3 Two-dimensional (2-D) materials 13

1.4.4 Three-dimensional (3-D) materials 13

1.5 Spin-crossover phenomena 13

1.5.1 Definition 13

1. 5. 2 Spin crossover nanoparticles (SCO NPs) 15

1. 5. 3 Spin crossover curves 17

1. 5. 4 Spin crossover coordination polymers and fabrication 18

1. 5. 5 Light induced excited spin state trapping (LIESST) effect 20

1. 5. 6 Entropy changes upon spin-crossover 21

1. 5. 7 Fabrication of spin-crossover (SCO) materials 22

1.6 Gold nanoparticles (Au NPs) 23

1.6.1 Introduction 23

1.6.2 Surface plasmon resonance (SPR) 25

1.6.3 Surface enhanced Raman sacttering from hot spots 27

1.6.4 Optical properties of metal nanoparticles (NPs) 28

1.7 Optical waveguides 28

1.7.1 Active waveguides 29

1.7.2 Passive waveguides 30

1.8 Drug delivery 31

1.8.1 Drug carriers *31*

1.8.2 Vesicles as drug carriers 32

1.8.3 Zebrafish organism model for the drug assessment 33

Overview of the thesis 35

References 37

Chapter 2 **Lithographically oriented 1D nano-tape arrays composed of solution processable above room temperature spin cross-over iron(II) coordination polymers**

2.1 Abstract 49

2. Introduction 50

2.3 Results and discussion 51

2.3.1 Synthetic scheme 51

*2.3.2 Synthetic procedure of **1*** 51

*2.3.3 Absorbance and emission studies of **L** and **1*** 51

*2.3.4 Spin crossover behaviour and variable temperature Raman of **1*** 52

2.3.5 Fabrication of SCO nanotapes and their characterization 54

2.3.6 Preparation and characterization of PDMS mould by microscopic techniques 55

2.3.7 Fabrication of 1-D array SCO nanotapes 56

2.4 Conclusions 57

References 57

Chapter 3 **Optical wave guiding organic Nanorods coated with reversibly switchable Fe (II) spin crossover Nanoparticles**

3. 1 Abstract 59

3. 2 Introduction 60

3. 3 Results and Discussion 61

*3.3.1 Synthetic procedures of **2** and **3*** 61

3.3.2 Synthesis and fabrication of ONRs coated with SCO-NPs 62

3.3.3 Confocal micro-Raman Spectroscopy/ Wave guiding Studies 63

3.3.4 Spin crossover studies 64

*3.3.5 Waveguiding properties ONRs coated by SCO-NPs (**3**)* 65

3.4 Conclusions 66

References 66

Chapter 4 **Synthesis of gold nanoparticles stabilized by novel thiol functionalized Fe (II) complex to study spin crossover effect through plasmonic propagation**

4. 1 Abstract 69

4. 2 Introduction 70

4. 3 Results and Discussion 71

4.3.1 Synthetic scheme 71

4.3.2 Synthesis 71

4.3.3 Brust-Schiffrin two phase method in attaining thiol Au NPs 72

4.3.4 ^{1}H-NMR spectroscopy studies 72

*4.3.5 UV-Visible spectroscopic studies for of **L4** and **10*** 73

*4.3.6 Determination of composition of **L4** by TGA* 74

*4.3.7 TEM studies of thiol capped Au NPs (**L4**) and its Fe(II) complex (**10**)* 74

*4.3.8. Magnetic properties of **10*** 76

*4.3.9. Fabrication of rectangle micro stripes by **10*** 77

4.4 Conclusions 79

4.5 Synthetic procedures 79

References 87

Chapter 5 **Organic nano-vesicular cargoes for drug delivery: synthesis, vesicle formation, controlling "Pearling" states and terfenadine loading/release studies**

5.1 Abstract 89

5.2 Introduction 90

5.3 Synthetic scheme of L5 91

5.4 Results and discussion 92

*5.4.1 Synthesis of bolaamphiphile **L5*** 92

5.4.2 Variable temperature of ^{1}H-NMR 92

*5.4.3 Investigation of Nanostructures of **L5*** 93

5.4.4 Zebrafish Studies 95

5.4.5 Control over nanostructure using stabilizing agents 96

5.4.5.1 Synthesis of nanovesicles stabilized by PEG-400 97

5.4.5.2 Synthesis of nanovesicles stabilized by PEG-2000 97

5.4.6 Synthesis of TFN-loaded stabilized nanovesicles 98

5.4.7 Determination of concentration of TFN in surrounding media 98

5.4.8 Determination of concentrations of TFN inside anoveicles 99

5.4.9 UV-Visible spectroscopy for determination of unknown drug concentration 100

5.4.10 Stability of drug loaded nanovesicles 101

5.4.11 Protocol for Zebrafish treatment with TFN-loaded nanovesicles 102

5.4.12 Sustained drug delivery of TFN-Loaded nanovesicles in Zebrafish larvae 102

5.5 conclusions 103

5.6 Synthetic procedures 104

References 109

***Chapter 6* Conclusions**

Conclusions 111

Appendex A (materials) 113

Appendex B (Instrumentation) 114

Appendix C (Research publications and Conferences) 116

Presentations in Conferences and symposiums 117

CV 119

1.1 Introduction to nanoscience and technology:

The study of molecular nanomaterials is one of the budding areas of nanoscience and technology. The word "nano" evolved from Greek language and it represents physical length scales that are in the order of a billionth of a meter. Characteristic size of nanomaterials is in the order of 1-100 nm. Study of nanoscale materials has attracted considerable attention of scientists working in topics ranging from physics to chemistry to biology and engineering etc., and it is a highly inter-disciplinary area which connects between chemistry, physics, electric, chemical and mechanical engineering and so on.[1] Nanoscience and technology has emerged as an important discipline in the last decades, a renowned American physicist Richard Feynman discussed the possibility of direct manipulation of individual atoms in his famous talk called "*There is Plenty of Room at the Bottom*" delivered at Cal Tech in 1959.[2] In 1986 K. Eric Drexler, took Feynman concept and independently used the term *nanotechnology* in his book "*Engines of creation: The Coming Era of Nanotechnology*".[3] He founded the foresight institute to bring the understanding and awareness in the public about concepts of nanotechnology. Most of the properties of solids will change if their dimension reaches nano domain. Let us consider a particle of $1\times1\times1$ nm^3. This contains approximately 64 (4^3) atoms, 8 of them lie at interior of the particle and 87% (~56 atoms) of atoms lie on the surface of the particle. This is because of increasing the surface to volume ratio of nanostructure over bulk materials which provides the incredible change in the electronic, magnetic, chemical, and mechanical properties of nanomaterials as compare to bulk state. Some natural biological and manmade structures are shown in *Figure 1* with respect to their dimensions. Lot of applications can be realized from nanoscience and technology in all areas of science such as drug delivery, catalysis, sensors, luminescent materials, non-linear optics (NLO), photonics, bio-labelling and functionalization, super density data storage etc. Various sizes of materials and insects were demonstrated clearly in *Figure 1.1* from 2 nm to 0.1 m. Various methods will be discussed in subsequent sessions to fabricate nanomaterials.

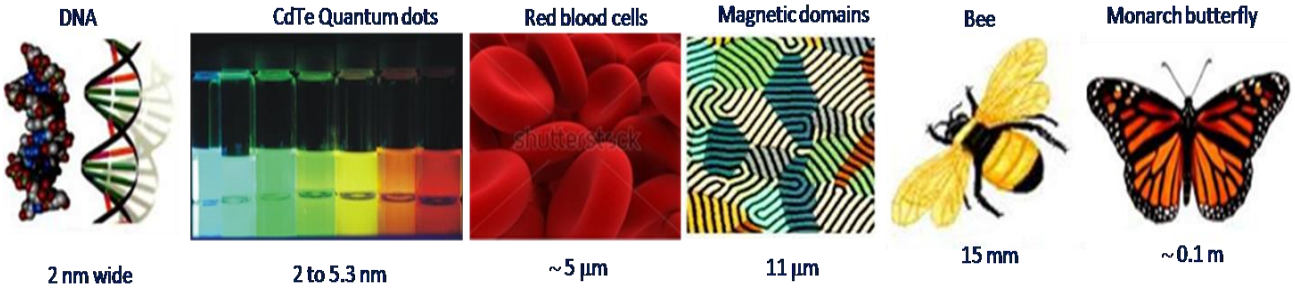

Figure 1.1*: Schematic representation of the dimensions biological and manmade structures.*

1.2 Methods for fabrication of nanomaterials:

Fabrication methods of nanomaterials are classified into two types based on the way of assembly of atoms or molecules within in the system as mentioned below.

- Top down approach and
- Bottom up approach

1.2.1 Top-down approach:

Generally breaking down a large piece of a material to achieve nanostructure is known as top-down approach. This method was introduced as new manufacturing tools to solve industrial problems such as micro electro mechanical devises.[4] Basically this strategy impose structure or pattern on various substrates like a rubber stamp. One of the best examples of the top-down fabrication method is photolithography silicon technology,[5, 6] which was essentially developed for microelectronics (integrated circuits planar technology) but now it is also used to make miniature machines, three dimensional structures by exploiting the preferential material-etching along the silicon's crystallographic planes.[7, 8] In 1947, this revolutionary fabrication process initiated with the invention of the point-contact transistor that raised the area of microelectronics.[9] Since then, the industry has been led by the demand to make devices that squeeze an ever increasing number of circuit elements onto ever smaller pieces of semiconductor materials.[10] Lithographic techniques such as ionic, x-ray and electronic lithography can be used for making master stamp which will be useful for making desired nanostructure via poly(dimethylesiloxane)(PDMS). Masters of dimension 10-100nm can be reached by means of X-ray lithographic technique.[11] To prepare replica of master stamp on PDMS, a mixture of PDMS (90%) and curing reagent (10%) is poured on master and heated at 60°C at least for 3h. Composite is released from master by cutting around the pattern with razor blade.[12] In addition to advantages in top-down methods, few drawbacks also associated with it

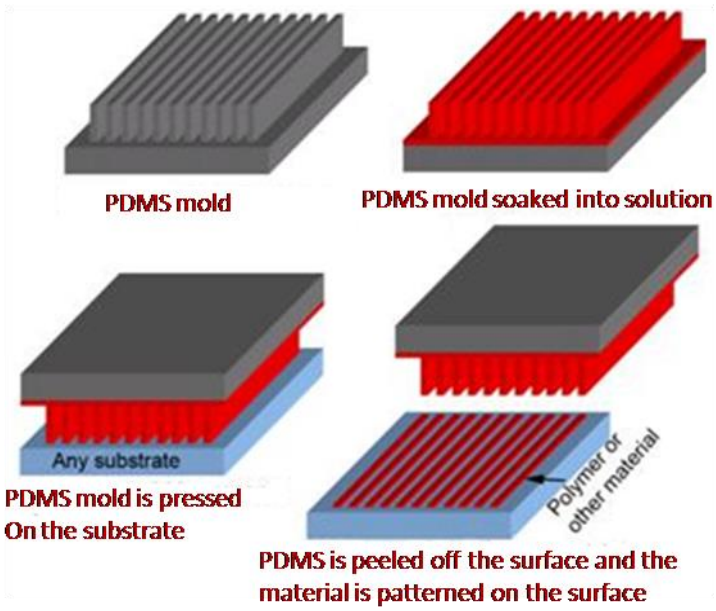

***Figure 1.2**: Lithographic controlled wetting method.*

such as cost, difficulties in nanoscale resolutions.[13]

1.2.1.1 Lithographic controlled wetting (LCW):

In this approach, the molding area of the PDMS stamp is soaked in solution of the any desired material needs to be patterned or printed. Later PDMS is carefully stamped on various surfaces or substrates to make pattern of desired compound or material. After evaporating the solvent, PDMS mold is peeled off watchfully, to achieve uniform shaped pattern on the glass surface as depicted in the *Figure 1.2*.

1.2.1.2 Micro transfer molding (μTM):

In this methodology,[14] a drop of liquid pre-polymer is applied to the clean surface of PDMS mold and excess liquid can be removed by scraping with flat PDMS block. Then the resultant mold is placed in contact with substrate followed by heating for solidification. After solidification, the PDMS mold is peeled off carefully to make a good patterned microstructure on the surface. The scanning electron microscopy (SEM) images of typical of polymer structures that were fabricated by μTM is shown in *Figure 3.* μTM molding has capability to generate both inter connected and isolated microstructures of polyurethane (PU) (*Figure 1.3A*). One of advantages of this method over micro lithographic technique is fabrication of microstructures on nonplanar surfaces, this characteristic is very important to build 3-D microstructures layer by layer. *Figure 1.3B* shows an array of parallel lines of micro posts made from thermally curable epoxy resins in. *Figure 1.3C* reveals a continuous polymeric web fabricated over separated polymer lines. *Figure 1.3D* shows a three-layer structure of epoxy fabricated by μTM on a glass slide.

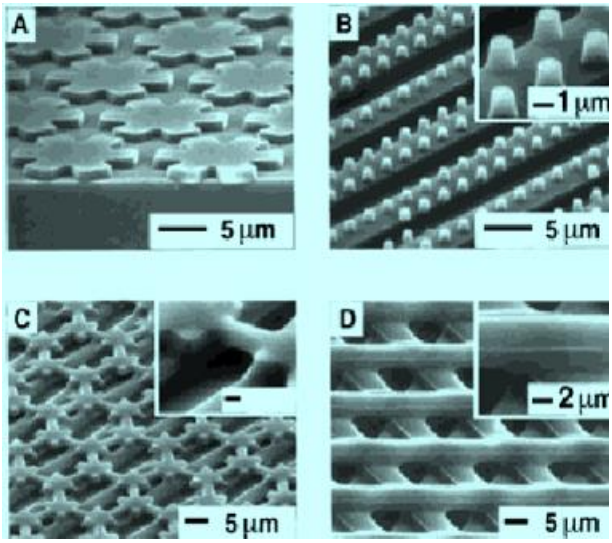

***Figure 1.3**: SEM images of polymeric microstructures fabricated by μTM technique: A) patterned, isolated microstructures of PU on silver (one layer); B) isolated microcylinders of epoxy on 5-mm lines of epoxy supported on a glass slide (two layers); C) a continuous web of epoxyover a layer of 5-μm lines of epoxy supported on a glass slide (two layers); D) a three-layer structures on a glass slide made from a thermally curable epoxy. Adopted from Ref. 15.*

Potential applications of this μTM technique is in the area of integrated optics,[15] tissue engineering,[16] applied optics[17] to achieve two and three-dimensional microstructures. By

using μTM, we can generate microstructures over relatively large areas (~3 cm^2) within a short period of time approximately 10 minutes. This methodology is also used to fabricate optical waveguides, interferometers and couplers from organic polymers.[18]

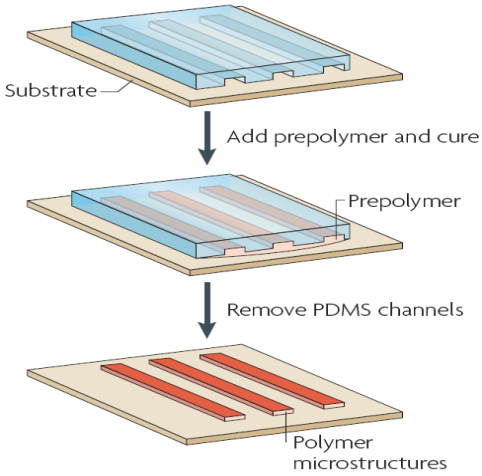

***Figure 1.4**: Lithographic micromolding technique. Adopted from ref. 19.*

1.2.1.3 Micromolding in capillaries:

Micromolding in capillaries (MIMIC) is a another non-photolithographic technique which can form complex micro structures on planar surfaces as well as on curved surfaces.[19] In this method, first PDMS mold will be placed on the surface of substrate to make contact with surface of substrate, then when we place low-viscous polymer liquid at the one end of the empty channel of PDMS mold on the surface, spontaneously liquid flows from one end to other end of that of empty channels due to capillary action. After curing the polymer into solid by heating at required temperature, PDMS mold can be removed carefully (*Figure 1.4*). Different types of materials are used in this method, for instance, pre polymers that are curable with either by thermal or UV light,[20] precursors to carbons[21] or ceramics,[22] structural and functional polymers,[23, 24] colloids,[25] polymer beads,[26] inorganic salts,[27] biological macromolecules[28] and sol-gel materials.[29]

Material fabrication based on MIMIC is remarkable for its simplicity and its fidelity in transferring the patterns from the mold to the polymeric structure that it forms. MIMIC makes patterned structures in a single step, and patterning structures with various thicknesses can be possible. Of course MIMIC does have so many limitations: (a) It can't form isolated structures (b) the rate of filling over a large distance decreases remarkably due to the viscous drag of the liquid in the capillary. (c) Extremely slow filling of small capillaries may limit the usefulness of MIMIC in various types of nanofabrication.[30, 31] (d) when hydraulic drag is high, forward ends of capillaries may fill incompletely.[32]

1.2.1.4 Photolithography:

Photolithography is a main pillar in the IC and semiconductor companies.[33-42] This technique has been used for pattern generation in making of microchips, ICs and commercial MEMS devices. Photolithography uses an exposure of a light-sensitive polymer (photo resist) to UV light to define a required pattern. Initially, UV light of wavelength is irradiated through a photo mask that consists of opaque features of a transparent substrate (glass or quartz) to create a exposure on a

photo-resist that is coated on a substrate. At the exposed area, the polymer chains of photo-resist break down yielding in good soluble chemical solution called developer. Furthermore the exposed photo-resist is removed in a developer to form the targeted photo-resist pattern. Patterned photo-resists are used as a protective layer in subsequent etching or deposition processes to build topography on the substrate.

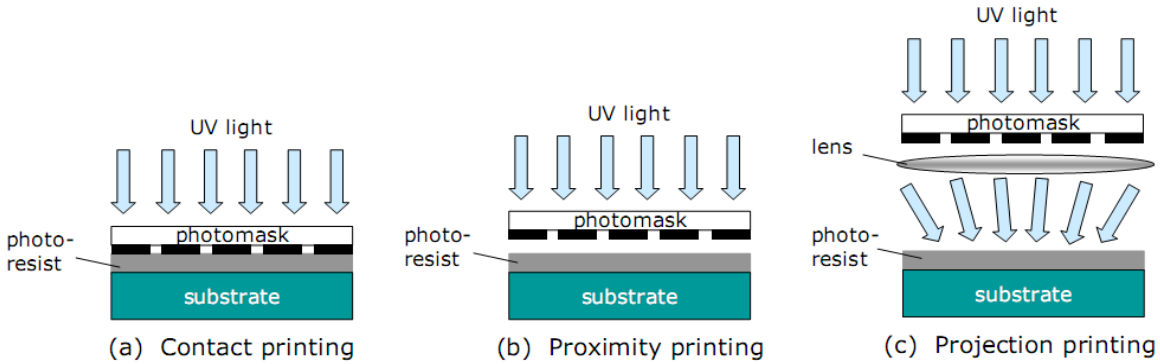

***Figure 1.5**: Schematic illustration of three forms of photolithography: (a) contact printing; (b) proximity printing; and (c) projection printing. Adopted from ref. 33.*

There are three types of photolithography: Contact printing, proximity printing and projection printing as shown in *Figure 1.5*. Photo mask will be in contact with photo-resist in both contact and proximity printing techniques. These both approaches make patterns as small as few microns, accordingly, they are generally used in the fabrication of moderate-resolution patterns, especially in laboratories and small to medium-sized companies. In the most of the research works generally refers to contact and proximity printings. Conversely, projection printing system uses an optical lens system to project a deep-UV pattern from an excimer laser on the photo-resist enabling pattern-size reduction by 2-10 times. Projection printing system has the ability to fabricate high-resolution patterns as small as a few tens of nanometers[43] at a high throughput rate.[44] However; this method requires the use of sophisticated optical-lens and precise temperature controllers resulting in increasing cost and thus utilized to manufacture advanced ICs and CPU chips.

1.2.2 Bottom-up approach:

In this approach nanostructures covering large area is built from the precursors in the solid, liquid, and gas phase employing either physical or chemical deposition processes,[45] this method is opposite to bottom up approach. Molecular interactions such as hydrophobic, hydrophilic, hydrogen bonding, Coulomb and van der Waals forces are all responsible over self-organizing structures in bottom up approach.[46] Self-organization normally renders just the local structures, to fully exploit the opportunities delivered by the self-organized nanostructures and get materials

with directional properties at different scales, An additional interactions and mechanisms like hydrophobic interaction and hydrogen bonding that promote phase separation,[47] topographically patterned surface,[48] tailored substrate chemistry[49] and electrical fields[50] are also very useful. Bottom-up approach starts with well-defined molecular species which undergo certain processes in making nanostructure as shown[51] in the *Figure 1.6*. They are many bottom-up methods were developed for the production of nanomaterials such as self-assembly, sol-gel processing, laser pyrolysis, bio-assisted synthesis, flame spraying synthesis, electroplating, supercritical fluid synthesis, and atomic or molecular condensation etc.[52]

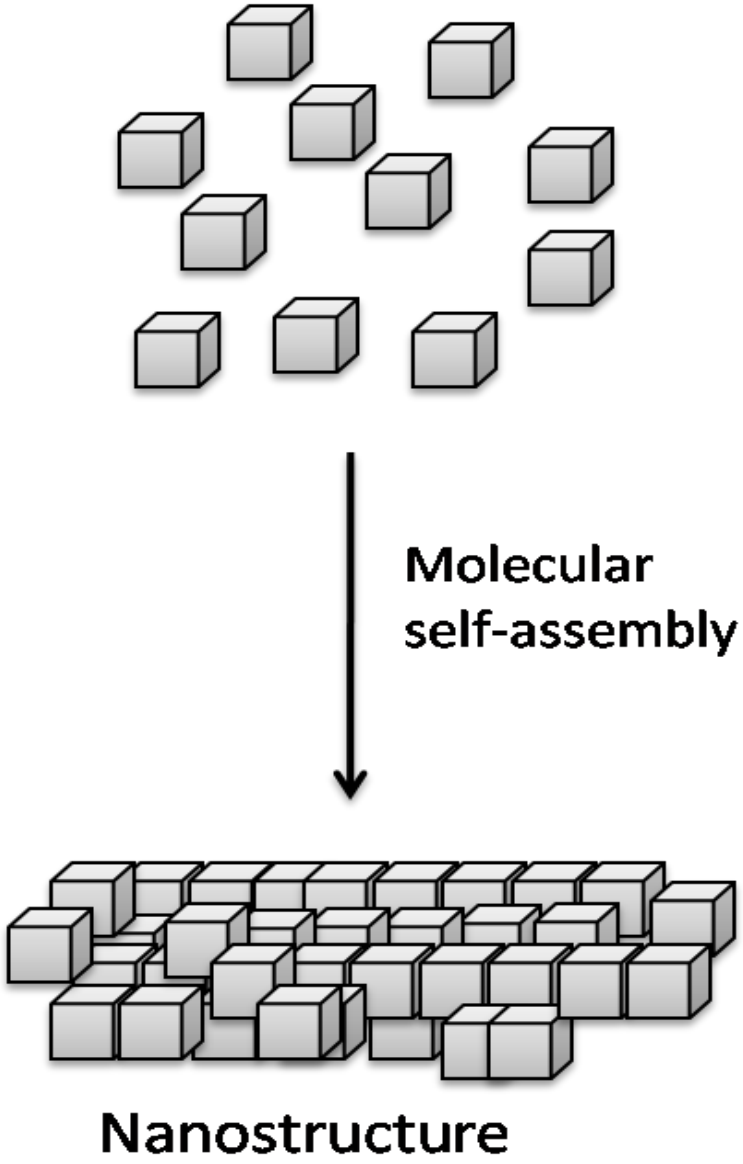

Figure 1.6*: Fabrication of a nanostructure via bottom-up methodology.*

1.3 Self-assembly:

Self-assembly is a natural phenomenon, in 400 BC the Greek philosopher Democritus speculated that universe evolved from the organization of atomistic components to yield solar system, Earth, stars and galaxies.[53] Two millennia later the French philosopher Descartes envisioned an uniform universe arising out of chaos based on natural laws via the organization of small objects into larger objects. The words of Democritus and Descartes appear to be tantamount with current thinking about self-assembly. Self-assembly is bottom-up method in which well-ordered structures will be made at nanometer scale.[54-56] Self-assembly normally occurs via reversible interactions that gradually arrange into the most thermodynamically favored nanostructure.[57] The Chemistry of complex non-covalent structures at nanoscale and the concept of "supramolecular chemistry" began by the study of different organic polymers and host-guest chemistry that was depended on advanced organic chemistry. The pioneering work of Jean-Marie Lehn who introduced the term supramolecular chemistry, is directed towards the engineering of molecular crypt and cages with expected shape whereby only some kind of molecules was allowed to be lodged in the cage[59, 60]. In 1987 Lehn received Noble Prize in Chemistry with Donald Cram and Charles Pedersen for supramolecular chemistry.

1.3.1 van der Waal forces:

According to IUPAC definition, van der Waals is the sum of the attractive or repulsive forces between molecules (or between parts of the same molecule) other than those due to covalent bonds, or the electrostatic interaction of ions with one another, with neutral molecules, or with charged molecules. The interactions can be between two permanent dipoles (Keesom force), between induced dipole and permanent dipole (Debye force), and between induced dipole-induced dipoles (London dispersion forces). These are weaker than all other intermolecular interactions such as dipolar-dipolar, ionic, hydrogen bonding and hydrophobic interactions. According to Schrodinger wave equation and

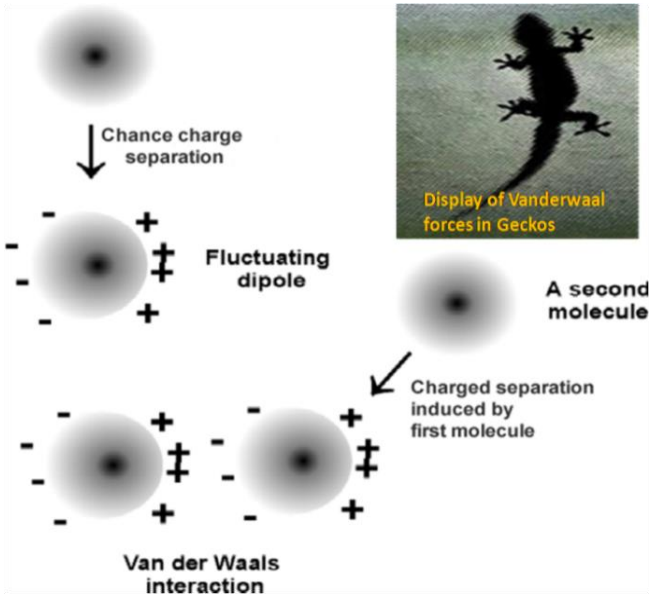

***Figure 1.7**: Display of rising vander Waals interaction, inset shows a Gecko climb trees or wall utilizing vander Waals forces.*

Heisenberg's uncertainty principle, an electron can be anywhere in the orbital. So there is probability of charge separation within the atom, this makes neutral atom or molecule as temporary dipoles such a way that atoms or molecules attract each other momentarily as mentioned in the *Figure 1.7*. van der Waals force can also be strong; for instance, Geckos can run and climb on any kind of surfaces due to micro and nanoscale high aspect ratio beta-keratin structure at their feet. The adhesion of Geckos at any kind of surface is mainly due to van der Waals forces. These interactions also plays well role in adsorption of noble gases (Ar, Kr, Xe) on metal surfaces like Pt(111), Pd(111), Cu(111) and Cu(110).

1.3.2 Hydrogen bonding:

Hydrogen bond is a weak electrostatic chemical bond between covalently bonded hydrogen atom and a more electronegative atom with a lone pair of electrons. Life will be impossible without the concept of hydrogen bonding.[61] Pauling, in his book on Nature of the chemical bond, said that hydrogen bonding is electrostatic but not covalent. The phenomenon of hydrogen bonding has been convinced by chemists, physicists, material scientists and biologists. Several books are available on hydrogen bonding[62, 63] starting with the first influential book introduced by Pimentel and McClellan in 1960. It is obvious that the study of hydrogen bonding came into reality before 1920. Hydrogen bond is combination of donor and accepter groups, usually more electro negative atoms like F, O, N act as accepters whereas hydrogen atom bonded with more electronegative atom acts as donor. It has been recognized that hydrogen accepter can be any

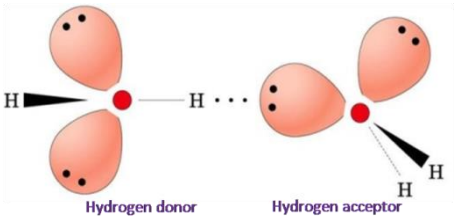

***Figure 1.8**: Simple model for hydrogen bonding by two water molecules.*

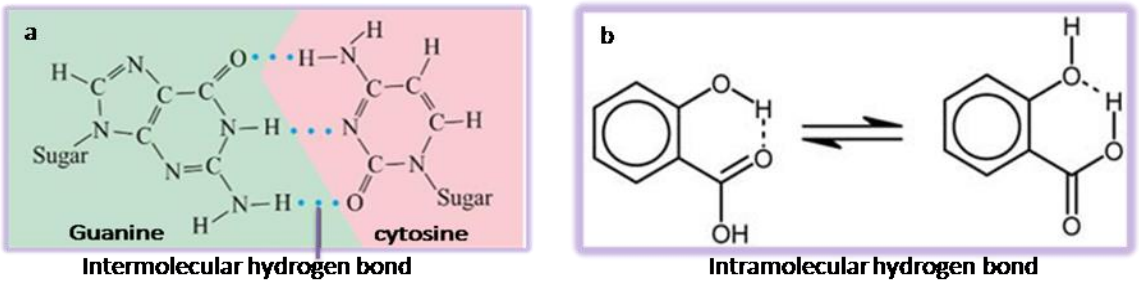

***Figure 1.9**: Intermolecular hydrogen bonding between guanine and cytosine (a), intermolecular hydrogen bonding in salicylic acid (b). Adopted from ref. 65.*

element[64] (F, N, O, C, P, S, Cl, Br, I and Se) having electronegative more than that of hydrogen atom. Hydrogen bonding is classified into two types based on nature of the bonding; those are

intermolecular and intermolecular in nature. Intermolecular hydrogen bonding occurs between two molecules where as in the case intermolecular hydrogen bond, donor and acceptor should be present within one molecule.

Double helix structure of DNA molecule is mainly due to presence intermolecular hydrogen bonds between nucleic bases adenine-thymine and guanine-cytosine. Numerous of literature is available regarding intra molecular hydrogen bonding; one of the simplest models is salicylic acid. Two resonance structures of salicylic acid possessing hydrogen bonds within one molecule as showed in the above *Figure 1.9*.[65] Hydrogen bonds within the molecules can be characterized by few techniques such as FTIR, NMR, Raman, UV and microwave spectroscopy.[66] Moreover today modern spectroscopic techniques like 2D-IR and double techniques (IR-UV, UV-UV)[67] are used to investigate the hydrogen bonded systems. In the process of self-assembly of molecules, hydrogen

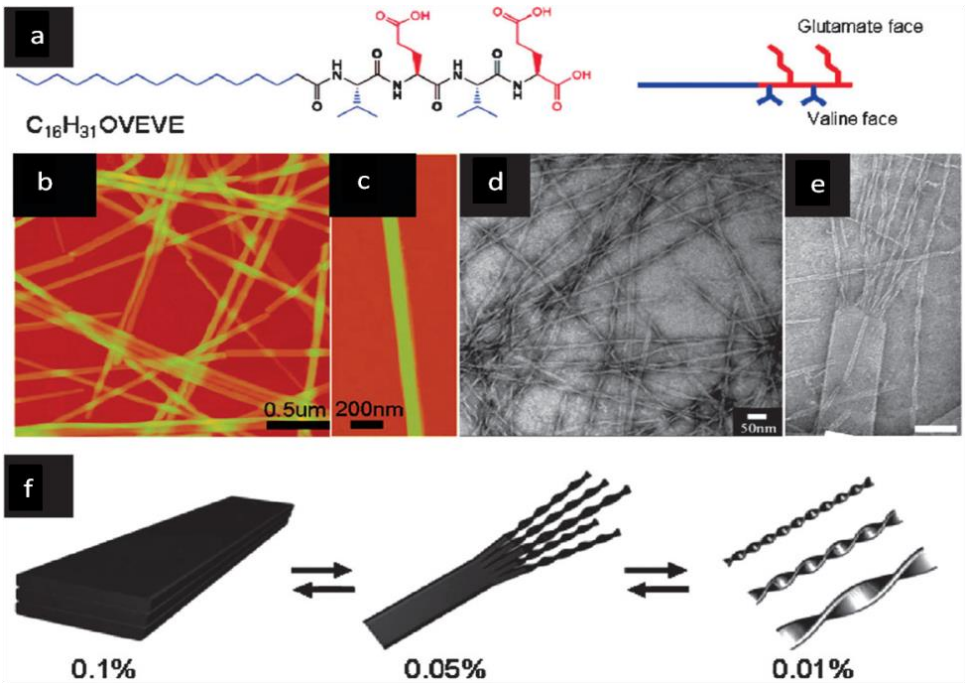

***Figure 1.10**: a) Chemical structure of peptide amphiphile, (b)(c) AFM images of nanobelts at different scan sizes, (d) TEM image of nanobelts and twisted nanoribbons, (e) EM image of twisted nanoribbons sprouting from nanobelt, (f) Growth of nanobelt and nanoribbons depending on concentration. Adopted from ref. 69.*

bonds play a vital role in order to attaining stable nanostructures. For example, the nano/micro bottom-up fabrication of peptides and polypeptides produces different kinds of structures such as tubes, fibres, ribbons, wires, vesicles and spheres[68] etc. A peptide amphiphile[69] self-assemble at different concentrations to produce three types of nanostructures such as nanobelt, nanoribbons, and twisted ribbons. Nanobelts are observed at a concentration of 0.1 wt%, twisted nanoribbons

sprouting from one nanobelt at 0.05 wt% and further reduction of concentration up to 0.01 wt% produced twisted nanoribbons as shown in *Figure 1.10*. It is easy to design and synthesize short peptides to use them as good model systems for investigating biological self-assembly. Different types of self-assembling peptides via hydrogen bonding[70] show considerable potential for a number of applications, including drug delivery, biological surface engineering and scaffolding tissue repair in tissue in regenerative medicine.

1.3.3 π-π interactions:

π-π interactions are non-covalent interactions which often occurs in π conjugated aromatic compounds, the reason behind π-π interactions are quadruple moments within conjugated system. In case of simple systems like benzene, sp^2 carbons are more electronegative than hydrogen atoms. In benzene more electron density lies on carbon while less electron density on hydrogen. Quadruple moments arises in such a way that over all dipole moment of the whole system would be zero and quadruple moments of benzene are given in *Figure. 1.11*. π-π interactions also depend on substituent which is attached to the aromatic ring.[71] Electron withdrawing substituent on ring favors sandwich kind of face to face interactions, In contrast, electron donating groups allows the T shape π-π stacking. For simple benzene molecule, three types of possible π-π interactions were depicted in the *Figure 1.12*. Particularly polycyclic aromatic hydrocarbons are relevant in making π-π interactions, for instance, stacking for hexabenzo-coronene on graphene sheet (*Figure 13A*).[72] Noncovalent interactions display important role in supramolecular chemistry, biochemistry and material science.[73]

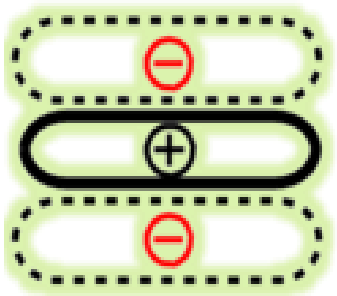

***Figure 1.11**: Polarization of electron cloud in benzene. Adopted from Wikipedia.*

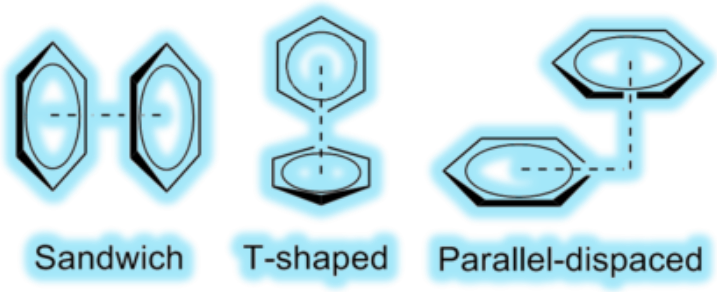

***Figure 1.12**: π-π stacking of benzene molecules.*

Recently, 1D semi-conducting organic materials (nanowire or belt) were fabricated via self-assembly by combining perylenetetracarboxylicdiimide (PTCDI, n-type) and arylene-ethynylenemacrocycle (AEM, p-type). The primary driving force for the self-assembly process is π-π interactions of PTCDI and AEM yielding nanobelts (*Figure 1.13B).* These kinds of materials are useful in many applications in various nanodevices including the electrical and optical sensors.[74]

1.3.4 Solvophobic forces: Hydrophobic effect:

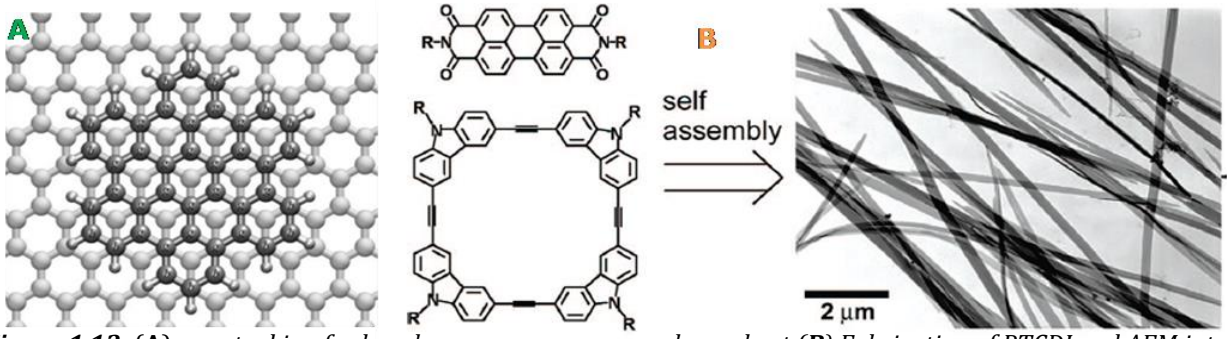

Figure 1.13: (**A**) *π-π stacking for hexabezo -coronene on graphene sheet* (***B***) *Fabrication of PTCDI and AEM into nanobelts through self-assembly. Adopted from ref. 72, 74.*

Hydrophobic effect is necessary element in so many chemical processes in daily life and industry that depends on phase separation between either oil or gas and water.[75] In general; hydrophobic effect is energetically favorable separation between water and oil. This acts as driving force for the self-assembly processes of amphiphiles and micellisation in water.[76] The efficiency of hydrophobicity can be estimated by contact angle (CA)θ,[77] which is the angle between tangent of water droplet and hydrophobic surface as depicted in *Figure 1.14*. Higher the CA (>90°), higher will be the hydrophobicity of respective material. For an example, leaves of lotus have CA ~ 145°, so it is good hydrophobic material to repel the water droplets in the process of self-cleaning. Thermodynamics also plays an important role in the realm of hydrophobicity to decide whether the process is spontaneous or not, according to Gibbs free energy equation can be written ($\Delta G = \Delta H - T\Delta S$). In case of water and oil system, thermodynamic parameters are as follows $\Delta G > 0$, $\Delta H < 0$, $\Delta S < 0$, which indicates that interaction between water and oil is not spontaneous. Aggregation and self-assembly of molecules can also be driven by hydrophobic effect in the process of nanofabrication, for instance, amphiphilic perylene form 3D fibre nanostructures.[78] Rybtchinski and co-workers have made water-soluble perylene by attaching polyethylene glycol chains to the periphery of the perylene molecule, the resulting molecule yields π-stacked fibre morphology driven by hydrophobic effect.[79] Transmission electron microscopic (TEM) image of fibres is presented in *Figure 1.15*. Hydrophobicity have been bringing lot of applications, for instance, self-cleaning, electro wetting and nanofluidics etc.[80]

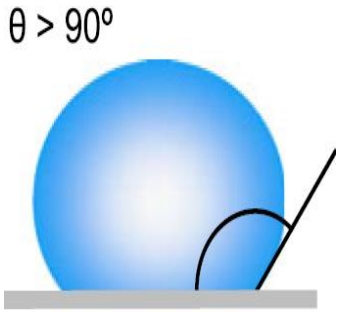

Figure 1.14*: water droplet on a surface with an angle θ in assessing of material hydrophobic character.*

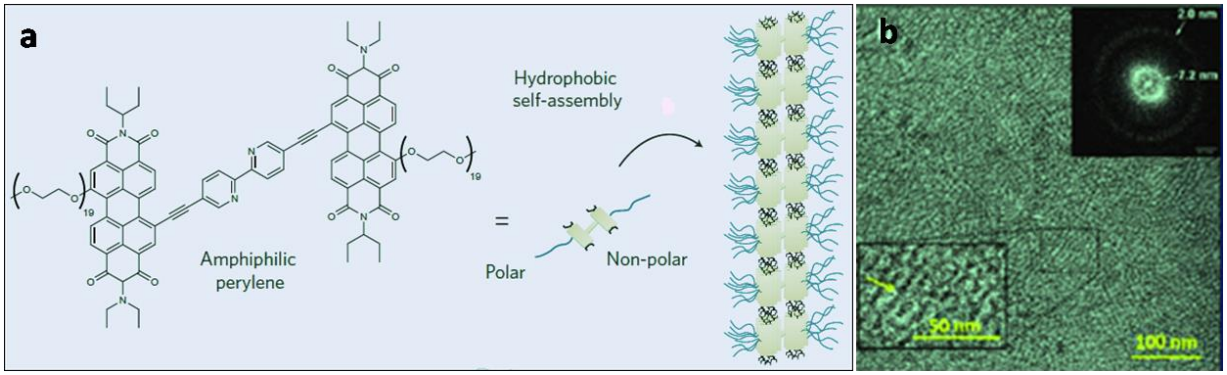

Figure 1.15*: (a) Self-assembly of amphiphilic Perylene into fibres in water owing to hydrophobic interactions, (b) Cryo-TEM image of amphiphilicperylene at higher concentration (3.3 × 10-3 M). Some individual fibers show distinct segments (yellow arrow). Inset: FFT calculation showing spacing of 7.2 nm (fiber-fiber distance) and 2.0 nm (segment-segment distance). Adopted from ref. 78.*

1.4 Nanomaterials:

Nanomaterials are the foundation stones of nanoscience and technology. Nanomaterials normally have at least one dimension in the range or less than 100 nm; which is about 1000 times smaller than the diameter of a human hair. Nanomaterials are classified as of 0D, 1D, 2D and 3D materials based on their dimensionality as depicted in the *Figure 1.16*. Nanomaterials are of interest in the present era by virtue of their unusual electrical, magnetic, optical and mechanical properties.

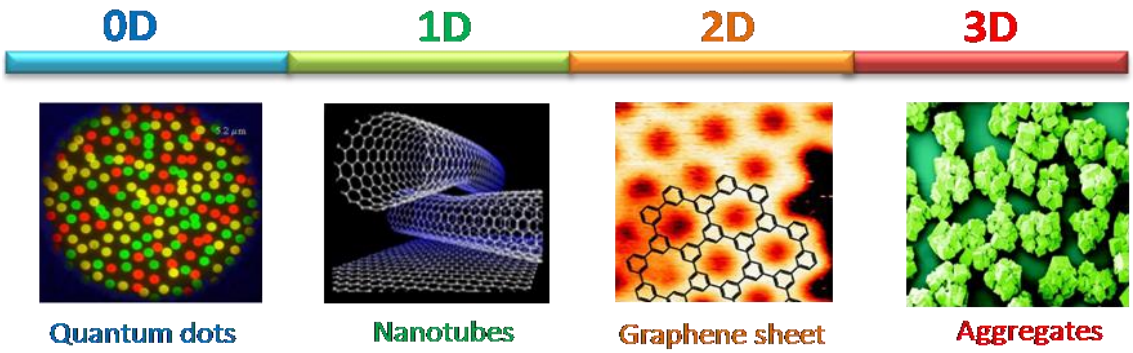

Figure 1.16: *Clasification of 0D, 1D, 2D and 3D materials.*

The first nanomaterial was obtained by vacuum evaporation of iron under inert gas atmosphere and deposited at cooled substrates.[81] Afterwards many new methods were developed to fabricate nanoparticles comprising inorganic ceramics and organic compounds. Although naturally some nanomaterials occurs, synthetic nanomaterials can be found in commercial products like cosmetics, sunscreens, tires, stain-resistant clothing, electronics, sporting goods, as well as many other daily items, and are used in drug delivery, imaging and medicine for the purpose of diagnosis.[82]

Nanocomposites and nanocoatings are employed in many consumer products, such as sports equipment, windows, automobiles and bicycles. One can keep beverages from damage of sunlight by nanocoatinings on glass bottles. Nanostructured titanium dioxide is used in sun-block creams, self-cleaning windows and cosmetics.

1.4.1 Zero- dimensional materials(0-D):

All dimensions of the material should be in the nanoscale, and should show electron confinement with in the 3-D space of 0-D nanomaterials. Generally quantum dots, metal nano particles, fullerenes, and nanoresonators fall in this category. These materials can be amorphous, crystalline, polycrystalline, metallic, ceramic and polymeric etc. They can have any kind of shape such as spherical, triangle, cubic, hexagonal, prism, etc., within the nanoscale. The function of these materials is also dependent of their shapes.

1.4.2 One-dimensional materials (1-D):

In these materials, two dimensions are in the nanoscale. Here the motion of the electronsis confined within the 2-D space. The features of 1-D materials can be crystalline, polycrystalline, amorphous, chemically pure or impure. Nanotubes, nanofibers, nanowires and nanoribbons are general examples for 1-D nanomaterials.

1.4.3 Two-dimensional materials (2-D):

In 2-D nanomaterials, one of the dimensions of given material in the nanoscale and motion of the electrons are confined in 1-D space. Planar type, sheet like and layer kind of materials can be considered as 2-D materials, for instance, single layer graphene. Graphene is an elementary structural element of some carbon allotropes such as graphite, carbon nanotubes and fullerenes.

1.4.4 Three-dimensional materials (3-D):

3-D materials are not nanomaterials because no dimension in the range of nanoscale and all electrons are delocalized in all dimensions of the bulk sample. Thus these materials will be characterized by having three arbitrary dimensions above 100 nm. 3-D materials can have dispersions of nanoparticles, bundles of nanotubes and nanowires as well as multi-nanolayers. Diamond and graphite and most of the naturally occurring objects belong to 3-D materials. These are entirely different from 0-D, 1-D, 2-D nanomaterials.

1.5 Spin-crossover phenomena:

1.5.1 Definition:

Spin-crossover (SCO) is a phenomenon that generally occurs in transition metal complexes where the spin state of metal ion changes from low spin (LS) to high spin (HL) and vice versa because of external stimuli such as temperature, pressure, light irradiation, magnetic field and mechanical perturbation.[83] Spin-crossover can also be called as spin transition (ST) or spin equilibrium. Transition temperature ($T_{1/2}$) is defined as temperature at which two species of HS and LS take part in the transition are equal. SCO effect was first observed by Cambi and co-workers in Fe(III) dithiocarbamate derivatives.[84] Since then, the field of SCO compounds have been increasing drastically till today and appealing the science and technology due to its remarkable applications in memory devices,[85] molecular electronic devices and MRI contrast agents.[86] Particularly, octahedral complexes of certain metal ions of electronic configurations like $d^4(Cr^{+2})$, $d^5(Mn_{+2})$, $d^6(Fe^{+2})$to $d^7(Co^{+2}, Ni^{+3})$[87] in the first transition series may display spin transition under external stimuli. During the spin transition, the metal to ligand bond distance remarkably changes due to transfer of electrons in the anti-bonding eg* orbitals. Suppose, in Fe(II) system, the change in Fe-N bond distance was found to be ~ 0.2 Å during spin transition. In LS Fe(II) complex, e_g* orbitals were empty and in HS complex, anti-bonding orbitals are filled two unpaired electrons which leads to show transition between singlet ($^1A_1$) and quintet ($^5T_2$) states of Fe(II) system followed by increasing the Fe-N bond distance remarkably as compared with Fe-N bond distance in LS complex. Few examples of SCO compounds are presented in the *Figure 1.18.*

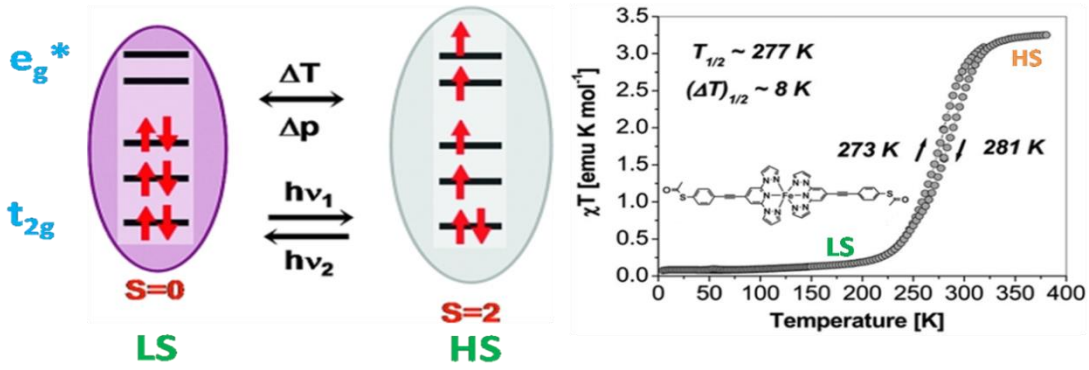

Figure 1.17*: Schematic representation of distribution of electrons in LS and HS under external stimuli and spin crossover curve with $T_{1/2}$ = 277 K. Adopted from ref. 89.*

The measurement of magnetic moment is frequently used to characterize SCO since there is much difference in the magnetic moments of HS (ca. 5 B.M.) and LS (ca. 0 B.M.) of Fe(II) system while monitoring the temperature.[88] In the *Figure 1.17*, temperature dependent magnetic measurement of $[Fe^{II}(L)_2]$-$(ClO_4)_2$ [L = S-(4-{[2,6-(Dipyrazol-1-yl)pyrid-4-yl] ethynyl}-phenyl) is given in the range of 4.5-380 K. The measurement was performed at both heating (↑) and cooling

(↓) cycles to detect the reversible SCO behavior with a hysteresis loop. While heating till 380 K, χT was found to be 3.25 emu K mol^{-1} which has good agreement with the expected value of HS Fe(II) ion at S = 2 state. Conversely, upon cooling down to 4.5 K, magnetization had gone down and

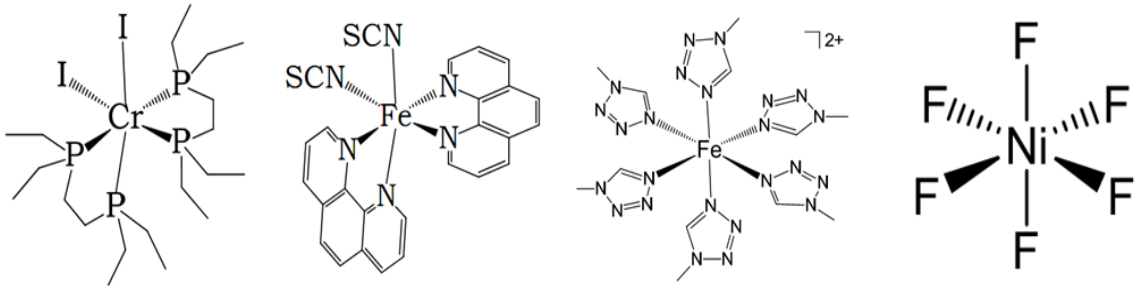

***Figure 1.18**: Some examples for octahedral SCO complexes. Adopted from Chem. Commun. 1989, 1322.*

reached the value χT = 0.07 emu K mol^{-1} which is approximately equal to zero of LS Fe(II) ion in the S = 0. Here ST temperature $T_{1/2}$ is ~277 K which is mid-point where equal amounts of LS and HS of Fe(II) will exists.[89] SCO phenomena also depends on ligand field strength, donor or acceptersubstituentsontheligand,[90] type of ring whether six membered or five membered,[91] and counter anions.[92] Characterization of ST material scan be done by using few techniques such as crystallography, magnetometry, Mossbauer spectroscopy, FTIR, Raman spectroscopy, and UV-Visible spectroscopy.[93-96]

1.5.2 Spin crossover nanoparticles (SC NPs):

Nanoparticles play a great role in the search for miniaturized (or size reduction) next generation devices, due to the availability of several methods for the syntheses and manipulation of NPs. Magnetic NPs (eg. Fe_3O_4) are of particular interest due to the evident information storage applications in high density media devices. In addition, functionalized magnetic NPs can offer a wide variety of applications, specifically for biological and medical usage,[97] Drug delivery,[98] or tumor treatment,[99] protein detection[100] are some other applications where magnetic NPs can make a change. Recently, coordination complexes based magnetic materials had been self-assembled from solution into nanoparticles,[101] by avoiding the

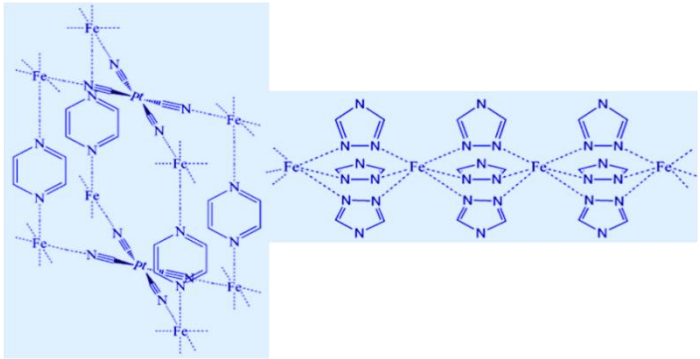

***Figure 1.19**: Molecular structure of polymeric spin crossover complexes: 3D [Fe(pyrazine)Pt(CN)$_4$]$_\infty$ (right) and 1D [Fe(trz)$_3$]$_\infty$(left). Adopted from ref. 109.*

use of expensive high-energy top-down physical methods. For example, micro emulsions or reverse micelles techniques had been used very successfully for the synthesis of molecule based NPs with superparamagnetic[102, 103] and photomagnetic[104,105] properties. The display of a magnetic "memory effect" is imperative in the exploration of magnetic NPs which can be integrated in actual devices but regrettably, biastability occurs at very low temperatures in most magnetic transition metal coordination compounds. The SCO complexes are one remarkable inorganic switches displaying bi-stability at the molecular level.[106, 107] Here the SCO between the low-spin (LS) configuration of the ground state and a meta stable high-spin (HS) state can be triggered by external stimuli (light, temperature, electric field, x-ray, pressure, and surface plasmon).[108] Many successful efforts to synthesis SCO NPs had been reported in the past decade. In all reports, the target compounds were polymeric iron (II) coordination compounds since these materials generally display broad hysteresis close to room temperature. NPs of the [Fe- (pyrazine)$Pt(CN)_4$] 3D network[109] (*Figure 1.19*) were prepared by through reversed micelles and size control was achieved by tuning the concentration of metal ions.[110] In this case, the remnant HS fraction of metal centers increases and the magnetic hysteresis decreases with the size of the NPs. The hysteresis completely disappears for 7 nm diameter NPs. Analogous results were found in parallel studies carried by Real et al. in NPs of the same material but followed a different solid state treatment.[111] When [Fe (pyrazine)$Pt(CN)_4$] NPs are stabilized into a biopolymeric matrix, magnetic hysteresis is retained below 4 nm size as demonstrated by Bousseksou et al.,[112] despite only about 1/3 of the iron(II) centers involved in the process. The decrease and further disappearance of the thermal hysteresis and bistability were due to the decrease in cooperatively when the iron atoms inside the NPs started to be severely reduced compared with those on the surface.

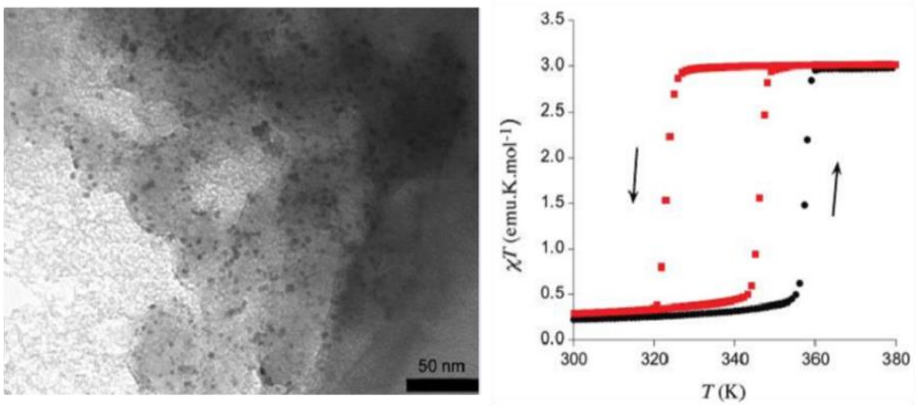

***Figure 1.20**: TEM image and temperature dependence of the magnetic moment (black circles, 1st heating protocol; red squares, stable hysteresis cycle) of [Fe (Htrz $_{2.95}(NH_2trz)_{0.05}](ClO_4)_2$. Adopted from ref. 109.*

Bistable NPs were prepared from SC complexes of iron(II) and trizole down to a few nanometers in size, which

were around 6 nm and maintaining an over 40 K thermal hysteresis. Size and magnetic properties of NPs can be examined by altering chemical components of these nano objects. In order to prepare bistable NPs closer to room temperature, 1,2,4-triazole was mixed with 4-amino-4H-1, 2, 4-trizole that were already successful for this purpose in bulk.[113] The discovery of bistable magnetic NPs of 6 nm with a wide thermal hysteresis above room temperature prove the actual possibilities of SC materials for nanotechnological applications.

1.5.3 Spin crossover curves:

From the measurement of the temperature dependent magnetic property of a SCO molecular system, the relative concentrations of LS and HS states as a function of temperature can be determined from the plot of the HS molar fraction γHS versus T. For SCO complexes in solution

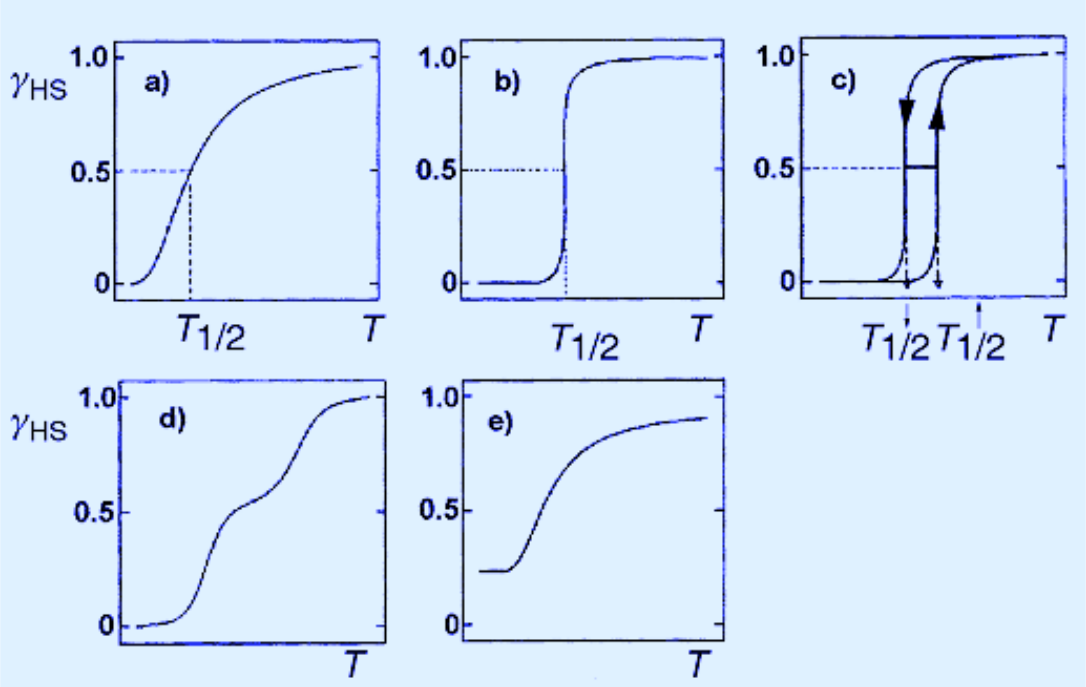

***Figure 1.21**: The nature of ST curves for SC systems in the solid state: (a) gradual; (b) abrupt; (c) with hysteresis; (d) with steps; (e) incomplete. Adopted from ref. 114.*

state, the magnetic behavior follows a curve similar to that of *Figure 1.21a* and can be explained in terms of a simple thermal equilibrium involving a Boltzmann distribution over all vibronic levels of the two spin states. Here, the transition arises at the molecular level without the involvement of lattice or neighboring interactions. For solid systems, lattice effects are important and the behavior is described by the curves shown in *Figure 1.21a–e.* The transition may be gradual and continuous over along temperature range, similar to solution behavior (*Figure 1.21a*). The transition may be

related with a thermal hysteresis loop (*Figure 1.21c*) or be a two-step process for bimetallic or polymeric system (*Figure 1.21d*). In certain instances, the transition may be incomplete at one or both extremes of the SCO curve (*Figure 1.21e*). The curves are indicative of the nature of the SCO and the abruptness of the change suggests the extent of cooperativity involved in the dissemination of the spin change in the solid lattice. That means that the extent to which the electronic and structural changes in a molecule undergoing a SCO influence related changes in neighboring molecules. When the cooperativity is low the transition will be a gradual or continuous process, but when its urges the transition becomes more abrupt and can occur within a very narrow range of temperature or be linked with a phase change and/or thermal hysteresis.[114a] A transition temperature is defined as that temperature at which equal portions of HS and LS species exists (HS 50% and LS 50%). For transitions displaying hysteresis two transition temperatures $T_{1/2}\downarrow$ and $T_{1/2}\uparrow$ determine the width of the hysteresis loop.

1.5.4 Spin crossover coordination polymers and their nano-fabrication:

Coordination polymers have vast variety of physical and chemical properties as well as wide spread applications in science and technology. Kurth *et al.* have made soluble coordination polymers and traditional polymers with covalently formed polymers,[114b] where the monomers are connected by covalent bonds. Ruben group have synthesized of a ditopic building block ligand, 1,4-bis(1,2':6',1''-bispyrazolylpyridine-4'-yl)benzene L,[114c] which was converted into a linear 1-D iron(II) coordination polymer represented as $\{[Fe^{II}(L)]_n(BF_4)_{2n}\}$ with a above room temperature

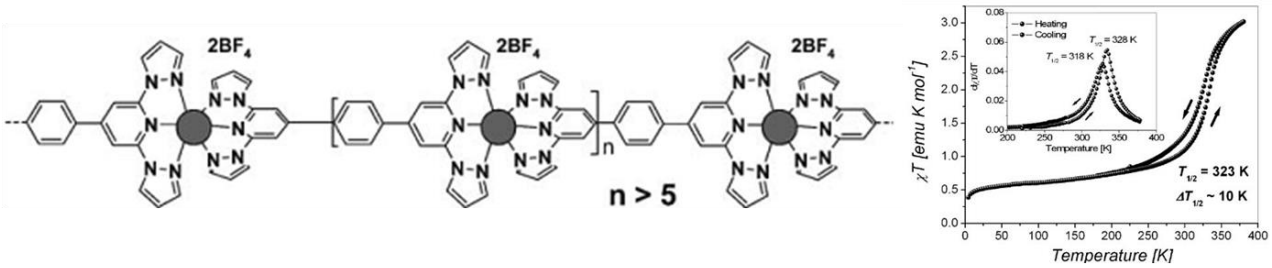

***Figure 1.22**: Above room temperature SCO coordination polymer $\{[Fe^{II}(L)]_n(BF_4)_{2n}\}$ and its χT vs T plot from 4.5 to 380 K.*

$T_{1/2}$ value of 323 K together with a hysteresis loop value of $\Delta T_{1/2}$ ~10 K. Unfortunately due to the poor solubility of this SCO polymer and processing difficulty the material aspect of this polymer was not explored. For the first time Chandrasekar *et al* have reported the fabrication of high resolution nano-lattices composed of solution processable and solution stable SCO Fe(II) metallo-supramolecular polymer. The SCO polymer was prepared form a back-to-back coupled ditopic unit comprises of pyridine, pyrazole and triazole forming a chelating hybridligand.[114d]

An extensive variety of solid-state architectures including one-dimensional molecular chains and ladders motifs, two-dimensional grids, brick wall structures, and three-dimensional frame-works had already been prepared with a simple rigid rod like spacer ligand such as 4, 4'-bipyridine.[115] These Fe(II) coordination polymers are important because of their promising catalytic,[116] electrical,[117] optical,[118] and magnetic[119] properties. Variable-temperature magnetic susceptibility measurements have been revealed the occurrence of the HS ↔ LS transition with a spin transition temperature $T_{1/2}$ of 205 K. The crystal structure was resolved at 293 K (high-spin form) and at 173 K (low-spin form). The complex exhibits one-dimensional zigzag chain structure

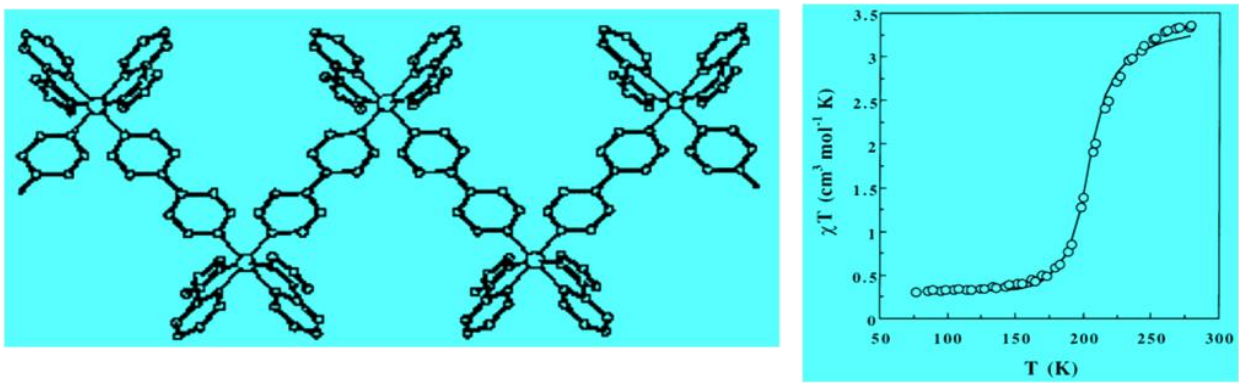

Figure 1.23: (a) *One-dimensional zigzag chain structure of* $[Fe(pyim)_2(bpy)](ClO_4)_2$. $2C_2H_5OH$ *at 293 K. (b) Temperature dependent magnetic behaviour for* $[Fe(pyim)_2(bpy)](ClO_4)_2 \cdot 2C_2H_5OH$. *The solid line represents fitted curve. Adopted from ref. 115.*

in which the iron (II) active sites were connected to each other by a chemical bridge as the rigid rod like 4, 4'-bipyridine molecule. The Fe-Fe separation via the bpy ligand equals 11.523(2) and 11.201(2) Å in the HS and LS structures, respectively. The polymeric chains have extended along the with the HS-LS energy gap and result in a relatively gradual SCO of the complex. Fabrication of SCO polymers based micro scale patterns can also be achieved using three dimensional SCO coordination polymer,[120] Fe(pyrazine)$[Pt(CN)_4]$ by using a combination of top-down and bottom-up methods is shown in (*Figure 1.24*). More importance is given to 3D polymers, because they show; 1) room-temperature hysteresis, 2) multi-layer assemblies, and 3) top-down processability. In fact, top-down technique becomes possible because of the extreme insolubility of the coordination network when compared to that of the molecular spin-crossover complexes. Square patterns of complex Fe(pyrazine)$[Pt(CN)_4]$ were made on a gold-coated silicon surface covered by a conventional polymethylmethacrylate (PMMA) by using election beam lithography (EBL). Square-

shaped patterns of various size and density were written by a tight focused electron beam. Clear patterns of various sizes were created from scanning electron microscopy (SEM) as depicted in the *Figure 1.24.* These patterns have shown square shapes with sharp borders for feature sizes between 2 μm and 200 nm. Patterns of smaller periods turned out to be unsuitable for lift-off. This limit can be improved up to some extent by decreasing the number of deposition cycles.[121, 122]

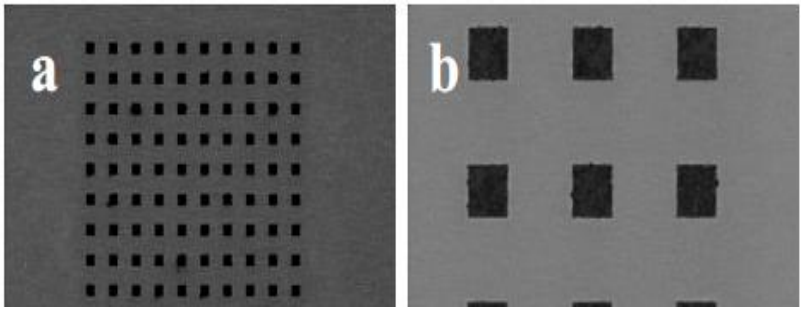

Figure 1.24*: SEM images of patterns of Fe(pyrazine)[Pt(CN)$_4$] after 15 deposition cycles with pattern size of 2 μm. Adopted from ref. 120.*

1.5.5 Light induced excited spin state trapping (LIESST) effect:

Spin-crossover effect also can be studied by light irradiation, called the LIESST effect, which was detected accidentally in a spin-crossover compound [Fe(ptz)$_6$](BF$_4$)$_2$, where LS state was converted into meta stable HS state under laser light of certain wavelength at sufficiently lowtemperature.[123] Mechanism involved in photo switching process was sketched clearly in *Figure 1.25*. Green colour Ar$^+$ laser of wavelength 514 nm was used to induce spin-allowed transition from $^1A_1 \rightarrow {}^1T_1$. Therefore, fast relaxation was observed over two successive intersystem crossing steps, $^1T_1 \rightarrow {}^3T_1 \rightarrow {}^5T_2$, populates electronic state $^5T_2$ and results HS Fe (II) complex. Transition from $^5T_2 \rightarrow {}^1A_1$ is spin forbidden but decays the thermal energy to the ground state $^1A_1$ at low temperature. Reverse LIESST effect can also be studied by the application of red light of wavelength 820 nm upon HS complex. During the irradiation of HS state with red light, electron will be excited $^5T_2 \rightarrow {}^5E$ and there by two intersystem crossing steps from $^5E \rightarrow {}^3T_1 \rightarrow {}^1A_1$ leading to

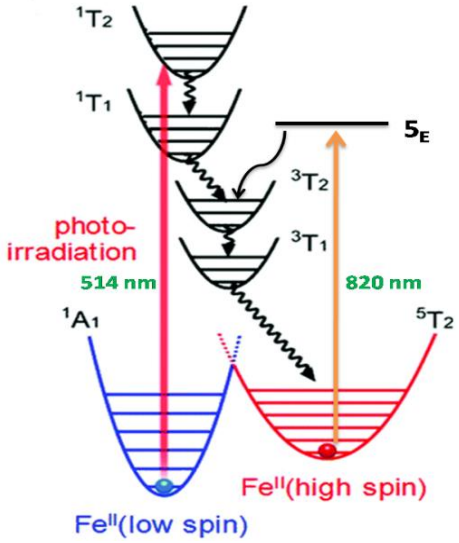

Figure 1.25 *Mechanism for LIESST Effect. Adopted from Dalton Trans. 2014, 43, 4220–4232.*

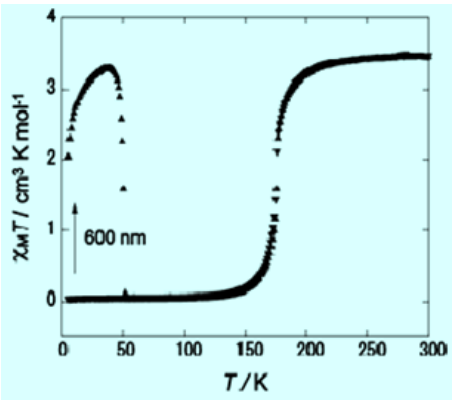

Figure 1.26*: LIESST effect of a SCO Fe(II)compound.*

get back LS state. Therefore both LS and HS states can be switched upon the application of light irradiation of certain wavelength.[124] It should be noted that, not only visible light, even X-rays have also been found in SCO of $[Fe(phen)_2(NCS)_2]$ and $[Fe(phen)_2(NCSe)_2]$ (phen = 1,10-phenanthroline) at 45 K.[125] The influence of light on SCO systems is being pursued actively and many new phenomena have been reported related to LIESST effect.[126a] LIESST effect also understood clearly from the metal complex $[Fe^{II}(HL)_2](ClO_4)_2$ (**1**) under the irradiation of wavelength 514 nm. Here L is [2-(((2-phenylimidazol-4-yl)methylidene)-amino)ethyl]-N-methylamine). Iron(II) metal ion has reached meta stable HS state (230 K) from LS state (130 K)during the application of electromagnetic radiation of wavelength 600 nm and then dropped into HS state in absence of light.[126b]

1.5.6 Entropy Changes upon Spin-Crossover:

In addition to physical methods for the study of spin SCO phenomena, calorimetric measurements are also well established. They have shown the spin transition and enabled to determine transition enthalpy and entropy for the example like iron(II) SCO compounds, are $\Delta H = H_{HS} - H_{LS} \approx 6\text{-}15$ k J mol^{-1} and $\Delta S = S_{HS} - S_{LS} \approx -40$ to 65 J K^{-1} mol^{-1} at spin transition temperatures around 130 K. 28 From C_p measurements of $[Fe(phen)_2(NCS)_2]$ and $[Fe(phen)_2(NCSe)_2]$,[127] Sorai and Seki 37 concluded[128] that the driving force behind the spin transition is the considerable entropy increase on going from the LS to the HS state. This is right for all spin crossover complexes irrespective of the central metal ion. According to Sorai and Seki, the electronic contribution to the total acquired gain in entropy of $\Delta S \approx 50$ J $K^{-1}mol^{-1}$ is about 30%: $\Delta S_{mag} = R(\ln(2S+1)_{HS} - \ln(2S+1)_{LS}) = 13.4$ JK^{-1} mol^{-1}. For complexes with symmetry lower than *Oh*, the orbital contribution is not remarkable. The major part of the remaining 70% of the entropy change will be taken from intra molecular stretching modes and intra molecular deformation modes; only a comparatively small fraction is supposed to be attributable to changes in intermolecular vibrational modes. The authors concluded from the dominant share of the total entropy gain from the vibrational changes that long-range interactions from coupling between the electronic states and the phonon system must plays a vital role in the cooperative spin transition in the solid. The SCO might be thermally induced when the energy of the LS state in its equilibrium geometry is lower than the energy of the HS state, also in its equilibrium energy.[129, 130] Above a particular temperature, the thermodynamically stable state may be the HS state. This is due to the fact that the entropy of the system in the HS state is much larger than that in the LS state ($\mathbf{\Delta}S = 0$) and the gain in $T\mathbf{\Delta}S$, T being the temperature, compensates the energy loss. It has been investigated that entropy is remarkable physical property that can measure weather complex is LS or HS.

1.5.7 Fabrication of Spin-Crossover(SCO) materials:

The demand for efficient information storage is one of the great challenges for scientific and technological research.[131] The hard disks of computer store data due to the magnetic anisotropy orientation of all small regions of a spinning disk. During the last decades, scientists and engineers have enhanced the capacities of memory devices by reducing the size of the effective magnetic storage regions.[132] This trend is likely to continue until to reach the so-called super paramagnetic limit.[133] Conversely the surrounding heat can trigger de-orientation of magnetic domains as a result of their decreased size. Nanopatterning of the storage domains seems to be promising to overcome this difficulty.[134] In this regard, nanofabrication of SCO complexes of first transition series metal ions ($3d^4$ to $3d^7$) have been proven to be good candidates for applications in information technology, sensors, and molecular memory and displays.[135-139] Since information generated in a SCO event are within the nanometric regime, the interfacing of SCO units with micro or nanoscale device environment is of great importance. Fabrication of SCO materials can be achieved by using some bottom-up techniques like layer-by-layer assembly, [140] electron beam lithography and spin coating.[141]

For example, lithographic controlled wetting (LCW) was employed to fabricate SCO complex $[Fe^{II}(L)_2](BF_4)_2$ (**I**) where L = 4,4″-dioctylated 2′,6′-bispyrazolylpyrine with $T_{1/2}$ is ~ 270 K. Lithography is a method of printing originally based on the immiscibility of oil and water.[142, 143] For the nanofabrication of **I** on TEM grid is as fallows, polystyrene (PS) thin film was made by drop casting 100 µL of PS (125 mg) solution in toluene (2 mL) on TEM grid and allowed it dry.

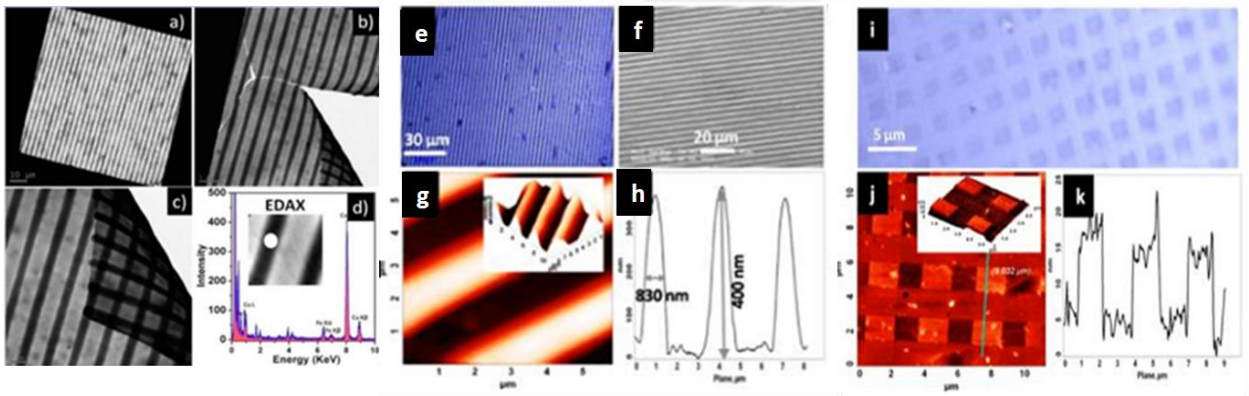

Figure 1.27*: (a, e, i) Optical images of wedge stripes, rectangular stripes, and square pillars, respectively. (b, f) SEM images of wedge and rectangular stripes. (c, g, j) AFM 3D images of wedge stripes, rectangular stripes, and square pillars, respectively. (d, h, k) AFM topographic profile (height and width) of the patterns shown in c, g, j, respectively. Adopted from ref. 144.*

Subsequently, microstripes of **I** were prepared on PS thin film through LCW technique. TEM images

of 1D pattern of Polymer embedded **I** were mentioned in *Figure 1.27*(*a, b,c*). Moreover, energy dispersive X-ray analysis (EDAX) clearly confirmed the presence of Fe in the dark SCO patterns, by elevating Fe signals (*Figure 1.27d*).

Additionally, micropatterning of **I** also has been done on silica glass slide by drop casting 20 µL of acetonitrile solution of **I**. Confocal microscope and scanning electron microscope images are depicted in figure and SCO stripe was extended to several hundred micrometers with height within the sub micrometer domain. The AFM profile measurements of the wedge stripes revealed that the height, fwhm (full width at half maxima), and period/channel parameters were 400 nm, 830 nm, and 3 µm, respectively (*Figure 1.27c, d*), here triangular edge angle of a stripe was found to be about 70°. Furthermore, fabrication of 0D micro square pillars were also made and conformed by AFM studies. Confocal microscope and AFM measurements have showed the presence of 0D micro square pillars on a 2D glass surface (*Figure 1.27i, j, k*). AFM measurements revealed that the formation of nearly perfect squares with the height (H) and width (W) profiles of 25 nm ×1.5 µm, respectively (*Figure 1.27j, k*). Here, the height of each square is 27 times smaller than the height of the 1D array and the top surface area of each square is just 2.25 μm^2. This kind of 0D square pillars may be useful as logical structures as well as photonic applications if the synergy between the two is established.[144]

1.6 Gold nanoparticles (Au NPs):

1.6.1 Introduction:

Chemistry of gold in bulk was not established well due to its inertness and less reactivity. When it comes to nanolevel, great chemistry had been penetrated in to science due to its display of fascinating applications in various fields such as chemistry, physics, and material science, biology etc.[145] Au NPs are most stable metal NPs and also termed as gold colloids. In the year of 1718, Hans Heinrich Helcher had published a complete book on gold colloids[146] in which, he stated the advantage of boiled starch in its drinkable gold synthesis enhanced its stability. Drinkable gold contains gold in the elementary form whereas under extreme sub-division will be suspended in a liquid. In 1818, an explanation was given by Richters to understand the differences in colour exhibited by various syntheses of drinkable gold.[147] Purple colour solutions were seen because of finest degree of subdivision of gold

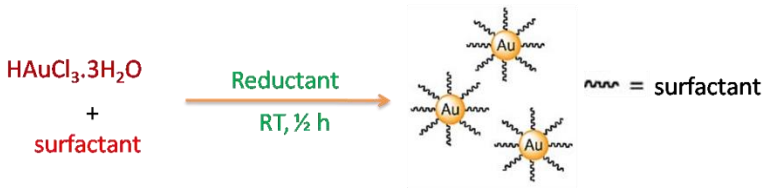

***Figure 1.28**: Syntheses of Au NPs stabilized by surfactant in presence of $NaBH_4$. Adopted from ref 155.*

whereas yellow colour solution were found due to particle aggregation. Deep red colloidal Au NPs were prepared by the reduction auric acid ($AuCl_4$) using phosphorus in carbon disulfide reported first time by Faraday in 1857. Many synthetic methods have been investigated for the preparation of colloidal gold in the 20th century.[148-154] In general, Au NPs can be prepared via the reduction of $HAuCl_3.3H_2O$ by using reductants like sodiumborohydride,[155] sodiumascorbate,[156] trisodiumcitrate[157] in presence of surfactants at room temperature. Surfactant and reductant plays vital role in monitoring shape and size metal NPs. Surfactant is combination of hydrophilic (head) and hydrophobic (tail) groups. Normally hydrophobic group will be alkyl chain which creates steric hindrance in given system to prevent aggregation of NPs.

$$AuCl_4^-(aq) + N(C_8H_5)_4^+(C_6H_5Me) \longrightarrow N(C_8H_{17})_4 + AuCl_4^-(C_6H_5me)$$

$$\begin{matrix} m AuCl_4\text{-}(C_6H_5Me) \\ + \\ nC_{12}SH(C_6H_5Me) + 3me\text{-} \end{matrix} \longrightarrow Aum(C_{12}H_{25}SH)n(C_6H_5me) + 4m\ Cl^-(aq)$$

Scheme 1.1*: Two phase synthesis of 1-dodacanethiol stabilized gold nano-particles, me = methyl group.*

Stabilization of NPs by organic surfactants are no longer enough to stop aggregation, therefore NPs needs to have to suitable dispersive reagents for long time stability. Depending on Pearson's concept of hard and soft acid and bases (HSBC),[158] hard acids will tend coordinate with hard bases and soft acids will try to bind with soft bases. In his theory metals and metal ions were considered as acids and electron rich ligands were bases. Au and Au^+ are behaves as soft acids

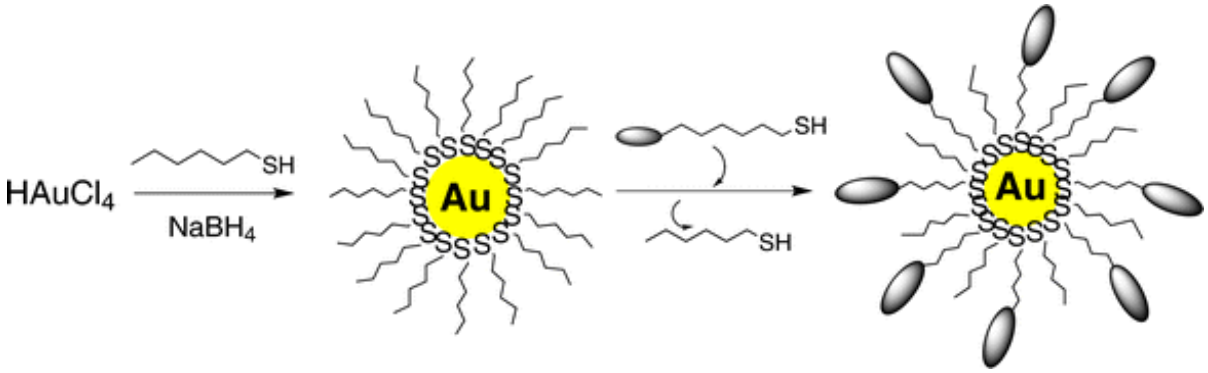

Figure 1.29*: Reduction of $HAuCl_4$ to prepare Au NPs stabilized by alkyl thiols. Adopted fro ref. 160.*

whereas –SH (thiol) ligand acts as soft base, consequently, gold will have tendency to coordinate with sulphur atom. Therefore organic thiols will be suitable dispersive agents in stabilizing NPs.[159] In 1994, Brust and his coworkers also reported on the use of organic thiol molecules as best dispersing agents. Size of the nanoparticle can also be increased by varying the length of the alkyl

chain of thiol ligand, suppose, from 1-dodecanethiol to 1-hexanethiol, size of particle will be increased due to less steric hindrance for aggregation of NPs. Indeed, thiol stabilized NPs can be repeatedly separated and redissolved in organic solvents without decomposition and aggregation. Therefore, thiol stabilized NPs are easy to handle just like stable organic compounds, which is another advantage over surfactant stabilized NPs. *Figure 1.29* represents stabilization Au NPs via construction of thiol monolayers followed by exchange of another thiol ligand to yield mixed-monolayer stabilized Au NPs.[160] Moreover, two phase reaction path way in attaining thiol stabilized gold NPs was reported by Brust and his coworkers mentioned below reaction scheme.[161] Here, 1-Dodecanethiol had chosen to stabilize Au NPs in presence of phase-transfer reagent tetraoctylammonium bromide (TOAB) in toluene solvent. In first phase $HAuCl_4$ was transformed in to toluene in presence of TOAB and in second phase Au (III) was reduced to Au (0) by $NaBH_4$ in presence of dodecanethiol. Immediate colour change from orange to deep brown during the addition of $NaBH_4$ has been observed the formation of thiol bound Au NPs. Chemistry of Au NPs have attracted various fields of science and technology because of tremendous applications in paints, catalysis, optical properties, conductivity, magnetic properties, microwiring, medical treatment etc.[162] One of the important physical properties of gold NPs is they exhibit surface plasmon resonance (SPR), which is very useful for single molecule sensing applications.

1.6.2 Surface Plasmon resonance (SPR):

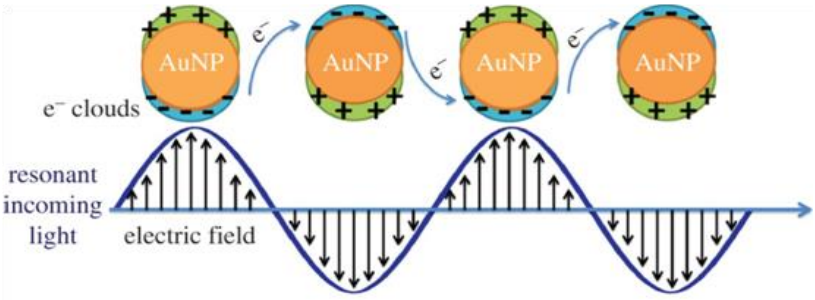

***Figure 1.30**: Establishment of resonance condition between AuNPs and electromagnetic radiation to show SPR. Adopted from DOI: 10.1098/rsfs. 2013. 0006, Published 23 April 2013.*

Surface area of the NPs will be greater than in bulk leads to have more number of atoms on the surface. Hence, plenty of valence electrons will occupy surface of metal NPs and positive electric charge of metal is fixed and all electrons will move around NPs. Since electrons will also exhibit particle nature, they tend to vibrate and produce oscillating electric field within the system. When light shine on metal surface of NPs at critical angle θ, the frequency of the electromagnetic radiation will match with frequency of oscillating electrons of metal surface. Consequently, resonance condition will be established and light would be absorbed by NPs to generate collective oscillation of electrons. This phenomenon is called as surface Plasmon resonance (SPR) and this was reported first by Kretschmann and Raether in 1968.[163] The flow of

collective oscillating electric field is also named as plasmonic waves. If SPR is confined to a particular surface of NPs, then it is said to be localized surface plasmon resonance (LSPR). When 20 nm Au NPs were irradiated by 520 nm of visible region of electromagnetic radiation, electric field

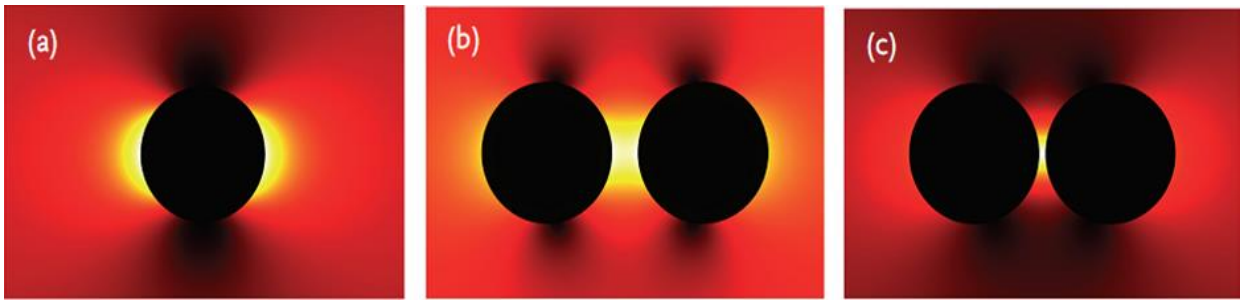

Figure 1.31*: (a) LSPR at both sides of Au sphere (b) (c) HOT SPOTS generation at junctions of Au nanospheres. Adopted from 2013 Wiley-VCH Verlag GmbH & Co. KGaA.*

generated by LSPR has been distributed on left side and right side of the Au NP, perpendicular to the direction of the incident light in *Figure 1.30*. Strength at junctions of Au spheres. This kind of junctions generally called as HOT SPOTS and the density of electric field at junctions increases as decreases the distance between NPs. In the *Figure 1.31(b)* distance between two Au spheres was 4 nm and in the *Figure 1.31 (c)* the distance was found to be 1 nm. Therefore density of generated electric field in case *Figure 1.31(c)* is much greater than in the *Figure 1.31(b)*. Generation electric field strength due to SPR has an advantage of detecting so many organic molecules at low concentration by enhancing Raman spectra intensity called as surface enhance Raman spectrum (SERS). Suppose, single molecules of Rhodamine 6G (R6G) at the junction of minimum two of Ag NPs due to hot spot generation at junctions of Ag NPs (*Figure 1.32*).[164] It is known that SERS materials have several application in nanoscience, biology, chemistry and physics. Generally, spherical Au NPs use to absorb green light (520 nm to 550 nm) and emits purple colour light, purple colour is complementary colour to green. Similarly, a colloidal Ag NPs show SPR band at 400 nm (blue) and emits yellow colour, therefore, yellow is complementary to blue. Absorption wavelength will be decided by size and shape of the NPs.

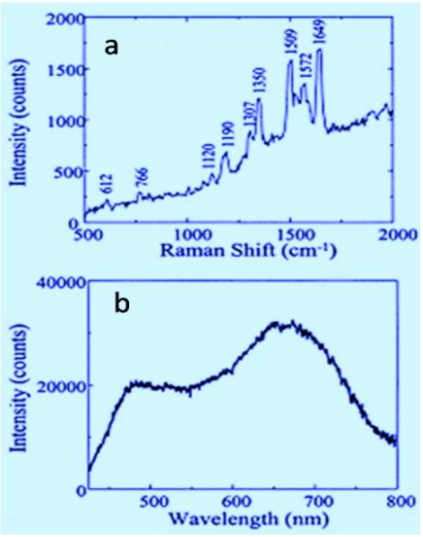

Figure 1.32*: (a) SERS of single molecule R6G at the junction of Ag NPs, (b) Resonant Rayleigh scattering spectrum of a single SERS-active Ag particle incubated with 10 mM NaCl and 2 nM R6G. Adopted from ref. 164.*

1.6.3 SERS from hot spots:

SERS can be seen for the complex of ferrocene and cucurbiturils at hot spot junctions. Cucurbiturils are macrocyclic molecules made of glycoluril ($C_4H_2N_4O_2$) monomers linked by methylene bridges (-CH_2-). The oxygen atoms are located along the edges of the band and are tilted inwards, forming a partly enclosed cavity. The name is taken from the resemblance of this molecule with a pumpkin of the family of Cucurbitaceae. Suppose complex of ferrocene (Fc) and Cucurbit [7]urils is labeled as Fc@CB(7), here ferrocene used as the inert molecule which can be captured tightly within CB(7).[165] Ferrocene molecule will fit easily in to the cavity of CB(7). In order to achieve SERS for FC@CB(7), this complex was assembled with Au NPs to make multilayer film on a ITO substrate by layer-by-layer approach. A convenient and cost-effective chemical method was developed to fabricate Au aggregates with uniform 1 nm nanogaps via the assembly of cucurbit [7]urils with Au colloids. Cucurbit[7]urils located in the nano gap region can be used as a useful SERS hot-spot nanocontainer to show the SERS enhancement of Fc up to 109, SERS of Fc@CB(7) was presented in figure. *Figure 1.33A* revealed that TEM images of CB(7)-bridged Au NPs and *Figure 1.33B* are SEM images of Fc@CB(7)-bridged Au NPs aggregates. The result that the SERS enhancement factor (EF) of Fc is larger than EF of CB[7] is intriguing, SERS enhancement may originate from EM and chemical contributions. The EM effects have come from exciting the localized surface Plasmon resonance (LSPR) of the substrate. The reason behind the obtained result might be that the Fc molecules were placed at the centre of hot-spot, while the bond corresponding to 800 cm-1mode is a little deviated from the centre due to the bigger size of the CB[7] molecules. CB[7] served as good SERS container and made a platform for studies of the EM enhancement mechanism excluding chemical enhancement arising from direct or indirect binding of molecules to metal surfaces.[166]

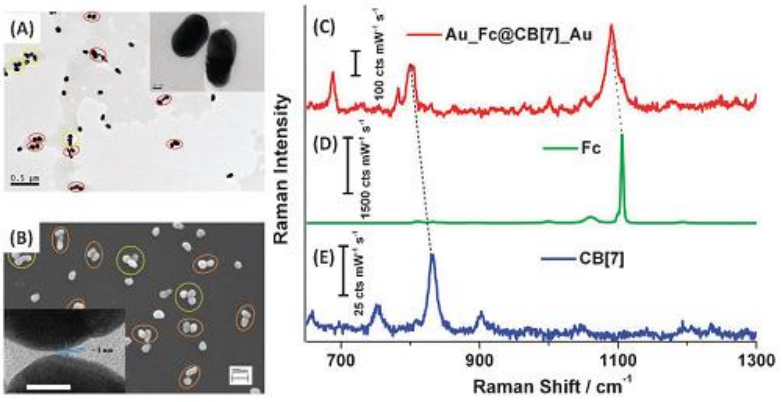

***Figure 1.33**: (A) TEM image of CB[7]-bridged Au nanoparticle aggregates; (B) SEM image of Fc@CB[7]-bridged Au nanoparticle aggregates deposited on the glass. Inset in panel (A) is the high-resolution TEM image of the formed dimer. Inset in panel (B) is the high-resolution TEM image of the formed nanogap. The scale bar in the inset corresponds to 10 nm. Red circle: dimers, yellow circle: trimers. (C) SERS spectrum recorded from Fc@CB-bridged Au aggregates on glass; Raman spectra from (D) bulk Fc and (E) bulk CB[7]. Adopted from ref. 165.*

1.6.4 Optical properties of metal nanoparticles (M NPs):

Au MNPs tend to exhibit multiple colours in the visible region over pretty gold due to rising of the surface plasmons in the nanolevel. SPR is sensitive with shape and size NP and this leads to show different absorption wavelengths. Shift of the Plasmon resonance is also depends on the dielectric constant of solvent, surrounding material and capping material. As the size and shape of the particles changes, the surface geometry changes resulting a remarkable shift in the density of electric field on the metal surface. As a result of this, there will be change in the oscillation frequency of the electrons and creating different cross-sections for absorption and scattering.[167] In order to monitor optical properties, shapes and size of noble metal nanoparticles needs to be changed.[168-172]

In case of Au NPs, Au spheres will show characteristic purple color and absorption wavelength around 520-550 nm. As shape changes from spherical to nanorod, great shift in the absorption wavelength will be noticed as shown in the *Figure 1.34*. Two kinds of absorption bands were evolved for Au nanorods, one is at 520 nm and another on at higher wavelength (near IR region) as depicted in figure.[173] First Plasmon resonance at 520 nm is due to transverse oscillation of electrons and other one at near IR region is because of longitudinal Plasmon resonance at longer wavelength obtained from high aspect ratio. The transverse surface Plasmon resonance is independent aspect ratio whereas the longitudinal surface Plasmon resonance increases as increases the aspect ratio.

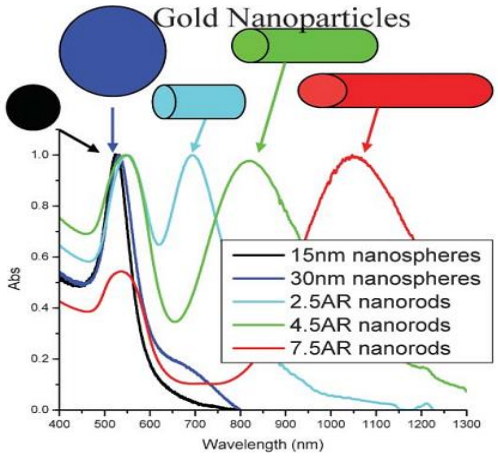

***Figure 1.34**: SPR wavelengths of Au Nps of various size and shapes. Adopted from ref. 173.*

1.7 Organic optical waveguides:

The study of optical waveguides comes under the discipline of nanophotonics which is aimed to improve technology to control and manipulate optical energy in the nanometer scale.[174] The development of technologies regarding nanophotonics rely on new optical methods, constructing photonic devices having low cost, size reduction and better performance.[175] Optical wave guides were one of the necessary tools of miniaturized devises of nanophotonics,[176] these are physical structures have been used to guide the light in a desired direction such a way that they acts as 'light pipe'. Prof. K. Kao was received Noble prize in physics in 2009 for his break through result on the light transmission in fibers for optical communication.[177] Commercial available optical fibers

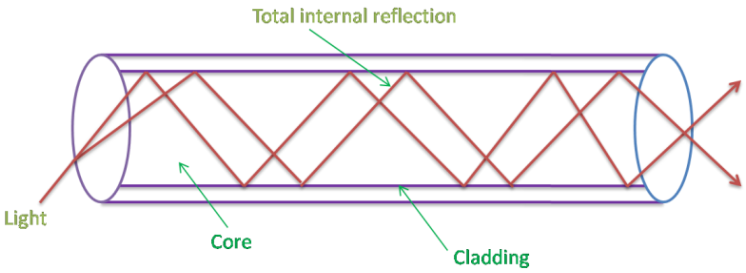

Figure 1.35: *Schematic representation of TIR.*

are much thicker than human hair (10 – 100 μm) and those were synthesized by transparent polymers or silica. These fibers are consists of core and cladding, where refractive index (n) of core is more than that of cladding. Consequently, light will be transmitted inside the core due to the total internal reflection (TIR). When light shine at critical angle through a medium of higher refractive index than its outside, light would be reflected within in the medium rather than outside. This phenomenon called TIR and is necessary to study wave guiding property of materials; it was graphically depicted in the *Figure 1.35*. Due to the high refractive index (n ~ 1.56-1.6) of the organic crystals they confine photons and propagate them depending upon the geometry of the crystals. Organic optical waveguides are classified into two types as active waveguides[178] and passive waveguides[179] based on nature of light they propagate in the solid structures.

1.7.1 Active waveguides:

In active waveguide materials absorbs the input laser radiation and propagates emitted fluorescence (FL) light towards output of that material. This has been understood clearly by exciton polaritons (EP) mechanism. Electron-hole pair has been called as exciton and polariton is coupling of the exciton pair with electromagnetic radiation. The active wave guiding character in the form of propagation of EPs in luminescent one dimensional (1-D) organic dye and microrings have been demonstrated recently.[180] Low group velocities,[181] and large refractive index[182] of EPs have led show extraordinary propagation properties[183] of EPs, which allows EPs to move at the wavelength scale and sub wavelength scale organic fiber materials. These properties have given a chance to construct EP-dependent miniaturized nanophotonic devices and circuits. Mostly active wave guiding behavior has been observed in 1D

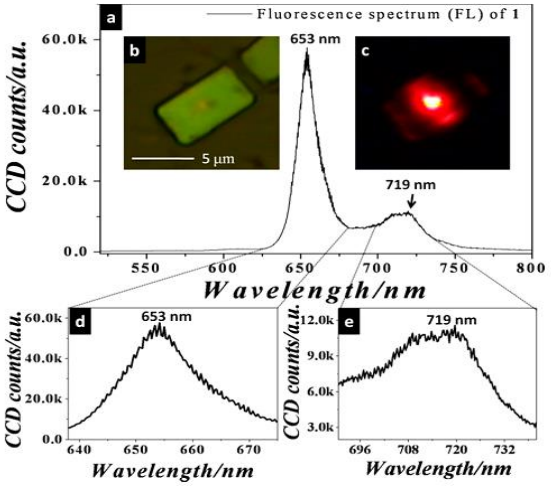

Figure 1.36*: (a) Spatially resolved fluorescence spectrum (backscattered geometry) of a nanosheet obtained upon 532 nm laser excitation at the centre of a sheet. Inset show (b) bright-field image of a sheet and (c) dark field images of a sheet with a 532 nm LPEF. (d, e) Magnified regions of the 653 nm and 719 nm peak displaying optical modes. Adopted from ref. 184.*

materials. Recently, our group demonstrated the active waveguide nature in hexagonal 2-D sheets made up of 5, 10, 15, 20-tetra(p-tolyl)porphyrin (**1**).[184] A laser 532 nm (Nd:YAG) laser was employed as point illumination source to excite electron from hexagonal sheets which was made up of **1**. As a result of illumination of laser by laser confocal fluorescence microscope, strong red fluorescence observed at 653 and 719 nm from the nanosheets. Whole phenomenon was pictuarized in fluorescence spectrum of *Figure 1.36* where bright field images of nanosheets and dark field image of sheets with long pass edge filter (LPEF) and fluorescence spectrum were mentioned.

1.7.2 Passive waveguides:

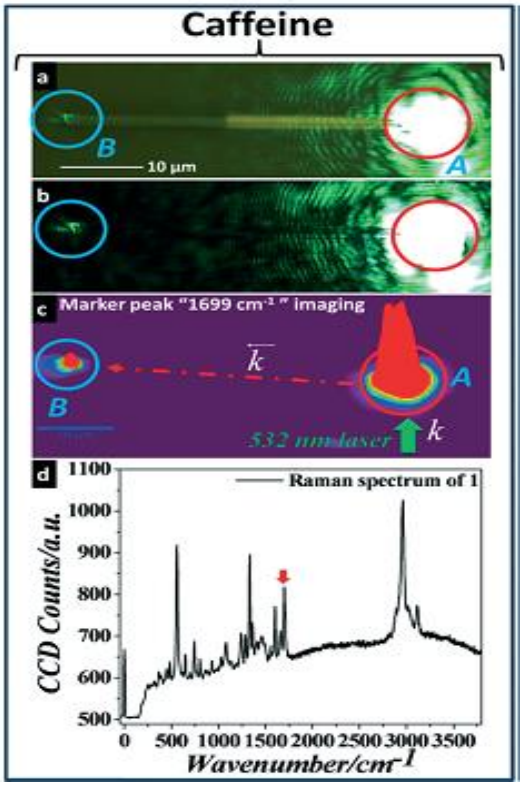

***Figure 1.37**: Passive waveguiding property of nanotubes achieved from 1: Bright field image (a), dark field image (b), SNOM (c) and Raman spectra of **1** (d). Adopted from ref. 186.*

In 2012, for the first time our group at University of Hyderabad has discovered the passive wave guiding phenomenon utilizing self-assembled organic sub microtubes and rods.[185] The functioning of passive organic waveguides resembles with commercial available optical fibers, which means that input light propagates directly along the organic substance towards the other end (output). Passive wave guiding materials will avoid photo luminescence (PL) and guide the light directly to the output end without changing wavelength unlike active waveguides. The refractive index (n) of the organic solid must be greater than air (n = 1) in order to couple and guide an optical wave through organic substance. Passive wave guiding nature can be manifested in nanotubes[186] of a pharmaceutical drug such as caffeine. Bottom illumination of a laser beam 532 nm (Nd:YAG) orthogonally at the input point A (*Figure 1.37a*) of a single tube of 50 μm long has displayed a guided propagation of the laser towards the output point B. Moreover the dark field image confirmed outgoing laser light at point B (*Figure 1.37b*).

During the propagation, the light may generate Raman scattering depending on the orientation of the molecules within the organic tube. Raman scattering also can be utilized to prove 2D confinement laser light within the organic tube. Raman mapping was done for wave guiding

tubes of **1** using the high intensity peak appeared at 1699 cm^{-1} (*Figure 1.37*d).The result showed a strong and weak Raman signals from point A and B, respectively and no detectable signals from the body of the tube (*Figure 1.37c*). Raman signal observed at output point B further affirmed that laser light was propagated from A to B. Study of passive organic waveguides under laser light propagation by using Raman spectroscopy is one of the methods to detect defect in the nano/microscale solid structures.

1.8 Drug delivery:

The last chapter of thesis work also deals with exploitation nano-organic vesicles for drug delivery studies. Hence a brief background also will be given on the concept of nano drug delivery and Zebrafish model system.

1.8.1 Nano drug carriers:

For many years, usage of medicines for an acute diseases or a chronic illness has been achieved by drug delivery to the patients through various pharmaceutical dosage forms like pills, capsules, tablets, creams, ointments, aerosols, liquids, injectable and suppositories as carriers. To attain and then to maintain the drug concentration administered within the therapeutically effective range needed for treatment, it is necessary to take this kind of drug delivery systems several times in a day. This results in a fluctuated drug level and consequently unwanted toxicity and low efficiency. To overcome this fluctuation, novel drug delivery systems had been developed, which consists of liposomes, niosomes, dedrimers, microspheres, nanoparticles, microemulsions, magnetic microcapsules, nanotubes, synthetic polymeric systems such as micelles, vesicles and impalatable pumps.[187, 188] The concept of drug delivery designed for trying to concentrate the drug in the tissues of interest while decreasing the relative concentration of the medication in the rest of tissues. As a result of this, drug will be localized on the targeted site. Therefore surrounding tissues won't be affected by the drug, leading to achieve maximum efficiency of the medication.[189] While loading

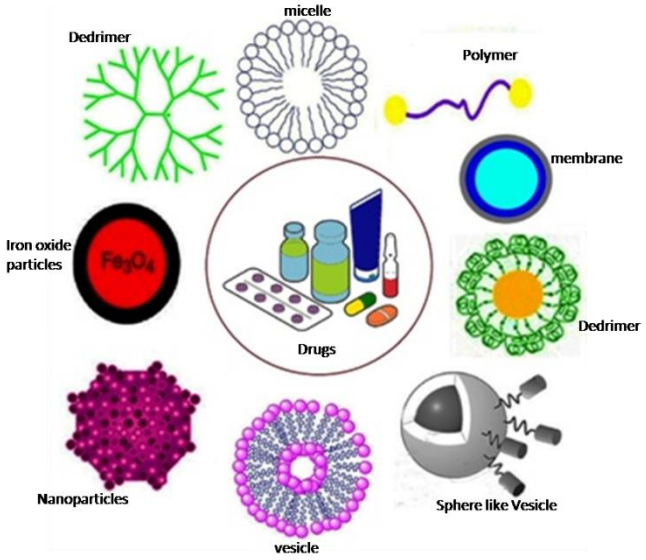

***Figure 1.38**: Various kinds of drug carriers for drug delivery. Adopted from Asian Journal of Biomedical and Pharmaceutical Sciences, Vol 2, No 14 (2012).*

drug in to a delivery system, whole drug may not enter inside the carrier, the efficiency of drug loading is calculated as follows.[190]

Efficiency of drug loading = (Drug fed by carrier-Drug loss by carrier)/Drug fed by carrier x 100%

1.8.2 Vesicles as drug carriers:

Various drug delivery systems have been developed to improve efficiency of treatment and drop the drug at specific site and meet the appropriate drug demand of the body.[191] Vesicular drug delivery systems are one of the best delivery systems, because vesicles are highly ordered assemblies of several concentric lipid bilayers, when amphiphillic building blocks are confronted with water. There are several vesicular drug delivery systems have been developed such as liposososome, niosomes, ethosomes, colloidosomes, sphinosomes, transfersomes, herosomes, pharmacosomes and cubosomes etc. Vesicular drug system can prolong the existence of the drug in systemic circulation and decrease the toxicity.[192] These drug delivery leading to the improvement of systems that permits drug targeting and controlled release of conventional medicines.[193] In the case of intracellular infections, chemotherapy is not appropriate due to limited permeation of medicine in to cell. This problem can be overcome by the use of vesicular drug delivery systems because vesicles can easily entre into cells. Vesicular drug delivery systems have lot of advantages, few of them are mentioned below.

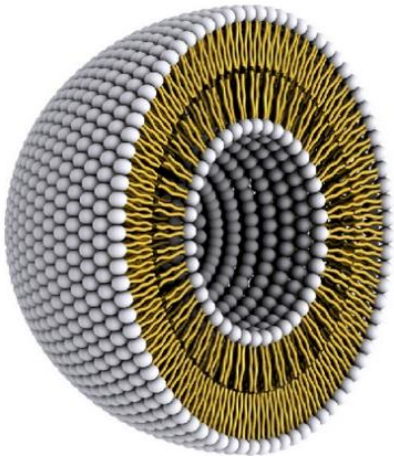

***Figure 1.39**: Vesicle of liposomes. Head= phosphate, tail= fatty acid alkyl chains. Adopted from VIDA lifesciences.*

a. Improves the bioavailability mainly in the case of less soluble drugs

b. Reduces the toxicity and prolong the existence of the drug in systemic circulation.

c. Delays removal of rapidly metabolizable drugs and thus works as sustained release systems.[194]

d. Both hydrophilic and hydrophobic drugs can be incorporated.

Liposomes were discovered by Dr Alec D. Bangham at Babraham University of Cambridge in 1961.[195] In the above *Figure 1.39*, vesicle of liposomes was presented and these are nearly spherical and unilamellar bilayer vesicles derived from lipids alternating with aqueous sections.[196] All liposomes have a compartmental structure such a way that which carries and accommodate various medicinal substances[197] to drop at specific site where the need is.

1.8.3 Zebrafish organism model for the drug assessment:

Generally, both human diseases and possible drug candidates had been modeled in mammals because of similar homology of between the mammalian genomes.[198] Typically, dogs and rats are used in toxicology experiments but mice are used in efficacy models. However predicting mammalian models is quite expensive and time consuming, and this yields a disconnection between in vivo and vitro data preventing reliable predictive effects on efficacy, toxicity and biodistribution. One of the best models for the studies of toxicity is Daniorerio, commonly called as Zebrafish. The Zebrafish organism model attracted attention of scientists to assessing drug toxicity and numerous studies confirmed that Zebrafish and mammalian toxicityprofiles are strikingly similar.[199] Zebrafish are inexpensive, small size, easy to maintain and a single spawning will give around 100-200 eggs. Adult Zebrafish length is 3 cm long whereas Larvae are only 1-4 mm long and fish can live for 7 days in a well of a standard 96- or 386-wellmicrotiter plate supported by nutrients stored in the yolk sac. Zebrafish is transparent and its larvae are able to absorb small molecules through skin and gills in water. In figure the growth of Zebrafish has been given in which different stages of fish growth were clearly understood. At 72 hours post fertilization (hpf), drugs can be introduced orally into fish because at this stage, Zebrafish begin to swallow. Fish develop discrete tissues and organs such as heart, liver, pancreas, brain, kidney, bones, muscles, intestines, sensory organs and nerve system at 120 hpf. These tissues and organs have shown to be similar to their mammalian counterparts at the physiological, anatomical, and molecular levels. That is why the study of drug assays via Zebrafish becoming so popular.[200]

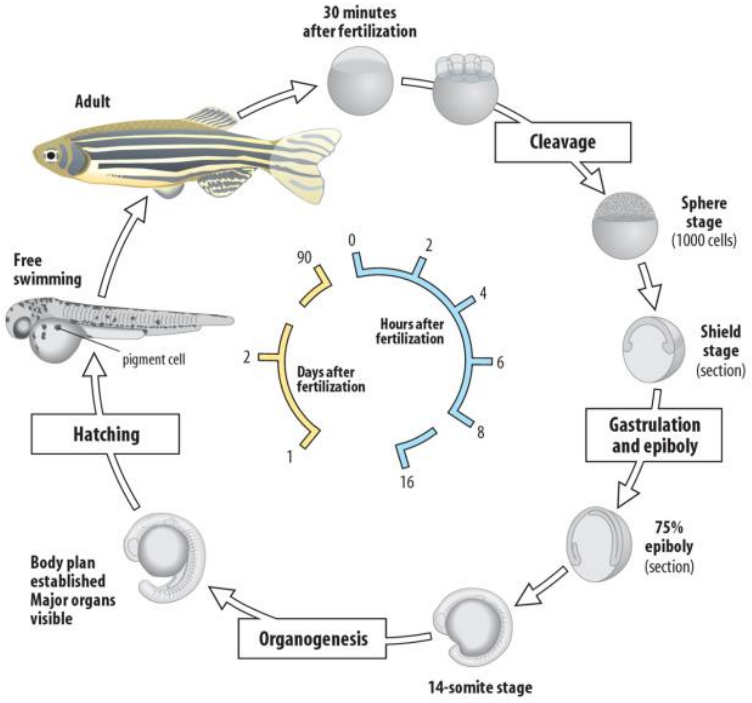

Figure 1.40*: The growth of adult Zebrafish from 30 minutes after fertilization of its embryo. Adopted from ref. 200.*

Heart is the first organ to develop and starts beating by 22 hpf and Zebrafish had been proven that it is good model for assessing drug-induced cardio toxicity.[201] Even though Zebrafish

and mammalian hearts have different structures, they show similar functional characteristics as follows.

a. Blood flows from a major vein atrium into an atrium.
b. Blood moves via a ventricle to entre in to the aorta.
c. Valves will direct blood stream.
d. An electrical system controls rhythm.
e. Endo cardium musculature leads a high-pressure system.
f. Heart beat is related with pacemaker's work function.

Mainly, the pharmacologic responses on heart of Zebrafish are strikingly similar to human.[202] Electrocardiogram (ECG) of adult Zebrafish has been proven that heart function of Zebrafish is similar to human as presented in *Figure 1.41*. Drug influence on cardiac functions, including heart rate, contractility, rhythmicity and circulation can be assessed visually in Zebrafish at 48 hpf by dissecting microscope. Drugs like terfenadine, clomipramine, mitoxantrone and thioridazine have shown to elicit cardiomyo-pathy, negative intropic effects, arrhypramine in humans. These drugs also cause abnormal atrial and ventricular (AV) ratio, bradycardia, reduce contractility and slow circulation in Zebrafish. Therefore, in conclusion, usage of Zebrafish in drug assessment will reduce reliance on drug assay in higher vertebrates.

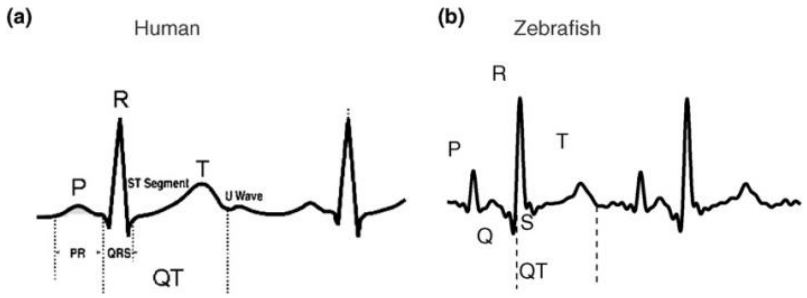

Figure 1.41*: ECG of Human and Zebrafish. Adopted from ref. 202.*

Overview of the thesis:

One of the main aims of this thesis is the creation of nano/micro scale assemblies from spin crossover (SCO) metal complexes and polymers which are soluble and sufficiently stable to be processed and characterized in both solution and solid state. For these requirements, metal-weak field ligand coordination bonds seem to be best suited to realize SCO complexes and polymeric chains. The 2,6-(Bis-pyrazolyl-pyridine)(BPP) ligand is particularly suited for this purpose due to its easy synthetic accessibility and the well-defined complexation behavior with various transition metal ions. BPP is a tridentate ligand which is combination of two pyrazole rings attached at 2,6-positions of pyridine ring. Since pyrazole is weak filed ligand, there is a possibility to switch the spin state of the metal ion when BPP makes complex with transition metal ions. Hence chemistry of BPP has been attracting attention of scientists due to its importance in synthesis of coordination compounds, biological active molecules and nano/micro materials. The present thesis work reports on the construction and through characterization of many functional derivatives of monotopic and ditopic BPP ligands with Fe(II) and also their usesage as such (without metal ions) for generating soft vesicular assemblies for drug delivery applications. Furthermore thiol-stabilized gold nanoparticles (Au NPs) were also prepared by using BPP functionalized with thiol groups. This entire thesis presents the opportunities of BPP chemistry in coordination chemistry, self-assembly, materials science such as in medicine and nanotechnology.

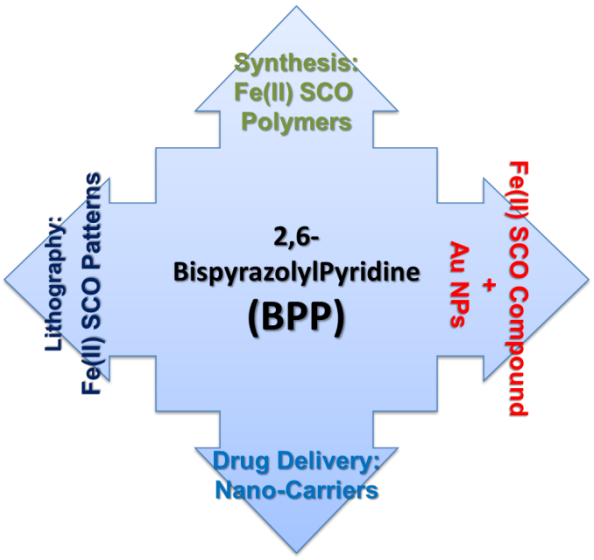

***Figure 1.42**: Over view of the thesis work*

In the beginning the introduction chapter describes few aspects of nanomaterials, its characterization and their classification. Moreover methods for size reduction such as top-down and bottom-up methods have been shown clearly. Furthermore introduction to the role of weak interaction in the self-assembly of molecules, spin crossover compounds, polymers, gold nanoparticles stabilization and their nanofabrication by various lithographic techniques also have been reviewed. Finally this chapter has also presented the importance of zebrafish organism for the drug assessment through vesicular drug carriers.

One of the aims of this thesis was to synthesis of solution processable Fe(II) SCO coordination polymer with back-to-back coupled 4-octyl-2,6-bispyrazolylpyridine units bridged by terphenyl unit (Chapter 2). It was expected that the good solubility of the ligand in simple organic solvents like DCM and THF and etc, assist the formation of nano-assemblies via bottom-up approach. Moreover 1-D array of SCO nanotapes were also fabricated by using lithographic controlled wetting (LCW) technique for SCO-based memory storage devices.

Study of SCO effect under external stimuli such as temperature, pressure and light has been established long back. In chapter 3 of this thesis work, study of SCO effect has been extended down to nanolevel under propagating guided light. In order to achieve this, organic ligand nanorod (self-assembled ligand) coated with SCO nanoparticles (ligands + Fe(II) + surfactants) were prepared by reverse micelle mechanism through the combination of ditopic BPP ligand and $Fe^{II}(BF_4)_2$ in presence of surfactants. The SCO curves have shown difference due to size and chemical environment of nanoparticles compared to the bulk state. Interestingly the organic nanohybrid has shown wave guiding property under visible laser light irradiation. This experiment demonstrated the future opportunity to study SCO effect at nanolevel under remote light irradiation.

Further in Chapter 4 of this thesis work was aimed to examine SCO effect via propagating plasmonic generation by thiol stabilized gold nanoparticles (Au NPs) appended to BPP. Six step synthetic protocol was employed to synthesize thiol stabilized Au NPs appended to BPP in presence of $Fe(ClO_4)_2$. Mixture of NPs like spherical, cubic and triangle were observed by TEM studies; and characterized by UV and TGA techniques. In order to get plasmon propagation the Au NPs carrying SCO complexes were patterned by using lithographic technique. These micro stripes have allowed future possibility to monitor SCO effect through SERS excitation via propagating plasmon.

Chapter 5 examines the synthesis of biocompatible vesicular drug carriers made of BPP and acetyl cytosine separated by long chain alkyl chains. This ligand is able to produce various kinds of nanostructures like vesicles, pearl-chain like morphology and nanotubes, which are conformed by SEM, AFM and TEM techniques. Since zebrafish teratogenicity assay study revealed that this ligand is nontoxic, a polymer protected vesicles were used as drug carriers in a model organism zebrafish. Stability of PEG protected nanovesicles found to be 72 hours which was proven by TEM results. Here terfenadine is used as model drug which shows effect on heart of the zebrafish.

References:

1. Gleiter.; *Prog. Mater Sci.* **1989***, 33*, 323.
2. (a) R. Feynman, **1959**,*There is plenty of room at the bottom* (Caltech: American Physical Society) http://www.its. Caltech.edu/~ Feyman/plenty.html; (b) R. P. Feynman, *Eng. Sci*. **1960**, *23*, 22.
3. Drexler, K. E.; *Engines of Creation: The Coming Era of Nanotechnolog.* Publisher-Doubleday,**1986***.*
4. Rein , V.; Ulijn .; Andrew, M.; Smith. *Chem. Soc. Rev*. **2008**, 37, 664–675.
5. Pease, R. F.; Chou, S. Y. *Proceedings of the IEEE*. **2008**, *96*, 248-270.
6. Sze, S. M. *Semiconductor Devices, Physics and Technology*, Publisher-John Weily & Sons, autharized reprint by wiley India, 2nd Edition, **1985**.
7. Madou, M. J. *Fundmentals of Microfabrication*, *2nd Edition, CRC Press*, **2002**.
8. Elwenspoek, M.; Jansen, H. V. *Silicon Micromachining*, *Cambridge University Press*, **1998**.
9. Bardeen, J.; Brattain, W. H. *Phys. Rev*. **1948**, *74*, 230.
10. Reichmanis, E.; Nalamasu, O. *Science*. **2002**, *297*, 349.
11. Early*, K;* Schattenburg*,* M*;* Smith, H*. Microelectron. Eng.* **1990**, *11*, 1-4.
12. Odom, T. W.; Love, J. C.; Wolfe, D. B.; Paul, K. E.; Whitesides, G. M. *Langmuir*. **2002**, *18*. 5315-5320.
13. Zhao, X. M.; Xia, Y.; Whitesides, G. M. *Adv. Mater*. **1996**, *8*, 837-840.
14. Dalton, L. R.; Harper, A. W.; Wu, B.; Ghosn, R.; Laquindanum, J.; Liang, Z.; Hubbel, A.; Xu, C. *Adv. Mater*. **1995**, *7*, 519 - 540.
15. Peppas, N. A.; Langer, R. *Science*. **1994**, *263*, 1715-1720.
16. (a) Ozbay, E.; Michel, E.; Tuttle, G.; Biswas, R.; Sigalas, M.; Ho, K. M. *Appl. Phys. Lett.* **1994**, *64*, 2059 - 2061. (b) Joannopoulos, J. D.; Villeneuve, P. R.; Fan, S. *Nature.* **1997**, *386*, 143 -149.
17. Zhao, X. M.; Smith, S. P.; Waldman, S. J.; Whitesides, G. M.; Prentiss, M. *Appl. Phys. Lett*. **1997**, *71*, 1017 - 1019.
18. Kim, E.; Xia, Y.; Whitesides, G. M. *Nature.* **1995**, *376,* 581 - 584.
19. Xia, Y.; Kim, E.; Whitesides, G. M. *Chem. Mater.* **1996**, *8*, 1558 - 1567.
20. Nelson, C. J.; Coggio, W. D.; Allcock, H. R. *Chem. Mater.* **1991**, *3*, 786.
21. Xia, Y.; Tien, J.; Qin, D.; Whitesidess, G. M. *Langmuir*. **1996**, *12*, 4033-4038.
22. Zhao, X. M.; Stoddart, A.; Smith, S. P.; Kim, E.; Xia, Y.; Prentiss, M.; Whitesides, G. M. *Adv. Mater*. **1996**, *8*, 420 - 424.
23. Kumar, A.; Biebuyck, H.; Whitesides, G. M. *Langmuir,* **1994**, *10*, 1498.
24. Kim, E.; Xia, Y.; Whitesides, G. M. *J. Am. Chem. Soc*. **1996**, *118*, 5722 - 5731.
25. Kim, E.; Xia, Y.; Whitesides, G. M. *Adv. Mater*. **1996**, *8,* 245 - 247.

26. Niino, H.; Yabe, A. *Appl. Phys. Lett*. **1992**, *60(21)*, 2697-2699.
27. Delamarche, E.; Bernard, A.; Schmid, H.; Michel, B.; Biebuyck, H. *Science.* **1997**, *276*, 779 – 781
28. (a) Trau, M.; Yao, N.; Kim, E.; Xia, Y.; Whitesides, G. M.; Aksay, I. A. *Nature*. **1997**, *390*, 674 – 676. (b) Lochhead, M. J.; Yager, P. *Mater. Res. Soc. Symp. Proc*. **1997**, *444*, 105 - 110.
29. (a) Ajayan, P. M.; Iijima, S. *Nature.* **1993**, *361*, 333 -334; (b) Dujardin, E.; Ebbesen, T. W.; Hiura, H.; Tanigaki, K. *Science*. **1994**, *265*, 1850 – 1852.
30. Martin, C. R. *Science*. **1994**, *266*, 1961 - 1966.
31. Kim, E.; Whitesides, G. M. *J. Phys. Chem. B*. **1997**, *101*, 855 - 863.
32. Pease R. F.; Chou, S. Y. *Proc. IEEE*. **2008**, *96*, 248- 270.
33. Gates, B. D.; Xu, Q.; Stewart, M.; Ryan, D.; Willson, C. G.; Whitesides, G. M. *Chem. Rev.* **2005**, *105,* 1171-1196.
34. Menon, R.; Patel, A.; Gil, D.; Smith, H. I. *Mater. Today*. **2005**, *8*, 26-33.
36. Chiu G. L. T.; Shaw, J. M. *J. Res. Develop*. **1997**, *41*, 3-6.
37. Moreau, W. M. *Semiconductor lithography: Principles, Practices and Materials. Plenu Publishing*. **1988**.
38. Elliott, D. J.; *Integrated circuit fabrication technology,* 2nd ed. Springer, **1989**.
39. Neureuther, A. R.; Rubinstein, J. J.; Chin, E.; Wang, L.; Miller, M.; Clifford, C.; Yamazoe, K. *J. Appl. Phys*. **2010**, *49,* 06GA01.
40. Sanders, D. P. *Chem. Rev*. **2010**, *110*, 321-360.
41. Liebmann, L. W.; Mansfield, S. M.; Wong, A. K.; Lavin, M. A.; Leipold, W. C.; Dunham, T. G. *J. Res. Develop*. **2001**, *45*, 651-665.
42. Wagner C.; Harned, N. *Nat. Photon*ics. **2010**, *4*, 24-26.
43. Gates, B. D.; Xu, Q.; Stewart, M.; Ryan, D.; Willson, C. G.; Whitesides, G. M. *Chem. Rev*. **2005**, *105*, 1171-1196.
44. Thompson, L. F.; Willson, C. G.; Bowden, M. J.; *Introduction to Microlithography*. Washington, DC: Oxford Univ. Press, **1983**.
45. Balzani, V.; Credi, A.; Venturi, M. *Chem. Eur. J*. **2002**, *8,* 5524-5532.
46. Muthukumar, M.; Ober, C. K.; Thomas, E. L. *Science.* **1997**, 277, 1225.
47. Ruokolainen, J.; Makinen, R.; Torkkeli, M.; Makela, T.; Serimaa, R.; Brinke, G. T.; Ikkala, O.; *Science*. **1998**, *280*, 557.
48. Park, C.; Cheng, J. Y.; Fasolka, M. J.; Mayes, A. M.; Ross, C. A.; Thomas, E. L.; Rosa, C. D. *Appl. Phys. Lett*. **2001**, *79*, 848.

49. Huang, E.; Mansky, P.; Russell, T. P.; Harrison, C.; Chaikin, Register, R. A.; Hawker, C. J.; Mays, J. *Macromolecule*s. **2000**, *33*, 80.
50. Thurn-Albrecht, T.; Rouchey, J. D.; Russell, T. P.; Jaeger, H. M. *Macromolecules*. **2000**, *33*, 3250.
51. Birol, H.; Rambo, C. R.; Guiotokuc, m.; Hotzab, D. *RSC Adv*. **2013**, *3*, 2873–2884.
52. Ulijn, R. V.; Smith, A. M. *Chem. Soc. Rev*. **2008**, *37*, 664–675.
53. Nuzzo, *R. G.;* Allara*, D. L.; J. Am. Chem. Soc.* **1983**, *105*. 4481.
54. *Whitesides, G. M.; Mathias, J. P.;* Seto, C. T. *Science.* **1991***, 254,* 1312–1319. *(b)* Zhang, S. *Nature Biotechnol.* **2003,** *21,* 1171–1178.
55. Capito, R. M.; Helena S. Azevedo, H. S.; Yuri S. Velichko, Y. S.; Alvaro Mata, A.; Stupp, S. I. *Science.***2008**, *319*, 1812–1816.
56. Lanyon, B. P.; Whitfield, J. D.; Gillett, G. G.; Goggin, M. E.; Almeida, M. P.; Kassal, I.; Biamonte, J. D.; Mohseni, M.; Powell, B. J.; Barbieri, M.; Guzik, A. A.; White, A. G. *Nature Chem*. **2010**, *2*, 106-111.
57. Berl, V.; Huc, I.; Khoury, R. G.; Krische, M. J.; Lehn, J. M. *Nature*. **2000**, *407*, 720–723.
58. Ramstrom, O.; Bunyapaiboonsri, T.; Lohmann, L.; Lehn, J. M. *Biochim. Biophys. Acta*. **2002**, *1572*, 178–186.
59. Lehn*, J. M.; Angew. Chem. Int. Ed.* **1988***, 27, 89-112.*
60. Pauling, L. *The Nature of the Chemical Bond*, Cornell University Press, Ithaca, **1960**.
61. Arunan, E.; Desiraju, G. R.; Klein, R. A.; Sadlej, j.; Scheiner, S.; Alkorta, I.; Clary, D. C.; Crabtree, R. H.; Dannenberg, J. J.; Hobza, P.; Kjaergaard, H. G.; Legon, A. C.; Mennucci, B.; Nesbitt, d. J. *IUPAC Technical Report,* **2004***.* 1-18*.*
62. Desiraju, G. R.; Steiner, T. *The Weak Hydrogen Bond*, Oxford University Press, Oxford, **1999**.
63. Rao, N. S.; Jakkar, S. K. K.; Qaurt. *J. Indian. Inst. Sci*. **1943**, *6*, 1.
64. Kollman, P. A.; Allen, L. C. *Chem. Rev.* **1972,** *72*, 283.
65. Kojic-Prodic, B.; Molcanov, K. *Acta Chim. Slov.***2008**, *55*, 692–708.
66. (a) Fecko, C. J.; Eaves, j. D.; Loparo, J. J.; Tokmakoff, A.; Geissler, P. L. *Science*. **2003**, *301*, 1698. (b) A. J. Dingley, A. J.; Grzesiek, S. *J. Am. Chem. Soc.* **1998,** *120*, 8293. (c) Xue, Z.; Suhm, M. A. *J. Chem. Phys*. **2009**, *131*, 054301. (d) Murthy, A. S. N.; Rao, C. N. R. *Appl. Spectrosc. Rev.* **1968**,*2*, 69. (e) Legon, A. C. *Chem. Soc. Rev*. **1990**, *19*, 197.
67. (a) Roberts, S. T.; Ramasesha, K.; Tokmakoff, A. *Acc. Chem. Res.* **2009***, 42*, 1239. (b) Biswal, H.; Shirhatti, R. R.; Wategaonkar, S.J. *J. Phys. Chem. A.* **2009***, 113*, 5633. (c) Maiti, S.; Patwari, G. N. *J. Phys. Chem. A*. **2009**, *113,* 1760.

68. (a) Andrew, M.; Smith, Richard, J.; Williams.; Claire Tang.; Paolo Coppo.; Richard, F.; Collins. *Adv. Mater*. **2008**, *20,* 37–41. (b) Rein, V.; Ulijn.; Andrew, M.; Smith. *Chem. Soc. Rev.* **2008**, *37,* 664–675. (c) Checot, F.; Lecommandoux, S.; Klok, H. A.; Gnanou, Y. *Eur. Phys. J*. **2003**, *E 10*, 25–35.

69. Zhao, X.; Pan, F.; Xu, H.; Yaseen, M.; Shan, H.; Hauser, C. A. E.; Zhang, S.; Lu, J. R. *Chem. Soc. Rev*. **2010**, *39*, 3480–3498.

70. Zhang, S.; Marini, D. M.; Hwang, W.; Santoso, S. *Biopolymers.* **2002***, 6,* 865–871.

71. Wheeler, S. E. *Acc. Chem. Res.* **2013***, 46,* 1029-1038.

72. Bjork, J.; Hanke, F.; Palma, C.; Samori, P.; Cecchini, M.; Persson, M. *J. Phys. Chem. Lett.* **2010**, *1*, 3407–3412.

73. Grimme, S. *Angew. Chem. Int. Ed*. **2008**, *47*, 3430 – 3434.

74. Zang, L.; Che, Y.; Moore, J. S. *Acc. Chem. Res.* **2008**, *41*, 1596-1608.

75. Marmur, A.; *J. Am. Chem. Soc.* **2000**, *122*, 2120-2121.

76. Greaves, T. L.; Drummond, C. J. *Chem. Soc. Rev.* **2013**, *42*, 1096-1120.

77. Yuan, Y.; Lee, T. R. *Surface Science techniques*, *Contact Angle and Wetting Properties, chapter-1*. Springer, **2013**, 1-34.

78. Che, Y.; Datar, A.; Balakrishnan, K.; Zang, l. *J. Am. Chem. Soc*. **2007**, *129*, 7234-7235.

79. Southall, N. T.; Dill, K. A.; Haymet, A. D. J. *J. Phys. Chem. B.* **2002**, *106*, 521-533.

80. (a) Yang, H.; Jiang, P. *Langmuir*. **2010**, *26*, 12598. (b) Bhushan, B.; Jung, Y. C.; Koch, K. *Langmuir,* **2009***, 25*, 3240. (c) Rauscher, M.; Dietrich, S. *Annu. Rev. Mater. Sci.* **2008**, *38*, 143. (d) Fei, K.; Chiu, C. P.; Hong, C. W . *Microfluid. Nanofluid*. **2008**, *4*, 321. (e) Keshavarz-Motamed, Z.; Kadem, L.; Dolatabadi, A. *Microfluid. Nanofluid*. **2010**, *8*, 47.

81. Gleiter. *Prog. Mater Sci*. **1989**, *33*, 323.

82. Ozin, G. A.; Arsenault, A. C.;' Ludovice, C. Nanochemistry-A: *A Chemical Approach to Nanomaterials.* 2d Edition, Publisher- RSC, **2012**, ISBN 978-1-84755-895-4.

83. (a) Cavallini, M.; Biscarini, F.; LLon, S.; Zerbetto, F.; Bottari, G.; Leigh, D. A.*Science*. **2003**, *299,* 531. (b) Jeftic, J.; Hinek, R.; Capelli, S. C.; Hauser, A. *Inorg. Chem.* **1997**, *36*, 3080 – 3087. (c) Baker, W. A.; Bobonich, H. M. *Inorg. Chem*. **1965**, *20*, 1184 – 1186. (d) Bousseksou, A.; Boukheddaden, K.; Goiran, M.; Consejo, C.; Boillot, M. L.; Tuchagues, J. P. *Phys. Rev. B*. **2002**, 65172412. (e) Decurtins, S.; Gutlich, P.; KPhler, C. P.; Spiering, H.; Hauser, A. *Chem. Phys. Lett*. **1984**, *105*, 1–4.

84. Gutlich, P.; Garcia, y.; Goodwin, H. A. *Chem. Soc. Rev*. **2000**, *29*, 419–427.

85. Basak, S.; Hui, P.; Chandrasekar, R. *Chem. Mater*. **2013**, *25*, 3408–34.

86. Chandrasekhar, N.; Chandrasekar, R. *Dalton Trans*. **2010**, *39*, 9872–9878.

87. Konig.; Madeja. *Chem. Commun*. **1966**, *3*, 61-62.

88. Figgis, B. N.; Introduction to Ligand Fields, Interscience Publishers, New York, London, Sydney, **1964.**

89. Chandrasekar, R.; Schramm, F.; Fuhr, O.; Ruben, M.; *Eur. J. Inorg. Chem*. **2008**, 2649–2653.

90. Goodwin, H. A.; Kucharski, E. S.; White, A. H. *Aust. J. Chem*. **1983**, *36*, 1115.

91. Dosser, R. J.; Eilbeck, W. J.; Underhill, A. E.; Edwards, P. R.; Johnson, C. E. *J. Chem. Soc. A*. **1969**, 810.

92. Chang, H. R.; McCusker, j. K.; Toftlund, H.; Wilson, S. R.; Trautwein, A. X.; Winkler, H.; Hendrickson, D. N. *J. Am. Chem. Soc.* **1990**, *112*, 6814.

93. Konig, E.; Madeja, K. *Chem. Commun*. **1966**, 61-62.

94. Guionneau, P.; Marchivie, M.; Bravic, G.; Létard, J. F.; Chasseau, *D. Top. Curr. Chem*. **2004**, *234*, 97-128.

95. Gutlich , P.; Bill, E.; Trautwein, A. X. *Mossbauer spectroscopy and transition metal chemistry*. Springer publication, Heidelberg, **2011**, ISBN 978-3-540-88427-9.

96. Hauser, A. *Chem. Phys. Lett.***1986**, *124*, 543.

97. Salata, O. V. *J. Nanobiotechnology*. **2004**, *2*, 3–8.

98. Mah, C.; Zolotukhin, I.; Dobson, J.; Batich, C.; Byrne, B. *J. Mol. Therapy.* **2000**, *1*, S239.

99. Yoshida, J.; Kobayashi, T. *J. Magn. Mater*. **1999**, *194*, 176-184.

100. Nam, J. M.; Thaxton, C. S.; Mirkin, C. A. *Science.* **2003**, *301*, 1884–1886.

101. Catala, L.; Volatron, F.; Brinzei,D.; Mallah, T. *Inorg. Chem*. **2009**, *48*, 3360–3370.

102. Catala, L.; Gloter, A.; Stephan, O.; Rogez, G.; Mallah, T. *Chem. Commun*. **2006**, 1018–1020.

103. Arai, M.; Miyake, M.; Yamada, M. *J. Phys. Chem*. **2008**, *112,* 1953–1962.

104. Moore, J. G.; Lochmer, E. J.; Ramsey, C.; Dalal, N. S.; Stiegman, A. E. *Angew. Chem. Int. Ed*. **2003**, *42*, 2741–2743.

105. Brinzei, D.; Catala, L.; Mathoniere, C.; Wernsdorfer,W.; Gloter, A.; Stephan, O.; Mallah, T. *J. Am. Chem. Soc.* **2007**, *129*, 3778–3779.

106. Gutlich, P.; Van Koningsbruggen, P. J.; Renz, F. *Recent advances in spin crossover research.* Springer*,* **2004**.

107. Real, J. A.; Gaspar, A. B.; Munoz, M. C*. Dalton Trans.* **2005***,* 2062–2079.

108. Gutlich, P. Struct*. Bonding (Berlin).* **1981***, 44,* 83–195.

109. Niel, V.; Martınez-Agudo, J.M.; Munoz, M. C.; Gaspar, A. B.; Real, J. A*. Inorg. Chem*. **2001**, *40*, 3838–3839.

110. Volatron, F.; Catala, L.; Riviere E.; Gloter, A.; St ephan, O.; Mallah, T. *Inorg. Chem*. **2008**, *47,* 6584–6585.

111. Boldog, I.; Gaspar, A.B.; Martınez,V.; Pardo-Ibanez, P.; Ksenofontov, V.; Bhattacharjee, A.; G utlich, P.; Real, J. A. *Angew. Chem*. **2008**, *47*, 6433–6437.

112. Larionova, J.; Salmon, L.; Guari, Y.; Tokarev, A.; Molvinger, K.; Moln ar, G.; Bousseksou, A. *Angew. Chem. Int. Ed.* **2008**, *47*, 8236–8240.

113. (a) Krober, J.; Codjovi, E.; Kahn, O.; Groliere F.; Martınez, C. J. *J. Am. Chem. Soc*. **1993***, 115*, 9810–9811. (b) Krober, J.; Audiere, J. P.; Claude R.; Codjovi, E.; Kahn, O. *Chem. Mater*. **1994**, *6*, 1404–1412. (c) Michalowicz A.; Moscovici, J.; Ducourant, B.; Cracco, D.; Kahn, O. *Chem. Mater*. **1995**, *7,* 1833–1842.

114. (a) Gutlich, P; Garciaa, Y.; Goodwin, H. A. *Chem. Soc. Rev*., **2000**, *29*, 419–427. (b) Viviane, A. Friese.;Dirk.; G. Kurth. *Coord. Chem. Rev*. **2008**, *252*, 199–211. (c) Chandrasekar, R.; Fuhr, O.; Kruk, R.; Ghafari, M.; Hahn, H.; Ruben, M. *Chem. Commun*. **2007**, 2636–2638. (d) Venkataramudu, U.; Chandrasekhar, N.; Basak, S.; Prasad, M. D.; Chandrasekar, R. *Macromol. Rapid Commun*. **2015**, *36*, 647-653.

115. Cobo, S.; Molnar, G.; Real, J. A.; Bousseksou, A. *Angew. Chem. Int. Ed.* **2006**, *45*, 5786 –5789.

116. (a) Fujita, M.; Kwon, Y. I.; Washiru, S.; Ogura, K. *J. Am. Chem.Soc*. **1994**, *116*, 1151. (b) Supramolecular Architecture: Bein, T., Ed.; *ACS Symposium Series 499*; *American Chemical Society: Washington, DC,* **1992**.

117. (a) Ermer, O. *Adv. Mater*. **1991**, *3*, 608. (b) Simon, I.; Andre, J. J.; Skoulios, A. *New. J. Chem*. **1986**, 295. (c) Hoskins, B. F.; Robson, R. *J. Am. Chem. Soc*. **1990**, *112*, 1546. (d) Bowes, C. L.; Ogin, G. A. *Adv. Mater*. **1996**, *8*, 13.

118. (a) Chen, C.; Suslick, K. S. *Coord. Chem. Rev*. **1993**, *128*, 293.(b) Chiang, W.; Ho, D. M.; Engen, D. V.; Thompson, M. E. *Inorg. Chem*. **1993**, *32,* 2886.

119. (a) Inoue, K.; Hayamizu, T.; Iwamura, H.; Hashizume, D.; Ohashi, Y. *J. Am. Chem. Soc*. **1996**, *118*, 1803. (b) Strumpf, H. O.; Quahab, L. Q.; Pey, Y.; Grandjean, D.; Kahn, O. *Science*. **1993**, *261*, 447. (c) Tamaki, H.; Zhong, Z. J.; Matsumoto, N.; Kida. S.; Keikawa, M.; Ashiwa, N.; Hamimoto, Y.; Okawa, H. *J. Am. Chem. Soc*. **1992**, *114*, 6974. (d) Lloret, F.; Munno, G. D.; Julve, M.; Cano, J.; Ruiz, R.; Caneschi, A*. Angew. Chem. Int. Ed.***1998**, *37*, 135. (e) Kumagai, H.; Inoue, K. *Angew. Chem. Int. Ed.***1999**, *38,* 1601. (f) Brandon, E. J.; Arif, A. M.; Burkhart, B.; Miller, J. S. *Inorg. Chem*. **1998**, *37*, 2792. (g) Retting, S. J.; Storr, A.; Summers, D. A.; Thompson, R.; Trotter, J. S. *J. Am. Chem. Soc*. **1997**, *119,* 8675. (h) Caneschi, A. Gatteschi, D.; Renard, J. P.; Rey, P. Sessoli, R. *Inorg. Chem*. **1989**, *28*, 3314.

120. Molnar, G.; Cobo, S.; Real, J. A.; Carcenac, F.; Daran, E.; Vieu, C.; Bousseksou, A. *Adv. Mater*. **2007**, *19*, 2163–2167.

121. Zhuang, Z.; Cheng, J.; Wang, X.; Yin, Y.; Chen, G.; Zhao, B.; Zhang, H.; Zhang, G. *J. Mol. Struct*. **2006**, *794,* 77.

122. Spiering, H.; Boukheddaden, K.; Linarès, J.; Varret, F. *Phys. Rev. B*. **2004**, *70,* 184 -206.

123. Decurtins, S.; Gutlich, P.; Köhler, C. P.; Spiering, H.; Hauser, A. *Chem. Phys. Lett.***1984**, *105*, 1. (b) Decurtins, S.; Gutlich, P.; Hasselbach, K. M.; Spiering, H.; Hauser, A. *Inorg. Chem*. **1985**, *24*, 2174.

124. Poganiuch, P.; Decurtins, S.; Gutlich, P. *J. Am. Chem. Soc*. **1990**, *112*, 3270.

125. Collison, D.; Garner, C. D.; McGrath, C. M.; Mosselmans, J. F. W.; Roper, M. D.; Seddon, J. M. W.; Sinn, E.; Young, N. A. *Dalton Trans.* **1997**, 4371–4376.

126. (a) Desaix, A.; Roubeau, O.; Jeftic, J.; Haasnoot, J. G.; Boukheddaden, K.; Codjovi, E.; Linares, J.; Nogues, M.; Varret, F. *Eur. Phys. B*. **1998**, *6*, 183. (b) Matsumoto, N.; Sato, T.; Hashimoto, S.; Kojima, M.; Iijima, S. *J. Phy*. **2009**, *148*, 012029.

127. Collison, D.; Garner, C. D.; McGrath, C. M.; Mosselmans, J. F. W.; Roper, M. D.; Seddon, J. M. W.; Sinn, E.; Young, N. A. *J. Chem. Soc., Dalton Trans*. **1997**, 4371–4376.

128. Sorai. M.; Seki. S. *J. Phys. Chem. Solids.* **1974**. *35*, 555.

129. Gutlich, P.; Hauser, A.; Spiering, H. *Angew. Chem. Int. Ed.* **1994**, *33*, 2024-2054.

130. Letard, J. F.; Real, J. A.; Moliner, N.; Gaspar, B.; Capes, L.; Cador, O.; Kahn, O. *J. Am. Chem. Soc*. **1999**, *121*, 10630 -10631.

131. (a) Krusin-Elbaum, L.; Shibauchi, T.; Argyle, B.; Gignac, L.; Weller, D. *Nature*. **2001**, *410*, 444 – 446; (b) Service, R. F. *Science.* **2006**, *314*, 1868 – 1870.

132. Dietzel, A. *Hard Disk Drives in Nanoelectronics and Informa-tion Technology.* Wiley-VCH, Weinheim, **2003**.

133. Eisenmenger, J.; Schuller, I. K. *Nature Mater.* **2003,** *2*, 437 – 438.

134. (a) Cavallini, M.; Gomez, J.; Ruiz, D.; Massi, M.; Albonetti, C.; Rovira, C.; Veciana, J.; Biscarini, F. *Angew. Chem*. **2005**, *117*, 910 – 914. (b) Cavallini, M.; Gomez, J.; Albonetti, C.; Ruiz-Molina, D.; Veciana, J.; Biscarini, F. *J. Phys. Chem. B.* **2006***, 110,* 11607 – 11610.

135. (a) Ruben, M.; Rojo, J.; Romero-Salguero, F. J.; Uppadine, L. H.;Lehn, J. M.*Angew. Chem.* **2004,***116*, 3728 – 3747. (b) Ruben, M.; Rojo, J.; Francisco, J.; Romero-Salguero F. J.; Uppadine, L. H.; Lehn, J. M. *Angew. Chem. Int. Ed.* **2004**, *43*, 3644 – 3662.

136. Ruben, M.; Breuning, E.; Lehn, J. M.; Ksenofontov, V.; Renz, F.; Gutlich, P.; Vaughan, G. B. M. *Chem. Eur. J.* **2003**, *9*, 4422 – 4429.

137. Bousseksou, A.; Molnar, G.; Demont, P.; Menegotto, J. *J. Mater. Chem*. **2003**, *13*, 2069. (b) Bonhommeau, S.; Guillon, T.; Daku, L. M. L.; Demont, P.; Costa, J. S.; Lotard, J. F.; Molnar, G.; Bousseksou, A. *Angew. Chem*. **2006**, *118*, 1655.

138. (a) Bousseksou, A.; Vieu, C.; Letard, J. F.; Demont, P.; Tuchagues, J. P.; Malaquin, L.; Menegotto, J.; Salmon, L. *US Patent US2005/0161728A1*. **2005**. (b) Cavallini, M.; Gomez, J.; .Ruiz, D.; Veciana, J.; Biscarini, F. *EU Patent WO/2005078521A2,***2005** and *US Patent US2007182060.***2007**.

139. Bousseksou, A.; MolnQr, G.; Cobo, S.; Salmon, L.; Real, J. A.; Vieu, C. *PCT Patent WO2007107644A1*. **2007**.

140. Cobo, S.; Molnar, G.; Real, J. A.; Bousseksou, A.; *Angew. Chem.* **2006**, *118*, 5918 – 5921.

141. Matsuda, M.; Tajima, H. *Chem. Lett.* **2007**, *36*, 700 – 701.

142. Peter, W. *The Technique of Lithography.* Publisher-(London) Batsford,**1964**.

143. Grilli, S.; Vespini, V.; Ferraro, P. *Langmuir*. **2008**, *24,* 13262–13265.

144. Basak, S.; Hui, P.; Chandrasekar, R. *Chem. Mater*. **2013**, *25,* 3408–3413.

145. Conde, J.; Fuente, J. M. D. L.; Baptista, P. V. *Pharm. Anti-Cancer Drug*. **2013**, *4*, 134.

146. Horikoshi, S.; Serpone, N. *Introduction to nanoparticles*.**2013**, 1-24.

147. Vajtai, R. *Springer handbook of nanomaterials.* Springer Dordrecht Heidelberg London New York, **2013**.

148. Brown, D. H.; Smith, W. E. *Chem. Soc. Rev.* **1980**, *9,* 217- 240.

149. Turkevitch, J.; Stevenson, P. C.; Hillier, J. *Discuss. Faraday Soc*. **1951**, 11, 55- 75.

150. Frens, G. *Nature. Phys. Sci.***1973**, *241*, 20-22.

151. Hayat, M. A. *Colloidal Gold, Principles, Methods and Applica- tions*. Academic Press, New York, **1989**.

152. Schmid, G.; Chi, L. F. *Adv. Mater*. **1998**, *10*, 515-526.

153. Mirkin, C. A.; Letsinger, R. L.; Mucic, R. C.; Storkoff, J. J. *Nature.* **1996**, 3*82*, 607.

154. Schmid, G. *Chem. Rev*. **1992**, *92*, 1709-1727.

155. Samal, A. K.; Sreeprasad, T.S.; Pradeep, T. J. *Nanopart. Res*. **2010**, *12,* 1777-1786.

156. Khan, Z.; Singh, T.; Hussain, J. I.; Hashmi, A. A. *Colloids Surf., B.* **2013**,*104,*11-17.

157. Ji, X.; Song, X.; Li, J.; Bai Y,; Yang, W.; Peng, X. *J. Am. Chem. Soc*. **2007**, *129,* 13939- 13948.

158. Pearson, R.G. *J. Am. Chem. Soc*. **1963**, *85*, 3533 – 3539.

159. Prasad, B.L.V.; Stoeva, S. I.; Sorensen , C. M.; Klabunde, K. J. *Chem. Mater*. **2003,** 15, 935 – 942

160. Giersig, M.; Mulvaney, P. *Langmuir*. **1993**, *9*, 3408-3413.

161. Brust, M.; Walker, M.; Bethell, D.; Schiffrin, D. J.; Whyman, R. *Chem. Commun*. **1994,** 801 – 802.

162. (a) Bisoyi, H. K.; Kumar, S. *Chem. Soc. Rev*. **2011**, *40*, 306–319. (b). Brust, M.; Walker, M.; Bethell, D.; Schiffrin, D. J.; Whyman, R. J. *Chem.Commun*.**1994**, 801-802.

163. Kretschmann, E.; Raether, H. *Notizen.* **1968**, *23a*, 2135-2136.

164. Michaels, A. M.; Jiang, J.; Brus, L. *J. Phys. Chem*. B. **2000**, *104*, 11965-11971.

165. Lee, J. W.; Samal, S.; Selvapalam, N.; Kim, H. J.; Kim, K. *Acc. Chem. Res*. **2003**, *36*, 621.

166. Tao, C.; An, Q.; Zhu, W.; Yang, H.; Li, W.; Lin, C.; Xu, D.; Li, G. *Chem. Commun*. **2011**, *47*, 9867–9869.

167. Eustis, S.; El-Sayed, M. A. *Chem. Soc. Rev*. **2006**, *35*, 209–217.

168. Burda, C.; Chen, X.; Narayanan, R.; El-Sayed, M. A. *Chem. Rev*. **2005**, *105*, 1025–1102.

169. Xia, Y.; Yang, P.; Sun, Y.; Wu, Y.; Mayers, B.; Gates, B.; Yin, Y.; Kim, F.; Yan, H. *Adv. Mater*. **2003**, *15*, 353–389.

170. Pileni, M. P. *Nature Mater*. **2003**, *2*, 145–149.

171. Jin, R. C.; Cao, Mirkin, C. A.; Kelly, K. L.; Schatz, G. C.; Zheng, J. G. *Science*, **2001**, *294*, 1901–1903.

172. Murphy, C. J.; Sau, T. K.; Gole, A. M.; Orendorff, C. J. G.; Gou, J. L.; Hunyadi, S. E.; Li, T. *J. Phys. Chem. B*. **2005**, *109*, 13857–13870.

173. El-Sayed, M. A. *Acc. Chem. Res*. **2001**, *34*, 257–264**.**

174. (a) Yanagi, H.; Morikawa, T. *Appl. Phys. Lett*. **1999**, *75*, 187–189. (b) Zhao, Y. S.; Fu, H.; Peng, A.; Ma, Y.; Liao, Q.; Yao, J. *Acc. Chem. Res*. **2010**, *43*, 409–418. (c) Zhang, C.; Zhao, Y. S.; Yao, J. *Phys. Chem. Chem. Phys*. **2011**, *13*, 9060–9073. (d) Zhao, Y. S.; Fu, H.; Peng, A.; Ma, Y.; Xiao, D.; Yao, J. *Adv. Mater.* **2008**, *20*, 2859–2876. (e) Balzer, F.; Bordo, V. G.; Simonsen, A. C.; Rubahn, H.G. *Phys. Rev. B.* **2003**, *67*, 115408–115415. (f) Takazawa, K.; Kitahama, Y.; Kimura, Y.; Kido, G. *Nano Lett*. **2005**, *5,* 1293–1296. (g) Zhao, Y. S.; Xu, J. J.; Peng, A. D.; Fu, H. B.; Ma, Y.; Jiang, L.; Yao, J. *Angew. Chem. Int. Ed*. **2008**, *47*, 7301–7305. (h) Balzer, F.; Bordo, V. G.; Simonsen, A. C.; Rubahn, H. G. *Appl. Phys. Lett*. **2003**, *82*,10–12. (i) Schiek, M.; Balzer, F.; Al-Shamer, K.; Brewer, J. R.; Lutzen, A.; Rubahn, H.-G. *Small*.**2008**, *4*, 176–181. (j) Zhao, Y. S.; Xu, J. J.; Peng, A. D.; Fu, H. B.; Ma, Y.; Jiang, L.; Yao, J. *Angew. Chem. Int. Ed*. **2008**, *47*, 7301–7305. (k) Zhao, Y. S.; Fu, H. B.; Peng, A. D.; Ma, Y.; Xiao, D. B.; Yao, J. *Adv. Mater*. **2008**, *20*, 2859–2876. (l) Zhang, C.; Zou, C. L.; Yan, Y. L.; Hao, R.; Sun, F. W.; Han, Z. F.; Zhao, Y. S.; Yao, J. *J. Am. Chem. Soc*. **2011**, *133,* 7276–7279. (m) Kim, F. S.; Ren, G. Q.; Jenekhe, S. A. *Chem. Mater*. **2011**, *23*, 682–732. (n) Yao,

W.; Yan, Y.; Xue, L.; Zhang, C.; Li, G.; Zheng, Q. D.; Zhao, Y. S.; Jiang, H.; Yao, J. N. *Angew. Chem. Int. Ed*. **2013**, *52*, 8713–8717.

175. Chandrasekar, R. *Phys. Chem. Chem. Phys*. **2014**, *16*, 7173-7183**.**

176. (a) Hunsperger, R. G. *Theory and Technology, Springer, Berlin, 5th edn*. **2002**.(b) Lal, S.; Linkand, S.; Halas, N. J. *Nat. Photonics*. **2007**, *1*, 641–648. (c) Yan, R. X.; Gargas, D.; Yang, P. D. *Nat.Photonics*. **2009**, *3*, 569–576. (d) Clark, J.; Lanzani, G. *Nat. Photonics*. **2010**, *4*, 438–446.

177. Kao, C. K. *Ericsson Rev*. **1979**, *56*, 92–94.

178. (a) Zhao, Y. S.; Fu, H. B.; Peng, A. D.; Ma, Y.; Xiao, D. B.; Yao, J. N. *Adv. Mater*. **2008**, *20*, 2859 2876. (b) Zhao, Y. S.; Peng, A. D.; Fu, H. B.; Ma, Y.; Yao, J. N. *Adv. Mater*. **2008**, *20*, 1661–1665. (c) Zhang, C.; Zheng, J. Y.; Zhao, Y. S.; Yao, J. *Adv. Mater*. **2011**, *23*, 1380–1384. (d) Zhang, C.; Yan, Y.; Yao, J.; Zhao, Y. S. *Adv. Mater.* **2013**, *25*, 2854–2859. (e) Zhang, C.; Zou, C. L.; Yan, Y. L.; Hao, R.; Sun, F. W.; Han, Z. F.; Zhao, Y. S.; Yao, J. N. *J. Am. Chem. Soc*. **2011**, *133*, 7276–7279. (f) Zhao, Y. S.; Fu, H. B.; Peng, A. D.; Ma, Y.; Liao, Q.; Yao, J. N. *Acc. Chem. Res*. **2010**, *43*, 409–418.

179. (a) Basak, S.; Chandrasekar, R. *Adv. Funct. Mater*. **2011**, *21*, 667–673. (b) Hui, P.; Chandrasekar, R. *Adv. Mater*. **2013**, *25*, 2963–2967. (c) Basak, S.; Chandrasekar, R. *J. Mater. Chem. C*. **2014**, *2*, 1404–1408.

180. Balzer, F.; Bordo, V. G.; Simonsen, A. C.; Rubahn, H. G. *Phys. Rev. B*. **2003**, *67*, 115408–115415.

181. Vugt, V. L. K.; Piccione, B.; Agarwal, R. *Appl. Phys. Lett*. **2010**, *97*, 061115.

182. (a) Ulbrich, R. G.; Fehrenbach, G. W. *Phys. Rev. Lett.***1979**, *43*, 963–966. (b) Chu, S.; Wong, S. *Phys. Rev. Lett*. **1979**, *48*, 738–741. (c) Andreani, L. C.; Panzarini, G.; Gerard, J. M. *Phys. Rev. B.* **1999**, *60*, 13276–13279.

183. Vugt, V. L. K.; Ruhle, S.; Ravindran, P.; Gerritsen, H. C.; Kuipers, L.; Vanmaekelbergh, D. *Phys. Rev. Lett.* **2006**, *97*, 147401–147404.

184. Chandrasekhar, N.; Mohiddon, M. A.; Chandrasekar, R. *Adv. Opt. Mater*. **2013**, *1*, 305–311.

185. (a) Chandrasekhar, N.; Chandrasekar, R. *Chem. Commun*. **2010**, *46*, 2915–2917. (b) Chandrasekhar, N.; Chandrasekar, R. *Angew. Chem. Int. Ed.* **2012**, *51*, 3556–3561;

186. Chandrasekhar, N.; Reddy, E. R.; Prasad, M. D.; Rajadurai, M. S.; Chandrasekar, R. *Cryst. Eng. Comm*. **2014**, *16,* 4696–4700.

187. Jeong, B.; Bae, Y. H.; Lee, D. S.; Kim, S. W.; Nature. **1997**, *388,* 860-862.

188. Ashutosh, L.; Suman, R.; Sidhyartha, S.; Altaf bhai, S.; Vandana, Y. M. *J. drug Deliv. therapeutics*. **2012**, *2*, 129-135.

189. Ashutosh, L.; Suman, R.; Sidhyartha, S.; bhai, S. A.; Vandana, Y. M. *J. drug deliv.therapeutics*. **2012**, *2(5)*, 129-135.

190. Saraf, S.; Paliwal, S.; Saraf, S. *Int. J. Cur. Sci. Res.***2011**, *1(2),* 63 – 68.

191. Kao, G. Y.; Change, L. J.; Allen, T. M. *Gene Ther*. **1996**, *3,* 250-260.

192. Gregariadis G. *Nature*. **1977**, *265*, 407.

193. Post, G.; Krisch, R.; Koestler, T. *Liposomes Tech. CRC Press Inc*. **1983**.

194. Kshirsagar, N. A.; Pandya, S. K.; Kirodian, B. G.; Sanath, S. *J. Postgraduate Medic*. **2005**, *51*, S5-S15.

195. Bitounis, D.; Fanciullino, R.; Iliadis, A.; Ciccolini, J.; *ISRN Pharmaceutics.* **2012**, ID 738432, doi:10. 5402/2012/738432.

196. Bangham, A. D.;Hill, M. W.; Miller, N. G. A. *J. Bioenerg Biomembr*. **1975**, *7*, 87-88.

197. Russell, R. *Neurosci. Biobehav. Rev.* **1991**, *15*, 7–11.

198. Hunter, A. J. *Drug Discov. Today.* **2008***, 13,* 9-10*.*

199. (a) Giacomotto, J.; Segalat, L. *J. Pharmacol.* **2010**, *160 (2),* 204-216. (b) Parng, C.; Anderson, N.; Ton, C.; McGrath, P. *Methods Cell Biol*. **2004**, *76*, 75–85. (c) Parng, C. *Curr. Opin. Drug Discov*. **2005**, *8,* 100–106(d) Ton, C.; Parng, C.; *Hearing Res*. **2005**, *208*, 79–88 (e) Haldi, M.; Ton, C.; Seng, W. L.; McGrath, P. *Angiogenesis*. **2006**, *9*, 139–151.

200. Parng, C. *Curr. Opin. Drug Discov. Dev.* **2005**, *8,* 100–106.

201. David, J.; Milan.; Ian, L.; Jones.; Ellinor, P. T.; Calum, A.; MacRae.; *AJP-Heart Circ Physiol*. **2006**, *291*, H269-H273.

202. McGrath, P.; Li, C.; *Drug Discov. Today*. **2008**, *13*, 394-401.

Chapter 2

Lithographically oriented 1D nano-tape arrays composed of solution processable above room temperature spin cross-over iron (II) coordination polymers

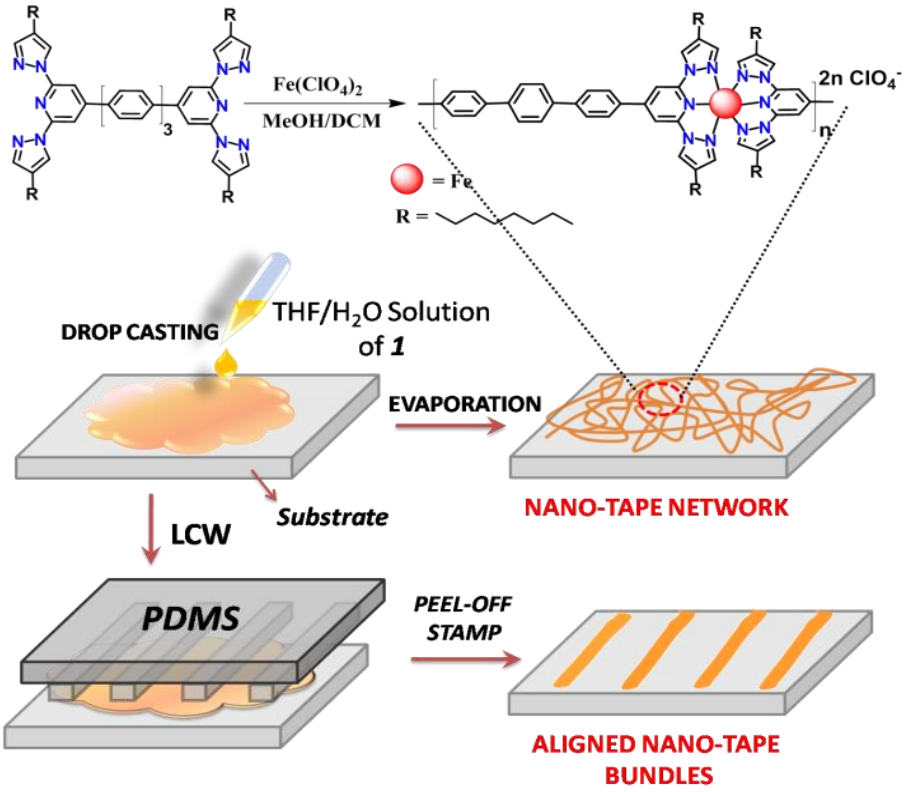

2.1 Abstract:

A novel highly soluble and solution processable Fe(II) spin cross-over (SCO) coordination polymer shows above room temperature SCO temperature at $T_{1/2}$ ~ 302 K. Bottom-up self-assembly of this supramolecular polymer in THF/water formed net-work of several micron long nano-tapes. Further solution processing using lithographically controlled wetting technique produced aligned 1D array of SCO nano-tape bundles.

This chapter has been adopted from the following publication: Botcha, A.K.; Basak,S.; Chandrasekar, R.* RSC Advances. **2014**, 4, 34760.

2.2 Introduction:

Spin cross-over (SCO) compounds displaying bistable behaviour (high-spin; HS and low-spin; LS) are perfect inorganic spin switches, and they can act as an electronic component in the construction of miniaturized nanoscale spintronic devices.[1] The current decade has seen attempts by many groups to synthesize a wide range of SCO molecules with an aim to fabricate device structures by following top-down and bottom-up approaches.[2] Mostly Fe(II) based SCO compounds are widely studies for this purpose owing to their reversible bistable HS (S=2; paramagnetic) and LS (S=0; diamagnetic) states with respect temperature, pressure, laser light and electric current.[3] Although a plethora of SCO compounds are reported in the literature, still the synthesis of solution stable and processable polymeric SCO materials are rather scarce. The reason behind is less number of publications in solution processable SCO coordination polymers is primarily attributed to the difficulty of ligand design and its synthesis. For example, to achieve soluble coordination polymers, synthesis of a novel back-to-back coupled tridentate (ditopic) ligand carrying solubilising groups is a logical route. Solution processability is one of the very imperative criteria to achieve low-cost nano/micro structures effectively adopting bottom-up or/and top-down approches.[4]

In this context, a decade back, Kurth et al. have reported the self-assembly of Fe(II) ion with a back-to-back terpyridine (terpy) ligands forming 1D coordination polyelectrolytes.[5] The authors achieved the solubility by employing anionic amphiphilic long alkyl chains and deposited them on graphite surface to form nano rods. For the first time, Ruben et al. have prepared 2,6-bispyrazolylpyridine (bpp) based Fe(II) coordination polymer displaying above room temperature SCO behaviour. Unfortunately the solubility of this polymer was rather poor, which limited its solution processability to fabricate nano/micro scale device structures. To increase the solubility of bpp coordination polymers, recently, we have synthesized a series of bpp units carrying octyl chains. We have also reported the synthesis of highly soluble Zn(II) coordination polymers from these ligands and demonstrated their superior processability by lithographically fabricating a series of well-ordered one dimensional micro patterns and arrays.[4] Till now no attempt has been made to achieve the nano/micro scale SCO polymer structures either by bottom-up (self-assembly) or top-down (solution lithography) techniques.

In this chapter we present for the first time the synthesis of a solution processable SCO Fe(II) coordination polymer $[Fe(II)(L)]_n \cdot 2nClO_4$ (**1**) using a back-to-back coupled 4-octyl-2,6-bispyrazolylpyridine bridged by terphenyl unit (**L**), its UV-visible titration studies, variable temperature magnetic susceptibility and Raman spectroscopy studies. This chapter also demonstrate the solution processabilty of **1** by fabricating isotropically distributed SCO micro-

fibres via bottom-up self-assembly approach. Furthermore a lithographic method will be discussed to align these self-assembled SCO microfibers into highly ordered anisotropic structures by following top-down lithography technique. Detailed transmission electron microscopy (TEM), atomic force microscopy (AFM) and micro-Raman analysis will also be presented.

2.3 Results and discussion:

2.3.1 Synthetic scheme:

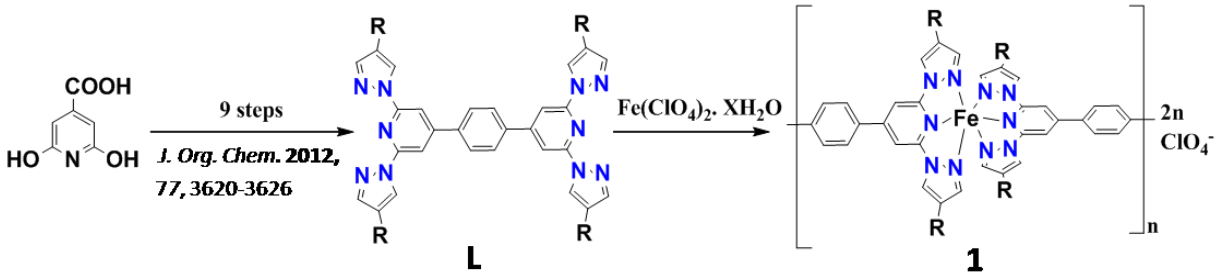

Scheme 2.1*: Synthesis of magnetically bistable SCO polymer **1** by in acetonitrile solvent.*

Ditopic ligand **L** was prepared as per our previously reported procedure.[5c] Coordination polymer **1** was prepared by using stoichiometric amount of $Fe^{II}(ClO_4)_2$ and **L** in acetonitrile solvent at room temperature as brown precipitate.

2.3.2 Synthetic procedure of 1:

The starting material for the synthesis of **1** was citrazinic acid. Ditopic ligand **L** was prepared via nine steps protocol as per the reported procedure (Scheme 2.1). A 100 mL flask was charged with **L** (30 mg, 0.0273 mmol) and 10 mL of DCM was added to it. A solution of $Fe(ClO_4)_2 \cdot 6H_2O$ (6.96 mg, 0.0273 mmol) in MeOH (10 mL) was added to the above solution. The mixture was stirred for a day under nitrogen atmosphere. Afterwards, the solvent was evaporated on a rotary evaporator in air. The residue was washed with diisopropyl ether (20 mL × 1) and dried in vacuum to get a yellow color powder of **1**. Yield 30 mg. FTIR (KBr disk; ν in cm^{-1}) 2959, 2921, 2860, 1737, 1463. Raman (488 nm Ar^+ laser; ν in cm^{-1}) 847, 994, 1202, 1290, 1459 and 1610 (C=C) cm^{-1}. UV/Vis (DCM/MeOH, L mol^{-1} (cm^{-1}): 347 nm, 285 nm, 263 nm, 230 nm.

2.3.3 Optical absorbance and emission studies of L and 1:

In order to prove the formation of coordination polymer **1**, UV-Visible and fluorescence spectroscopy studies were performed. In this regard, ligand **L** was dissolved in spectroscopic grade DCM in quartz cuvette and resultant solution has been titrated with methonolic solution of $Fe(ClO)_4$. During the titration, the intensity of the absorption bands at ~260, ~280, and 325 nm

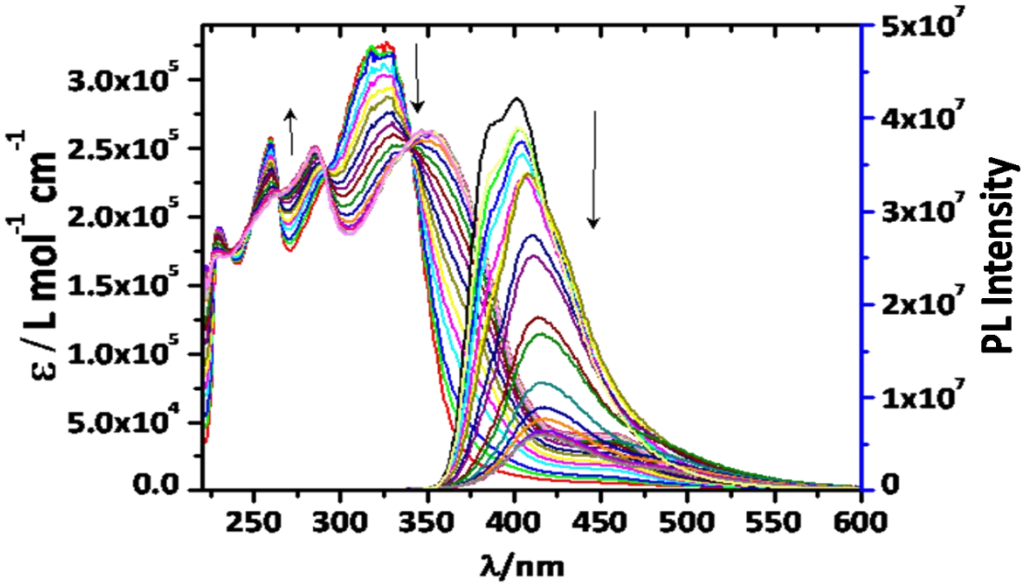

Figure 2.1*: UV–Visible and fluorescence titration spectra of ligand* ***L*** *with* $Fe^{II}(ClO_4)_2$ *in dichloromethane/MeOH at 25 °C. Arrows indicate the spectral changes with increasing amounts of Fe(II) ions.*

decreased drastically and red shifted due to the formation of 1D linear metallo-supramolecular polymer chains. The fluorescence intensity of **L** has gone down drastically with red shift, which indicates evolution polymer **1** and rising of LMCT band around 450 nm during titration gave an evidence for the presence of Fe(II) metal ion as part of **1** as mentioned in *Figure 2.1.*

2.3.4 SCO behaviour and variable temperature Raman studies of 1:

The temperature dependent magnetic susceptibility of complex **1** showed a reversible SCO behavior during the heating and cooling cycles in the temperature range of 320 K ↔ 4.2 K (*Figure 2.2*). At 320 K the product of the molar magnetic susceptibility (χT) is 2.74 emu K mol^{-1}, which is slightly lower than the expected value for a HS iron(II) ion (S=2). Upon cooling the χT value decreased sharply and reached a minimum value of 1.69 emu K mol^{-1} down to ~197 K indicating the SCO behavior. The calculated

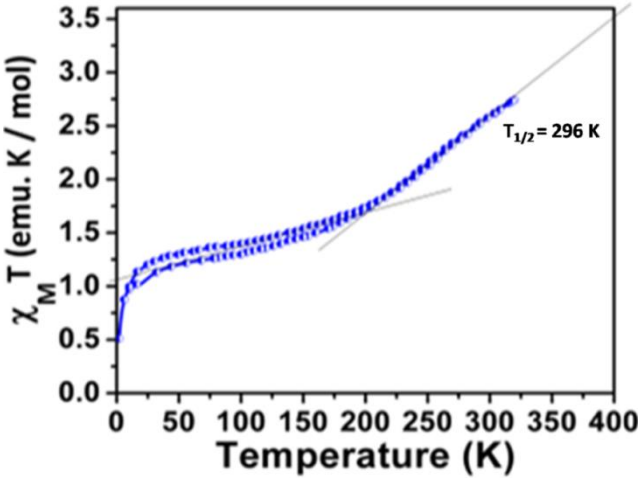

Figure 2.2*: χT vs T plot for the coordination polymer* ***1*** *measured in the temperature range of 2–350 K in the heating and cooling mode cycles with an applied DC magnetic field of 0.5T.*

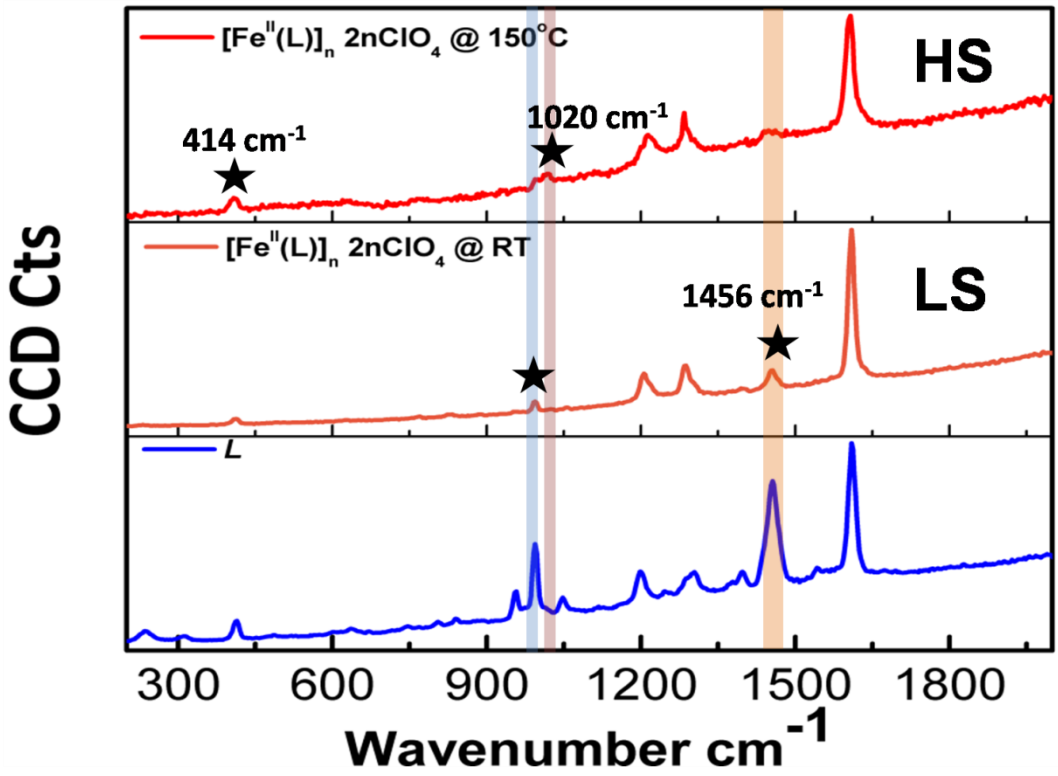

Figure 2.3*: Variable temperature Raman spectra of coordination polymer* ***1*** *in thin pellet state at 298 K, and 423 K.*

$T_{1/2}$ value of this regime is 296K using the theoretical HS state value of 3.5 emu K mol^{-1}. This value remained nearly constant for the heating and cooling cycles. Below 191 K the χT value decreased very sluggishly and reached the value of 1.28 emu K mol^{-1} at 37 K. Upon subsequent cooling the χT value dropped down abruptly to the minimum value of 0.51 emu K mol^{-1} at 2 K because of zero-field splitting of the remaining HS molecules. Furthermore in Fe(II) centered octahedral SCO compounds possessing Fe–N bonds, the (Δd) difference in the average Fe–N bond distances (d_{avg}) between the HS (1.8 Å; t_{2g}^4 eg*^{2}) and LS (2.0 Å; t_{2g}^6eg*^{0}) states is ~0.2 Å due to the population of the anti-bonding e_g* orbital in the HS state.[6] Hence variable temperature Raman spectroscopy is a very sensitive technique to probe the Raman active vibration modes associated with HS ↔ LS state structural transformations in Fe(II) complexes. This technique also can be used to confirm the complex formation due to metal coordination. The confocal Raman spectroscopy (Ar$^+$488 laser) investigations of pellet sample showed that the intensity of 1456 cm^{-1} and 994 cm^{-1} vibration modes of **L** decreased sharply after complex **1** formation. Two weak intense bands (958 cm^{-1} and 1048 cm^{-1}) of **L** also vanished completely after the formation of **1**. To probe the bond polarizability changes associated with the structural changes (HS ↔LS) during the SCO event, Raman spectra were collected both at RT and 150°C. In comparison to the room temperature, the high temperature

Raman spectrum showed disappearance and manifestation of modes at 1456 cm^{-1} and 1020 cm^{-1}, 1018 cm^{-1}, respectively (*Figure 2.3*). This result further confirms the operating thermal SCO phenomenon in **1**.

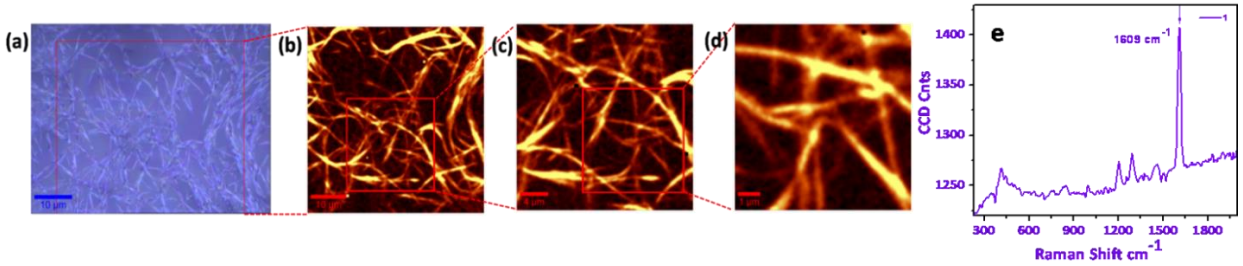

Figure 2.4*: (a) Confocal image of isotopic fibers assembled from SCO coordination polymer* ***1****. b) Corresponding Raman image of the marked area shown by red line in fig (a). c, and d) Raman images of the corresponding red line profile shown in (b) and (c) respectively. e) Raman spectrum of* ***1.***

2.3.5 Fabrication of SCO nanotapes and their characterization:

To demonstrate the solution processabilty, the SCO coordination polymer **1** was self-assembled by following bottom-up approach. At first a 500 μL of saturated THF solution of **1** was prepared and 100 μL of Millipore water was rapidly injected. Drop casting this solution on a clean

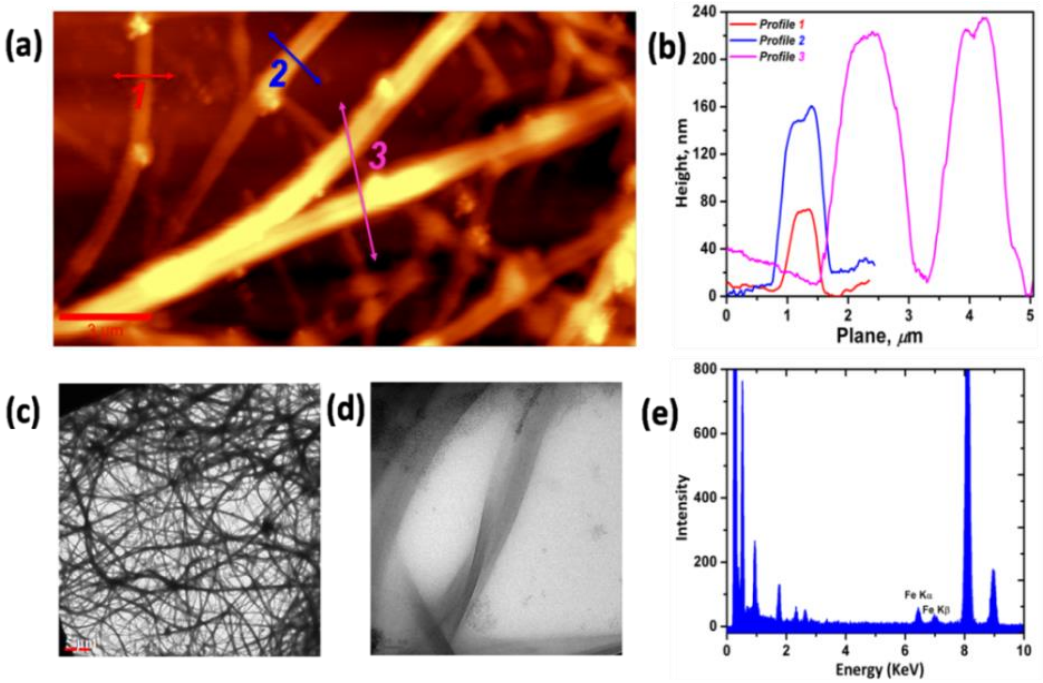

Figure 2. 5*: (a) AFM image of the SCO nano-tape bundles, (b) AFM topography along the lines shown in a, (c) TEM image of the SCO nano-tapes bundles , (d) Twisted nano-tape, (e) EDAX to conform presence of Fe.*

silica glass substrate followed by laser confocal microscopy investigation showed the formation of bundles of several micron long fibre-like structures of **1** with different scale bars as shown in *Figure. 2.4.* Raman imaging of fibre-like structures of **1** also performed by taking reference peak at 1609 cm^{-1} corresponding to the C=C stretching modes (*Figure 2.4e*). Micro Raman spectroscopy and imaging analysis evidently confirmed the chemical composition of the SCO polymer **1**. AFM topography analysis clearly indicated that fibre-like structures are indeed nano-tapes with the height and width were in range of 70-240 nm and 0.5-1.5 μm, respectively (*Figure 2.5b*). To study the nano-tapes by TEM, the sample was prepared on a carbon coated copper grid and bright-field TEM images clearly supported AFM results by displaying twisted nano-tape like features of several micron-long fibers (*Figure 2.5c, d*). Energy dispersive X-ray analysis (EDAX) further confirmed the presence of iron ion in the nano-tapes (*Figure 2.5e*).

2.3.6 Preparation and characterization of PDMS mould for lithographic studies:

Before fabrication of 1-D array SCO nano-tapes, PDMS mould was prepared as per the following procedure. PDMS viscous liquid (9 mL) was taken in a 50 mL polythene plastic container and 1 mL of curing agent has been added to it. Resultant mixture was shook well for making homogeneous solution and it was evacuated for an often hour to remove air bubbles within the solution. Afterwards resultant PDMS solution has been poured on master stamp in a plastic cap to

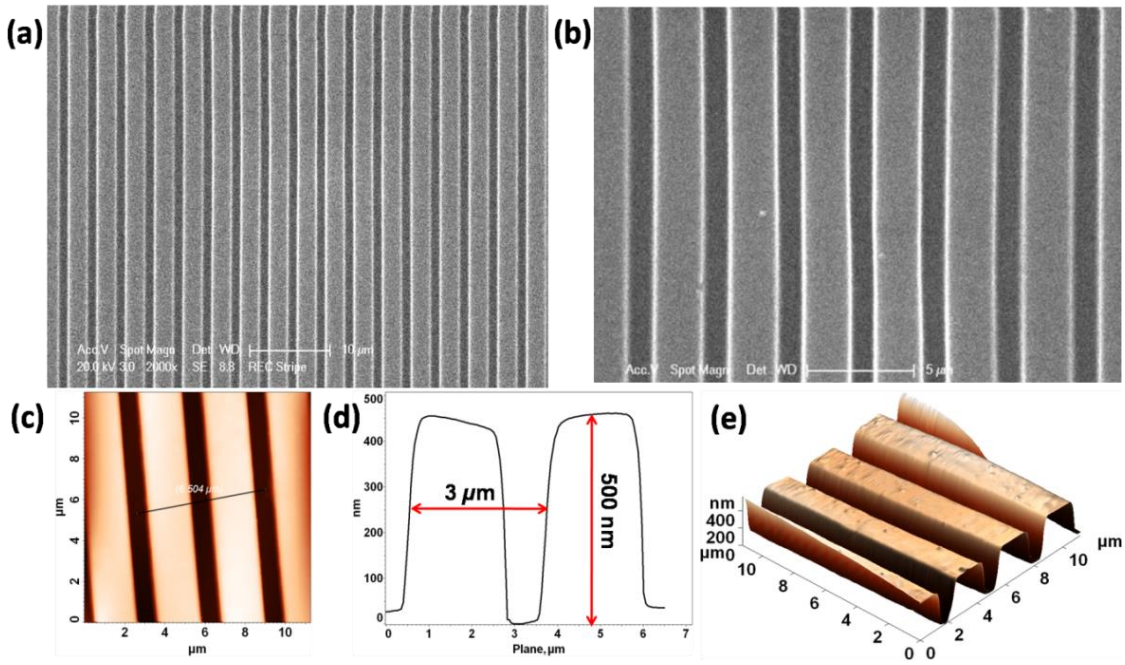

Figure 2.6*: (a, b) SEM images of rectangular pattern, (c) Noncontact mode AFM images of (a) Rectangular pattern, (d) Topographic profile of the mould, and (e) 3-D image of the mould.*

heated at 80 °C for ~6 hours to solidify it. After solidification mold was removed carefully by cutting with a blade. Finally the mold was characterized by scanning electron microscopy (SEM) and atomic force microscopy (AFM) as shown in *Figure 2.6.* Rectangular elongated pattern of PDMS mould was clearly revealed in SEM images (*Figure* 2.6*a* and *b*) of various resolutions. Moreover AFM studies affirmed the presence of rectangle 1D pattern and also height and width of the rectangle pattern were found to be ~500 nm and ~2.5 μm respectively (*Figure* 2.6*c* and *d*). Furthermore three dimensional image of AFM clearly showed the height and width of the pattern (*Figure 2.6e)*, which are 500 nm and 2 μm, respectively. The gap (channels) between adjacent stripes is ca. 1μm.

2.3.7 Fabrication of 1-D array SCO nanotapes:

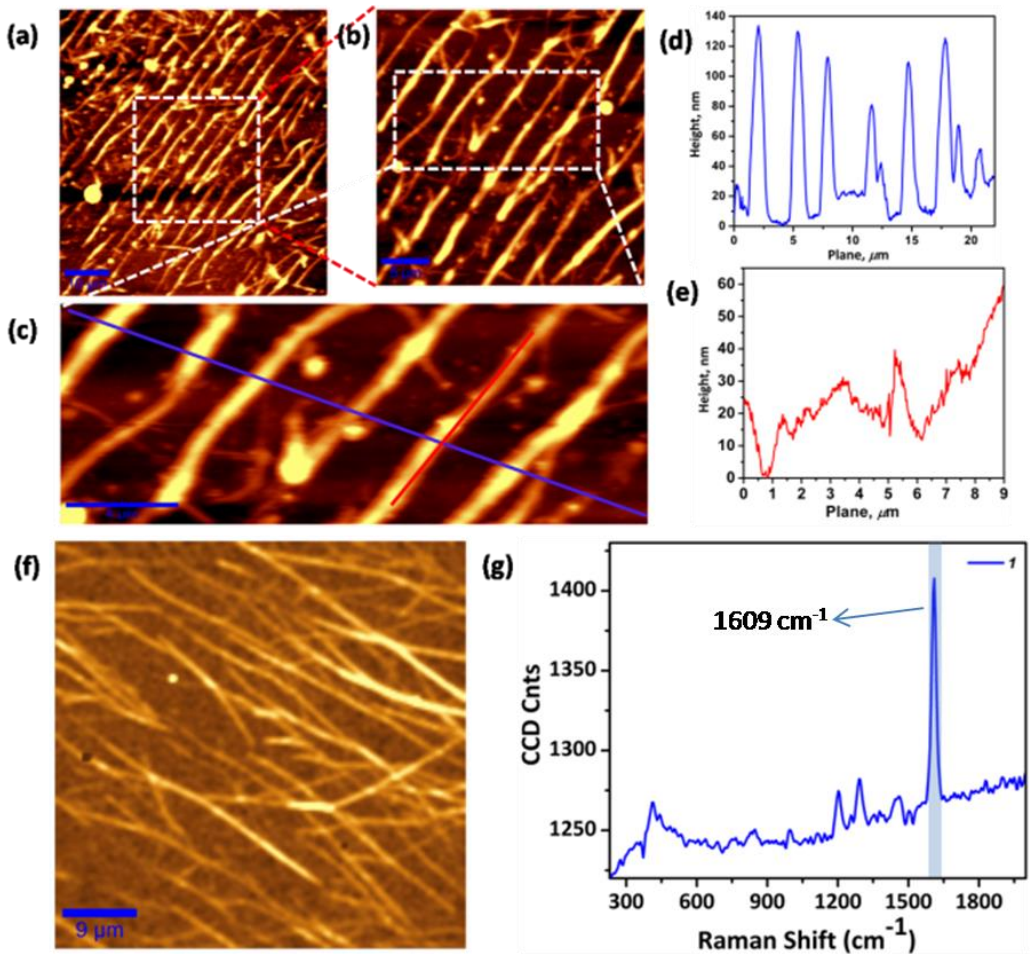

Figure 2.7*: (a) AFM image of the patterned growth of coordination polymer* ***1*** *(5o x50 μm area), (b) the magnified area shown in image (a) by dotted white square, (c) the magnified area shown in image (b) by dotted white rectangle, (d and e) topographic profile along the blue line as well as red line shown in image c. (f) Raman image of the aligned coordination polymer* ***1*** *fiber, (g) Raman spectrum from the aligned fiber.*

Anisotropic ordering of SCO coordination polymer nano-tapes at a surface is a challenging task. The arrangement of 1-D nano-tapes in an array fashion is a first step towards the fabrication of logical memory based devices based on SCO compounds. Hence we envisioned to align them in an orderly fashion by following one of the top-down soft-lithography approaches, namely lithographically controlled wetting (LCW) technique.[7] LCW involves the use of a poly(dimethylsiloxane) (PDMS) stamp. We have used PDMS stamp consists of an array of 1D rectangular stripes as discussed in 2.3.6. At first, 200μL of the saturated dichloromethane (DCM) solution of complex **1** was diluted by adding 100 μL of DCM. A 20 μL of this solution was placed on a clean glass slide and it was immediately covered by the protrusion of the PDMS stamp. After drying the solvent, the stamp was gently peeled-off from the substrate. Confocal microscopic investigation of the substrate clearly showed the formation of an array of 1-D structures. Noncontact mode AFM studies of the arrays showed that the gap between the each aligned stripes is ~2.54 μm (*Figure* 2.7*a* and *d*). The height and roughness of the stripe are ~120 nm and ~±30 nm, respectively (*Figure* 2.7*d* and *e*). The AFM profile clearly point out that the alignment of the nano-tapes happened inside the channels. Further investigation of the arrays by confocal Raman spectroscopy/imaging technique demonstrated that the stripes indeed composed of SCO Polymer **1** (*Figure* 2.7*f* and *g*).

2.4 Conclusions:

A highly soluble Fe (II) SCO coordination polymer **1** with the $T_{1/2}$ of 296 K form self-assembled isotropically distributed nano-tapes. Using LCW technique the nano-tapes were oriented into aligned 1D arrays. The presented technology is very simple, unprecedented, and promising for potential future development in the SCO-based memory storage devices.

References:

1. (a) Garcia, V.; Bibes, M. *Nature.* **2012**, *483*, 279–281. (b) Bousseksou, A.; Molnar, G.; Salmon, L.; Nicolazzi, W. *Chem. Soc. Rev.***2011**, *40*, 3313–3335. (c) Kahn, O.; Martinez, C. J. *Science* **1998**, *279*, 44. (d) Bousseksou, A.; Molnar, G.; Demont, P.; Menegotto, J. *J. Mater. Chem.***2003**, *13*, 2069. (e) Halcrow, M. A.; *Chem. Soc. Rev.***2011**, *40*, 4119–4142. (f) Halcrow, M. A.; *Coord. Chem. Rev.***2009**, *253*, 2493–2514. (g) Halcrow, M. A.; *Spin Crossover Materials: Properties and Application*; Wiley-Blackwell: Oxford, U.K., **2013**. (h) Olguín, J.; Brooker, S. *Coord. Chem. Rev.***2011**, *255*, 203–240. (i) Wagner, S.; Kisslinger, Ballmann, S.; Schramm, F.; Chandrasekar, R.; Bodenstein, T.; Fuhr, O.; Secker, D.; Fink, K.; Ruben, M.; Weber, H. B.; *Nat. Nanotechnol*. **2013**, *8*, 575.

2. (a) Cavallini, M.; Bergenti, I.; Milita, S.; Ruani, G.; Salitros, I.; Qu, Z. R.; Chandrasekar, R.; Ruben, M. *Angew. Chem.* **2008**, *47*, 8596. (b) Cavallini, M.; Bergenti, B.; Militta, S.; Kengne, J. C.; Gentili, D.;

Ruani, G.; Salitros, I.; Meded, V.; Ruben, m. *Langmuir.* **2011**, *27*, 4076−4081. (c) Basak, S.; Hui, P.; Chandrasekar, R. *Chem. Mater*. **2013**, *25*, 3408-3413.

3. Meded, V.; Bagrets, A.; Fink, K.; Chandrasekar, R.; Ruben, M.; Ever, F. *Phys. Rev. B.***2011**, *83*, 245415.
4. Basak, S.; Hui, P.; Boodida, S.; Chandrasekar, R. *J. Org. Chem.* **2012**, *77*, 3620−3626.
5. (a) Schwarz, G.; Bodenthin, y.; Tomkowicz, Z.; Haase, w.; Geue, T.; Kohlbrecher, J.; Pietsch, U.; Kurth, D. G. *J. Am. Chem. Soc.* **2011**, *133*, 547-558. (b) Bodenthin, Y.; Schwarz, G.; Tomkowicz, Z.; Geue, T.; Haase, W.; Pietsch, U.; Kurth, D. G. *J. Am. Chem. Soc.* **2009**, *131*, 2934-2941. (c) Basak, S.; Hui, P.; Chandrasekar, R. *J. Org. chem*. **2012**, *10,* 2439-2446.

6. (a) Thompson, J. R.; Archer, R. J.; Hawes, C. S.; Ferguson, A.; Wattiaux, A.; Mathoniere, C.; Clerac, R.; Kruger, P. E.; *Dalton Trans.* **2012***, 41,* 12720-12725.

7. (a) Cavallini, M.; Biscarini, F. *Nano. Lett.* **2003**, *3*, 1269-1271. (b) Cavallini, M.; Gentili, D.; Pierpaolo, G.; Francesco, V.; Biscarini, F. *Nat. Protoc.* **2012***, 7,* 1668-1676.

Chapter 3

Optical wave guiding organic nano rods coated with reversibly switchable Fe(II) spin crossover nanoparticles

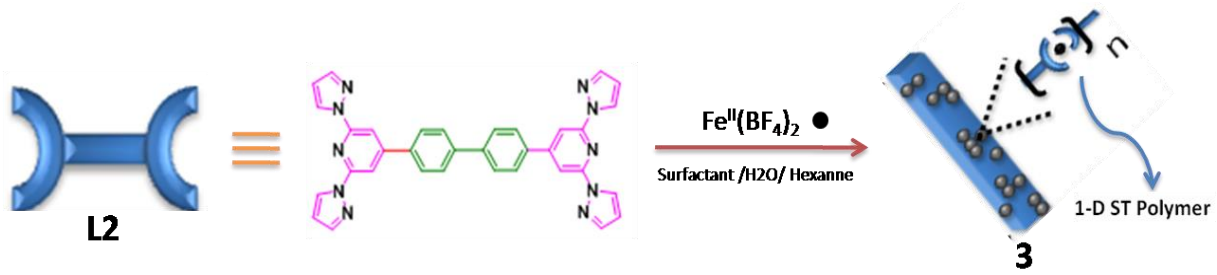

3.1 Abstract:

A dual functional nanohybrid soft structure combining photonic and magnetic properties was successfully prepared through a "bottom up" self-assembly approaches. In this method, SCO Fe(II) coordination nanoparticles and optical wave guiding organic nanorods were generated in situ and successfully integrated together in a single pot through self-assembly. The Fe(II) nanoparticles coated on organic nanorods (nanohybrids) display temperature dependent reversible SCO behavior (Paramagnetic; $\mathcal{S} = 2 \leftrightarrow$ diamagnetic; $\mathcal{S} = 0$). The nano-hybrids show efficient optical wave guiding behavior, which demonstrates the future possibility to perform remote light induced excited spin state trapping (LIESST) experiments on a single spin transition nanoparticle level. These photonic and magnetic "nanohybrids" offer promising option to externally manipulate spin state of the SCO nano particles using temperature as well as remote laser light.

This chapter has been adopted from the following publication:Basak, S.; Botcha, A. K.; Ansari, M. T.; Chandrasekar, R.*
Indian J. Mater. Science. **2013**, ID 136178.

3.2 Introduction:

Bottom-up nanofabrication of self-assembled multifunctional nanoobjects and study of their uncharted physical properties at the nanoscale level are an active and sophisticated research area of nanoscience and technology.[1–13] Particularly programming the *in situ* growth of organic and inorganic nanostructures from different molecular components and also their integration to form hybrid nanoscale objects in the same pot is a less explored area. A successful ground work in this discipline might lead to new advanced functional hybrid nanomaterials capable of performing a sensing, electronic, and photonic function.[1–13] For example integration of magnetically bistable inorganic nanoparticles (NPs) and optical wave guiding organic nanostructures could facilitate remote manipulation of the light sensitive spin states of individual NPs through guided laser light. Recently, we have reported for the first time on the passive wave guiding behavior of organic tubes and also demonstrated the remote electronic excitation of a *meso*tetratolylporphyrin nanosheet using a 20 μm long optical wave guiding organic tube.[14–16] Hence we intended to study the propensity of the 1D organic solids coated with SCO (or) spin transition NPs[17–37] (ST-NPs) to guide source laser light under laser confocal microscope setup. It was anticipated that the dielectric difference between the 1D nano-hybrid solid and the surrounding medium would guide the optical wave along the growth axis of the organic waveguide.

Among NPs, Fe(II) ST-NPs are of interest due to their switchable bistable magnetic spin states between paramagnetic high-spin state (S = 2; $t_{2g}^4\, e_g^2$) and diamagnetic low spin state (S = 0; $t_{2g}^6 e_g^0$) [17–37]. ST-NPs undergo reversible magnetic switching between low-spin (LS) and high-spin (HS) states due to the modulation of ligand field strengths depending on the temperature, light, and pressure. Till now there is no direct *in situ* method available on the integration of ST-NPs on other self-assembled organic nanoobjects. Recently our group reported an efficient solvent-assisted technique for the preparation of organic sub microtubes from a *back-to-back* coupled ditopic ligand, 4,4”-bis(2,6-di(1Hpyrazol-1-yl)pyridin-4-yl)biphenyl, **L2** in dichloromethane.[12] We found that **L2** also forms crystalline organic nanorods (ONRs) in hexane. Additionally, **L2** is also a good candidate for the syntheses of 1D ST metallo-supramolecular coordination polymers[38,39] due to its readily available two tridentate metal chelating sites on either side of the molecule. The surface of the **L2** ONR also can facilitate the interaction of Fe(II) ion and surfactant to form ST-NPs attached to the surface there by forming integrated ST nanohybrids.

To realize our idea, by following reverse micelle technique[40] we developed a single step method to fabricate ONRs from **L2**, which are coated with ST-NPs (*Scheme 1*). Herein we present our nanohybrid preparation procedure: (i) self-assembly of **L2** to form ONRs and (ii) self-assembly

of ST-NPs from molecules **L2** available on the surface of the ONRs in presence of Fe(II) salt and surfactants. We also report the electron (SEM, FESEM, and TEM), atomic force microscopy (AFM), and Raman spectroscopy images of the nanohybrids and also the variable temperature magnetic properties of bulk 1D ST coordination polymer **2** and ST-NPs coated on ONRs **3**. Finally we also present our preliminary results on the optical wave guiding tendency of the nano-hybrids.

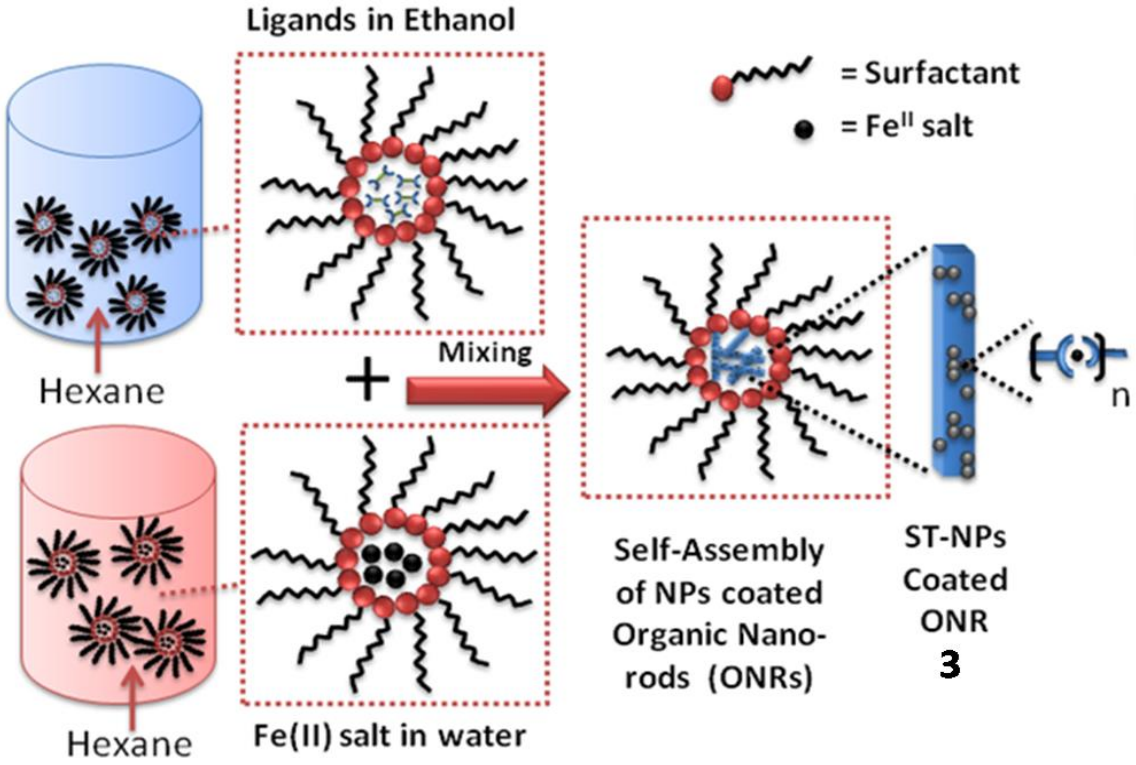

Scheme 3.1*: Schematic representation of the components used in the reverse micelle technique for the fabrication of spin transition nanoparticles (ST-NPs) coated on organic nanorods (ONRs)*

3.3 Results and Discussion:

3.3.1 Synthetic procedures of 2 and 3:

Preparation of coordination polymer is as following (**2**): 40 mg (0.069 mmol) of ligand 4,4'-bis(2,6-di(1H-pyrazol-1-yl)pyridin-4-yl)biphenyl **L2** was dissolved in a deaerated dichloromethane (30 mL). To this a deaerated methanolic solution containing 35.5 mg (0.139 mmol) of $Fe(BF_4)_2.6H_2O$ was added and stirred for 2 days under N_2 atmosphere. The solvents were evaporated from the turbid solution and the obtained yellow precipitate was collected and washed with dichloromethane and methanol and finally air-dried. Yield 53 mg; FTIR (KBr,]/cm^{-1}): 3524, 3435, 3128, 2924, 2854, 1631, 1572, 1523, 1460, 1406, 1253, 1219, 1053, 966, 819, 761. Elemental analysis (%) calculated for $C_{34}H_{24}B_2F_8FeN_{10}$: C 50.91, H 3.02, N 17.46; found C 51.41, H 2.95, N 17.25.

Preparation of ST nanoparticles coated nanorod is as follows (**3**): Fe $(BF_4)_2.6H_2O$ (14.6mg, 0.664mmol) was dissolved in water (2 mL), and added to a mixture of sodium dioctylsulphosuccinate (0.256 g) in 10mL of hexane. After a few minutes of stirring, behenic acid (39.4mg, 1.328) was added to this suspension. 4,4'-Bis(2,6-di(1H-pyrazol-1-yl)pyridin-4-yl)biphenyl (100mg, 0.174mmol) was suspended to ethanol (10 mL), added to the above mixture, and vigorously stirred for 36 h. Afterwards, the mixture was evaporated to get a sticky solid, the excess surfactants were removed by centrifuging with ethanol for several times. The powder obtained was finally dried under vacuum to afford a yellow powder of **3** (50 mg). FTIR (KBr,]/cm^{-1}): 3148, 2918, 2849, 1707, 1612, 1572, 1539, 1510,1462, 1394, 1261, 1207, 1035, 952, 935, 914, 871, 823, 787, 767, 628, 605, 486. Raman (cm^{-1}): 1604 (C=C), 1444, 1378, 1364, 1289, 1256, 1223, 1125, 1021, 996.

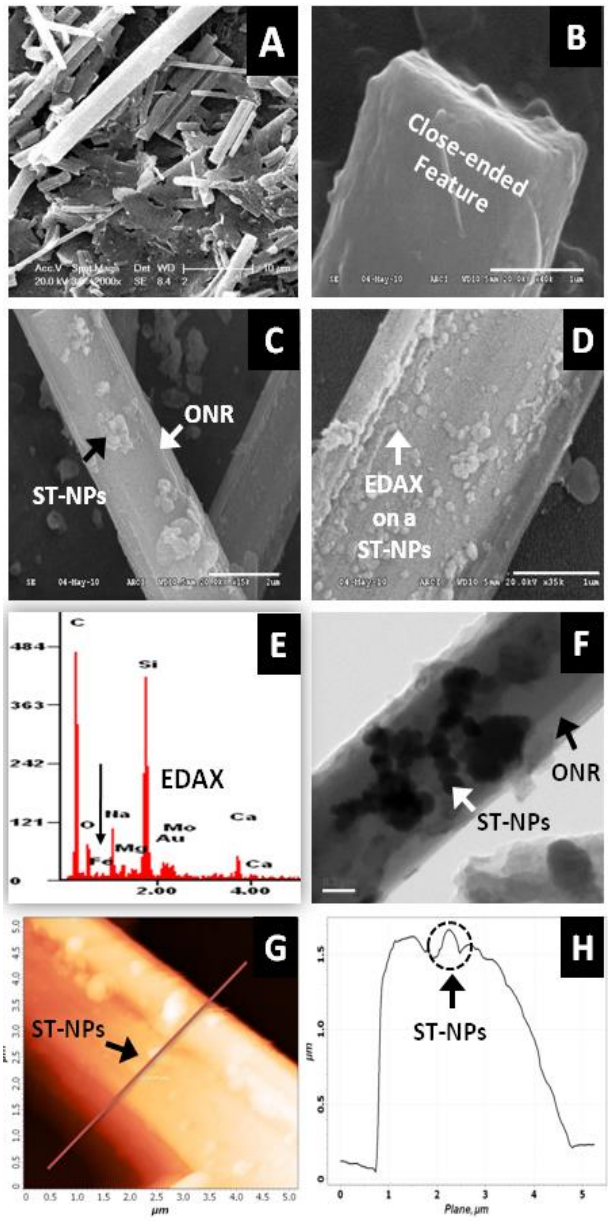

Figure 3.1: *SEM (a), FESEM (b-e), TEM (f) and AFM (g-h) micrographs and data of ONRs coated with coordination ST-NPs 2. a) a bunch of ONRs coated with ST-NPs; b) close-ended feature of a ONR; c and d) a nano-rod clearly shows the presence of spherical ST-NP aggregates on it; e) energy dispersive X-ray analysis (EDAX) data collected on ST-NPs coated on ONR; f) the dark (ST-NPs) and grey colour (ONR) contrast clearly distinguish the NPs from the ONRs; g) AFM image of a single ONR coated with ST-NPs. h) Cross-section profile along the red line in (g). Scale bars are: A: 10 µm; B, C: 2 µm; D: 1 µm; and F: 200 nm.*

3.3.2 Synthesis and characterization of ONRs coated with ST-NPs:

In the bulk state treatment of **L2** with $Fe^{II}(BF_4)_2.6H_2O$ (1 : 1 stoichiometry) in acetonitrile immediately formed an insoluble yellow precipitate, which indicated the formation of a 1D linear coordination polymer $[Fe^{II}(\mathbf{L2})(BF_4)_2]_n$ (**2**). We have employed an *in situ* reverse micelle technique to grow self-assembled nano-hybrids, that is, ONRs

coated with ST-NPs. Firstly dispersion of an ethanol solution of **L2** in hexane followed by treatment with sodium dioctylsulfosuccinate surfactant has formed micelle containing **L2** stabilized by the surfactant. Secondly, dispersion of an aqueous solution of Fe(II) salt in hexane followed by the treatment of surfactant produced a Fe(II) carrying micelle stabilized by the surfactants. Mixing followed by stirring of the two solutions containing micelle carrying **L2** and Fe(II) salt formed a yellow precipitate of ST-NPs coated ONRs **3**. Filtration of the resultant precipitate followed by drying gave a light yellow powder of **3**. The electron microscopy (SEM, FESEM, and TEM) images of **2** clearly exhibited the formation of ST-NPs on ONRs. The SEM images of **3** showed that the ONRs of different lengths varying from 5–30 μm lengths and widths in the range of ca. 1–4 μm (*Figure* 3.*1a*). FESEM measurements clearly showed the growth of aggregates of spherical NPs on the surface of the ONRs (*Figures 3.1b-d*). Furthermore the energy dispersive X-ray analysis (EDAX) measurement performed on NPs coated on ONRs clearly indicated the presence of iron ions in the spherical NPs (*Figure 3.1e*).

Additionally AFM measurements confirmed the hybrid assembly of ST-NPs on ONRs (*Figures 3.1g, h*). A typical width × height range profile of selected ONRs is ca. 1–4 × 0.4–1.5 μm. Direct visualization of ST-NPs (black contrast) on the surface of the ONRs (grey contrast) was achieved by TEM measurements (*Figure 3.1f*). The NPs are spherical in shape and the sizes were in the range of ca.70–200 nm. The spherical particles were aggregated together on the surface of the ONRs.

3.3.3 Confocal micro-Raman spectroscopy/waveguiding studies:

The confocal Raman microspectroscopic data (with 488nm Ar^+ laser; back scattering mode) confirmed the presence of ST-NPs on the surface of the ONR by exhibiting characteristic Raman

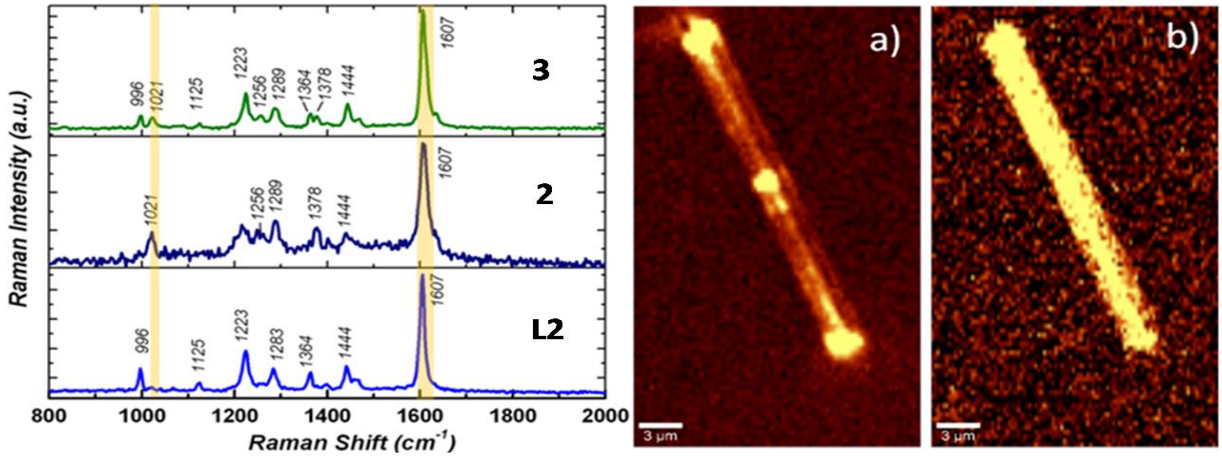

Figure 3.2*: Comparative confocal Raman micro spectroscopic data collected from* ***L2****,* ***2*** *and the Fe(II) coordination nanoparticles coated organic nano-rods* ***3****. (a) Raman image of the 1021 cm^{-1} region. (b) Raman image of the region between 1580 and 1631 cm^{-1}.*

shifts corresponding to bulk **L2** and ST-NPs**2** (*Figure 3.2*). The Raman modes of coordination polymer **2** were observed in the ONR-NPs. To identify the NPs, the peak at 1021 cm^{-1} was picked-up and used for mapping (*Figure 3.2a*). Interestingly the signal intensity of the 1021 cm^{-1}peak was quite high at the rod ends. Raman imaging of a common peak (1607 cm^{-1}) corresponds to C=C showed nearly equal intensity from rods. The confocal fluorescence microscopy studies of the nanorods coated with ST-NPs **3** displayed a blue emission at 443 nm demonstrating the fluorescence property of the nanorods and also possibility to utilize these rods as active waveguides (*Figure 3.3*).

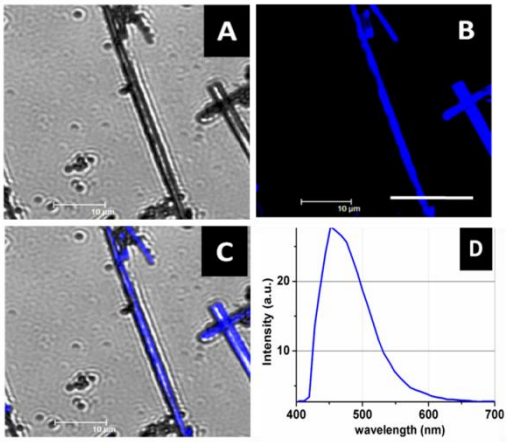

Figure 3.3*: Confocal fluorescence microscopy data of nanorods coated with ST-NPs **3**. (A) Before excitation ((B); (C)) after excitation by Ar-ion UV laser. (D) Emission spectrum of rods shown in (B) and(C).*

3.3.4 Spin crossover studies:

The temperature dependent magnetic measurements data of **2** and **3** in the range of **3**75 ↔5K at 1000 Oe DC magnetic field are shown in *Figure 3.4*. For **2** the product of magnetic susceptibility and temperature χT versus Tcurve indicated the presence of a reversible ST behavior. The value of χT at 375 K (ca. 3.5 emu. K/mol) indicated the HS state of **2**. Upon cooling down to 293 K the χTvalue further decreased to 2.85 emu. K/mol. This demonstrated the presence of HS and LS fractions at room temperature. Further cooling showed a steep decrease of the χT value which reached a minimum value of ca. 0.5 emu. K/mol at 5 K, specifying the completion of the ST event. The χTcurve showed a similar trend even in the heating mode performed up to 375 K. The ST temperature of **2** is ca. 201 K. Since the process of ST is very sensitive to environmental changes, to

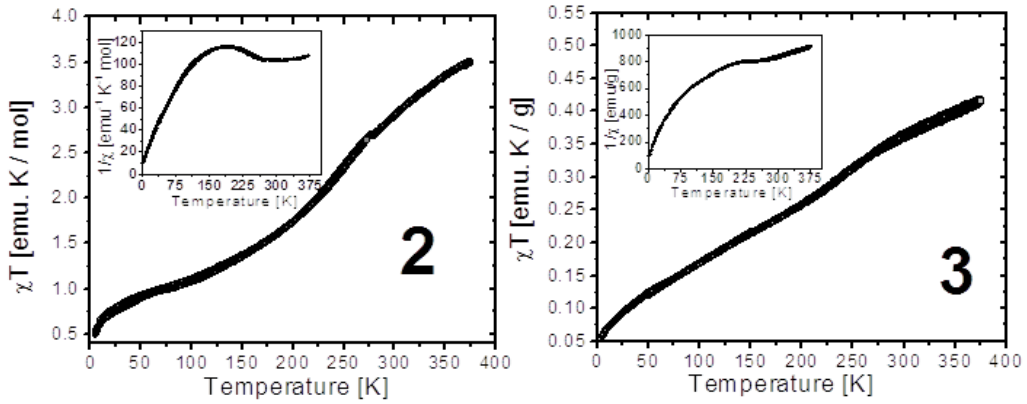

Figure 3.4*: χT = f(T) plots for bulk sample of **2** (left) and the Fe (II) coordination nanoparticles coated ONRs **3**(right). Inset figures show the 1/χ versus T plots.*

explore the ST tendency of the NPs coated on ONRs, the variable temperature magnetic properties of sample **3** were also investigated *(Figure 3.4 right)*. Interestingly the reversible ST property was retained for **3** but with a change in the ST temperature (ca.160 K) and its propensity compared to **2**. The shifting of the ST to lower temperature side is perhaps due to the decrease of the long-range cooperatives in the NP state. Additionally, the origin of smooth ST compared to **2** is probably due to the presence of ST-NPs of various particle size ranges.[25]

3.3.5 Waveguiding properties ONRs coated by ST-NPs (3)

For the passive optical wave guiding studies, a visible light laser (488 nm; Ar+) was employed to circumvent the electronic absorption of a laser light by the molecular building blocks of the rods (*Figure 3.5a*). The laser beam was coupled to the ONR kept on a thin glass substrate through a 50X objective (NA = 0.90). Orthogonal illumination of a laser beam at any one of the ends of a rod (*optical coupling point*) showed propagation of guided laser light to the opposite end of the rod (Bright field images; *Figures 3.5b and c*) while irradiation of laser at the center of the rod showed guided light propagation to both ends of the rod (*Figure 3.5d*). The corresponding dark field images taken with a 488 long pass edge filter (LPEF) are shown in *Figures 3.5e–5g*. Fe(II) STNPs are

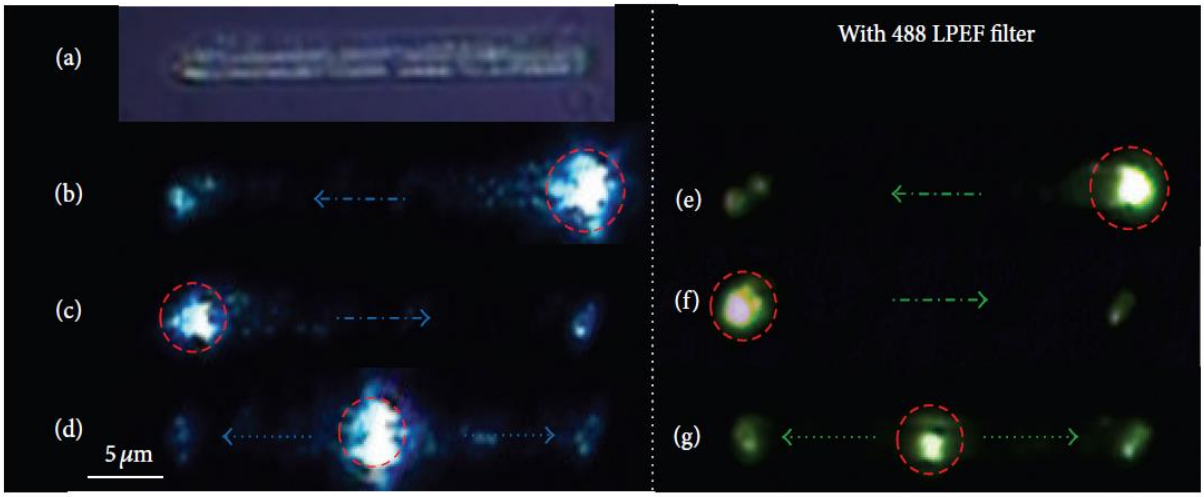

Figure 3.5*: Confocal micrographs of a wave guiding ONR under 488nm Ar^+ laser illumination. ((a)–(d)) without 488nm LPEF; ((e)–(g)) with 488 nm LPEF filter. Red circles show laser illumination point and blue/green arrows show the propagation direction.*

known to display light induced electron spin state trapping (LIESST) effect[41] that is, metastable high-spin state (S = 2) upon illumination with laser light at cryogenic temperature. In all of the reported literature works these LIESST experiments were performed on a bulk ST samples at very low temperature.[41–43] Our preliminary experimental results demonstrate that the remote LIESST studies can be done on single ST-NP level using a waveguiding organic nanorod coated with ST-NPs.

3.4 Conclusions:

The presented results clearly demonstrate a successful *in situ* preparation of organic and inorganic nanostructures such as ST-NPs and ONRs in a single pot to create nanohybrids. The optical wave guiding nature of the ONRs can be exploited to control the spin state of the ST-NPs using guided laser light. This is an attempt towards the "bottom-up" fabrication of externally switchable "nanohybrids'' by combining optical and magnetic properties.

References:

1. Mann, S. *Nat. Mater*. **2009**, *8*, 781-792.
2. Mirkin, C. A.; Niemeyer, C. M.; *Nanobiotechnology II*, Wiley- VCH, Weinheim, Germany, **2007**.
3. Mirkin, C. A.; Letsinger, R. L,; Mucic, R. C.; Storhoff, J. J. *Nature*. **1996**, *382*, 607-609.
4. Katz. E.; Willner, I. *Angew. Chem.* **2004***, 43,* 6042- 6108.
5. Nakanishi, T. *Chem. Commun.* **2010**, *46*, 3425-3436.
6. Van Bommel, K. J. C.; Friggeri, A.; Shinkai, S. *Angew. Chem*. **2003**, *42*, 980-999*.*
7. Li, M.; Viravaidya, C.; Mann, S. *Small*. **2007**, *3*, 1477-1481.
8. Okuda, M.; Kobayashi, Y.; Suzuki, K.; Sonoda*, K.;* Kondoh, *T.;* Wagawa, *A.;* Kondo*, A.;* Yoshimura, H*. Nano Lett.* **2005**, *5*, 991-993.
9. Meadows, P. J.; Dujardin, E.; Hall, S. R.; Mann, S. *Chem. Commun*. **2005**, *29*, 3688-3690.
10. Patil, A. J.; Li, M.; Dujardin, E.; Mann, S. *Nano Lett*. **2007**, *7*, 2660-2665.
11. Sofos, M.; Goldberger, J.; Stone, D. A.; Allen, J. E.; Ma, Q.; Herman, D. J.; Tsai, W. W.;Lauhon, L. J.; Stupp, S. I. *Nature Mater*. **2009**, *8*, 68-75.
12. Chandrasekhar, N.; Chandrasekar, R. *Chem. Commun*. **2010**, *46*, 2915-2917.
13. Basak, S.; Chandrasekar, R. *Adv. Funct. Mater*.**2011**, *21*, 667-673.
14. Chandrasekhar, N.; Mohiddon, M. A.; Chandrasekar, R. *Adv. Opt. Mater*. **2013**, *1*, 305-311.
15. Hui, P.; Chandrasekar, R. *Adv. Mater*. **2013**, *25*, 2963-2967.
16. Chandrasekhar, N.; Chandrasekar, R. *Angew. Chem.* **2012***, 51,* 3556-3561*.*
17. Gutlich, P.; Goodwin, H. A.; *Spin Crossover in Transition Metal Compounds I*, *Topics in Current Chemistry*, Springer, Berlin, Germany, **2004**.
18. Spiering, H. *Spin Crossover in Transition Metal Compounds III*, *Topics in Current Chemistry*, Springer, Berlin, Germany, **2004.**
19. Konig, E. *Prog. Inorg. Chem*. **1987**, *35*, 527.
20. Gaspar, A. B.; Ksenofontov, V.; Seredyuk, M.; Gutlich, P. *Coord. Chem. Rev*. **2005**, *249*, 2661-2676.
21. Gutlich, P.; Garcia, Y.; Woike, T. *Coord. Chem. Rev*. **2001**, *219-221*, 839-879.
22. Halcrow, M, A. *Coord. Chem. Rev*. **2009**, *253*, 2493-2514.

23. Forestier, T.; Mornet, S.; Daro. N.; Nishihara, T.; Mouri, S.; Tanaka, K.;Fouche, O.; Freyszc, E.;Letard, J. *Chem. Commun*. **2008**, *36*, 4327-4329.
24. Coronado, E.; Gallan-Mascarros, J. R.; Monrabal-Capilla, M.; Garca-Martnez, J.; Pardo-Ibanez, P. *Adv. Mater*. **2007**, *19*, 1359-1361.
25. Volatron, F.; Catala, L.; Riviere, E.; Gloter, A.; Stephan, O.; Mallah, T. *Inorg. Chem*. **2008**, *47*, 6584-6586.
26. Boldog, I.; Gaspar, A. B.; Martinez, V.; Pardo-ibaiez, P.; ksenofontov, V.; Bhattacharjee, A.; Gutlich, P.; Real, J. A. *Angew. Chem.***2008***, 47,* 6433-6437*.*
27. Larionova, J.; Salmon, L.; Guari, Y.; Tokarev, A.; Molvinger, K.; Molnar, G.; Bousseksou, A. *Angew. Chem.* **2008***, 47,* 8236-8240.
28. Letard, J. *J. Mater. Chem*. **2006**, *16*, 2550-2559.
29. Chandrasekar, R.; Schramm, F.; Fuhr, O.; Ruben, M. *Eur. J. Inorg. Chem*. **2008**, *17*,2649-2653.
30. Cavallini, M.; Bergenti, I.; Milita. S.; Ruani, G.; Salitros, I.; Qu, Z.; Chandrasekar, R.; Ruben, M. *Angew. Chem.* **2008***, 47,* 8596-8600*.*
31. Rajadurai , C.; Schramm, F.; Brink S.; Fuhr, O.; Ghafari, M.; Kruk, R.; Ruben, M. *Inorg. Chem*. **2006**, *45*, 10019-10021.
32. Rajadurai, C.; Fuhr, O.; Kruk, R.; Ghafari, M.; Hahn, H.; Ruben, M. *Chem. Commun*. **2007**, *25*, 2636-2638.
33. Rajadurai, C.; Qu, Z.; Fuhr, O.; Gopalan, B.; Kruk, R.; Ghafari, M.; Ruben, M. *Dalton. Trans*. **2007**, *32*, 3531-3537.
34. Chandrasekhar, N.; Chandrasekar, R. *Dalton. Trans*. **2010**, *39*, 9872-9878.
35. Basak, S.; Hui, P.; Chandrasekar, R. *Chem. Mater*. **2013**, *25*, 3408-3413.
36. Salitros, I.; Pavlik, J.; Boca, R.; Fuhr, O.; Rajadurai, C.; Ruben, M. *Cry. Eng. Commun*.**2010**, *12*, 2361-2368.
37. Gonzalez-Prieto, R.; Fleury, B.; Schramm, F.; Zoppellaro, G.; Chandrasekar, R.; Fuhr, O.; Lebedkin, S.; Kappes, M.; Ruben, M. *Dalton. Trans*. **2011**, *40*, 7564-7570.
38. Chandrasekhar, N.; Chandrasekar, R. *J. Org. Chem*. **2010**, *75*, 4852-4855.
39. Basak, S.; Hui, P.; Boodida, S.; Chandrasekar, R. *J. Org. Chem*. **2012**, 77, 3620-3626.
40. Vaucher, S.; Li, M.; Mann, S. *Angew. Chem.* **2000***, 39,* 1793-1796*.*
41. Chakraborty, Boillot, M. L.; Tissot, A.; Hauser, A. *Angew.Chem.* **2013***, 52,* 1*.*
42. Decurtins, S.; Gutlich, P.; Kohler, C. P.; Spiering, H. *Chem. Commun*. **1985**, *7*, 430-432.
43. Letard, J. F.; Guionneau, P.; Rabardel, L.; howard, J. A. K.; Goeta, A. E.; Chasseau, D.; Kahn, O. *Inorg. Chem*. **1998**, *37*, 4432-4441.

Chapter 4

Synthesis of gold nanoparticles stabilized by novel thiol functionalized Fe(II)complex to study spin crossover effect through propagating surface plasmon

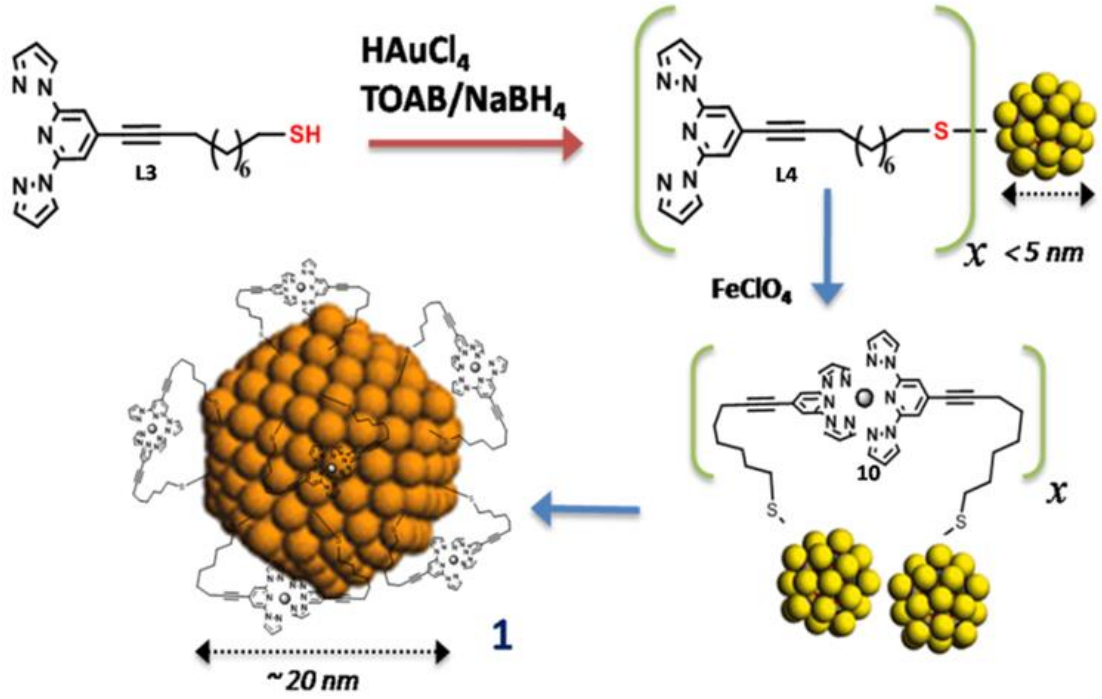

4.1 Abstract:

*This chapter demonstrates the synthesis of gold nanoparticles (Au NPs) stabilized by thiol functionalized BPP ligands. Au-NPs of different shapes show shape dependent surface plasmon properties. This work presents an innovative synthetic approach to achieve Au NPs of different shapes such as spherical-, cubic- and triangle stabilized by ligand **L4** and [Fe(**L4**)](ClO$_4$)$_2$ complex. The UV-Visible, powder XRD, and transmission electron microscope (TEM) studies were employed to characterize the thiol functionalized gold nanoparticles. Attempts also were made to prepare 1-D arrays via lithography to remotely detect the spin crossover (SCO) effect through propagating surface plasmon.*

4.2 Introduction:

Nanomaterials composed of metallic and semiconductors show interesting size and shape dependent properties such as magnetic, electrical, optical, photonic and catalytic properties etc.[1-3] Au NPs have attracted various fields of science and technology such as chemistry, physics, biology, material science and engineering due to its their stability, nontoxic nature and versatility of surface functionalities.[4] Surface plasmon resonance (SPR)[5] occurs when the natural frequency of oscillating electrons of nanoparticles matches with the frequency of electromagnetic radiation. SPR is responsible for the various colours observed in metal nanoparticles. Many functional organic molecules carrying stabilizing groups were synthesized to protect Au NPs from agglomeration, for instance, different kinds of organic phase transfer reagents, carboxylates, silaxanes, disulphides and organic thiols.[6]

As discussed earlier BPP unit has the advantage of displaying spin crossover (SCO) effect upon coordinating with Fe(II) metal ion[9] with respect to external stimuli such as light irradiation (LIESST effect), temperature, pressure, and magnetic field.[10] Particularly there has been a growing interest in attaining SCO complexes due to their technological applications in molecular devices and MRI contrast agents.[11] Till now no reports available on the investigation of SCO effect through the generation of propagating surface plasmons under light irradiation. Hence in this work, an attempt has been made to fabricate rectangle microstripes composed of Fe(II) complex linked to Au NPs (**10**) via LCW technique (*Scheme 4.1*). In order to prepare SCO unit attached Au-NPs (**10**), a thiol decorated BPP ligand, 10-(2,6-di(1H-pyrazol-1-yl)pyridin-4-yl)dec-9-yne-1-thiol (**L3**) was synthesized as capping agent. According to Pearson's concept of hard and soft acid base (HSAB),[7] hard acid tend to coordinate with hard base whereas soft acid tend to bind with soft base. Since Au atom acts as soft acid and sulphur atom behaves as soft base, the capping agent it was expected that **L3** might bind on Au NPs via thiol functional group. Even, preparation of self-assembled monolayers (SAMs)[8] of organic thiols can be obtained on the surface of Au NPs by using several methods. The target molecule **L3** consists of two components: (i) thiol (-SH) group to bind with Au NPs and (ii) BPP units for coordination with Fe(II) to form SCO complex. In order to characterize **L3** and thiol functionalized Au NPs (**L4,10**), ^{1}HNMR, UV-visible spectroscopy, thermo gravimetric analysis (TGA), powder XRD and transmission electron microscope (TEM) techniques were employed. Fabrication of micro stripes composed of complex **10** with the height and width in the range of ~150-200 nm and ~2 μm, respectively was achieved for studying SCO effect through propagating plasmons. Atomic force spectroscopy (AFM), FESEM and Raman spectroscopy were used to analyze the morphology of the micro stripes.

4.3 Results and Discussion:

4.3.1 Synthetic scheme:

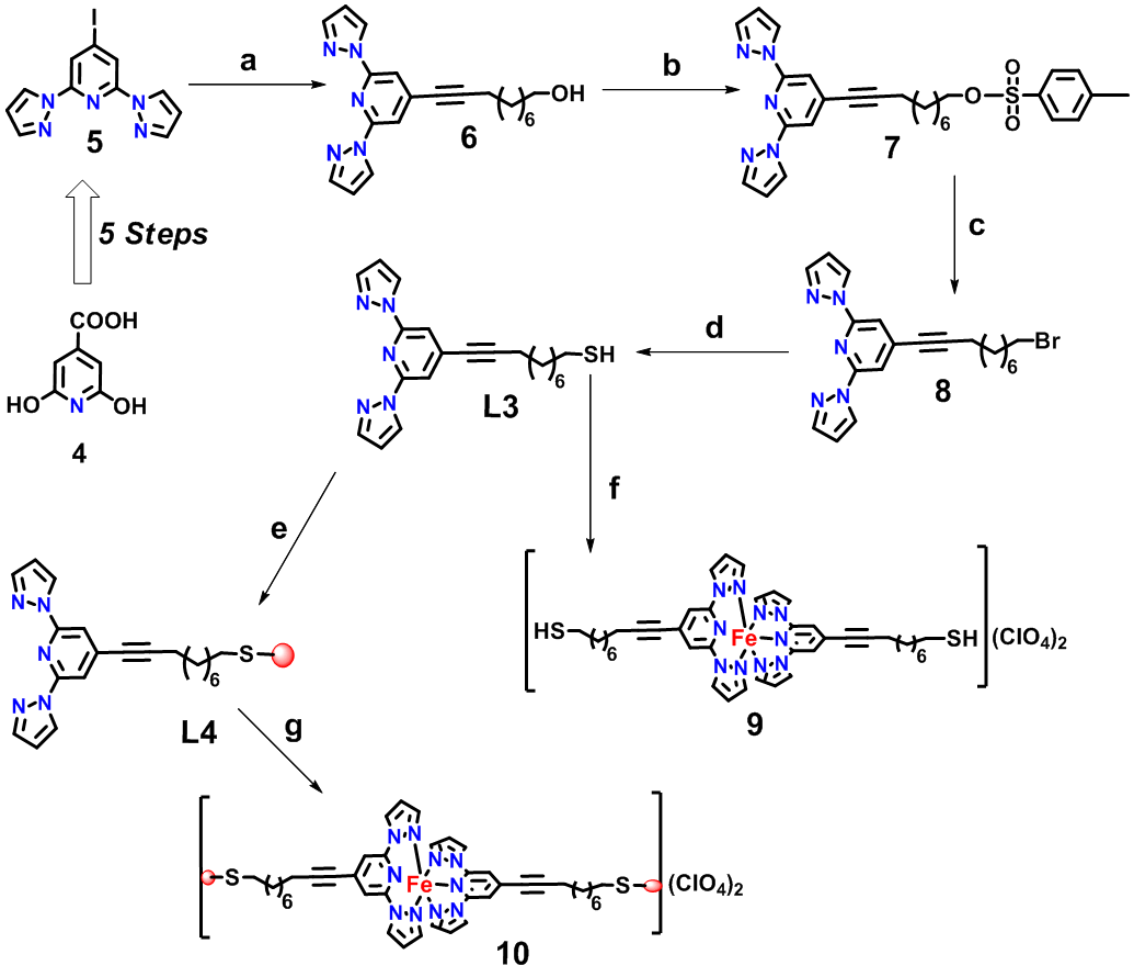

Scheme 4.1. *Reagents and conditions: (a) 9-dec-yn-1-ol, CuI, PPh_3, $Pd(PPh_3)_2Cl_2$, NEt_3, 1,4 Dioxane, 180 ℃, 12h. (b) Tosylchloride, DCM, NEt_3, RT, 4 h. (c) LiBr, Acetone, RT, 2h (d) Thiourea, NaOH, EtOH, Acetone, 80 ℃, 26 h. (e) $HAuCl_4$. $3H_2O$, TOAB, $NaBH_4$, H_2O, DCM, RT, 20 min. (f) $Fe(ClO_4).H_2O$, CH_3CN, 60 ℃, 1h (g) $Fe(ClO_4)_2{\cdot}H_2O$, CH_3CN, DCM, RT, 15 min.*

4.3.2 Synthesis:

A novel synthetic scheme was developed to prepare ligand **L3** and its Fe(II) complex **9** from the low cost starting material citrazinic acid. Conversion of citrazinic acid into 2,6-dichloroisonitinicacidmethyl ester and its subsequent conversion into **5** was carried out as per the reported procedure.[12] Attachment of decyne-1-ol to the **5** was successfully carried out under Sonogashira cross-coupling reaction conditions to achieve **6** in 90% yield. Compound **6** was tosylated by using tosylchloride in presence of base triethylamine to acquire **7** in 82% of yield, which was further transformed into **6** (73% yield) by treating with lithium bromide in acetone

solvent at room temperature. Furthermore, final conversion of the bromo derivative **8** into a thiol functional ligand **L3** was carried out in presence of thiourea and sodium hydroxide in acetone/ethanol (1:1) solution at 80°C in 65% yield. Thiol capped Au NPs (**L4**) was synthesized upon the treatment of **L3** with gold chloride in presence surfactant tetraoctylammonium bromide (TOAB) and $NaBH_4$. Pure thiol complex **9** was prepared by treating two moles of ligand **L3** with one mole of $Fe(ClO_4)_2.H_2O$ in acetonitrile in 92% yield. Finally, molecule **10**wasmade by adding few drops of methonolic solution of $Fe(ClO_4)_2.H_2O$ to the solution of **L4** in 8:2 mixture of DCM and methanol mixture.

4.3.3 Brust-Schiffrin two phase method in attaining thiol Au NPs:

Thiol capped Au NPs can be prepared in two phases according to Brust-Schiffrin's method[13] in presence of phase transfer reagent. In the first phase, aqueous solution of $HAuCl_3.3H_2O$ was transferred into DCM solvent in presence of phase transfer reagent tetraoctylammonium bromide (TOAB), which makes contact between aqueous layer and organic layer and forms ion pair complex in DCM. In the second phase, ion pair complex was transferred into solution of **L3** in DCM followed by the slow addition of aqueous solution of $NaBH_4$ as reducing agent and it was allowed stir at RT about 15 min. Consequently, the formation of deep brown colored thiol stabilized Au NPs was observed in the organic layer, DCM. Solvent extraction in water and methanol washing of crude material had led to achieve pure thiol capped Au NPs. BH_4^- is source of electrons to convert Au(III) into Au(0) in attaining thiol stabilized Au NPs. Since sulphur atom of thiol functional group acts as Lewis base, sulphur can make stable bond with Lewis acid like Au. The oxidation state of Au has been found to be zero when it was capped by the thiol ligands.

4.3.4 ^{1}H-NMR spectroscopy studies:

^{1}H NMR spectroscopy is able to identify chemical environment of protons and paramagnetic species in a given sample,[14] hence this technique was employed to study the effect of S-Au coordination on the chemical shift values of BPP. In *Figure 4.1*, the comparative ^{1}H NMR spectra of both compounds (**L3** and **L4**) shows significant changes in resonance peak positions together with line broadening. In the aromatic region, peaks of BPP in **L4** has been shifted towards up field as compared with those in **L3** with peak broading.[15a] Moreover, in case of **L3**, the protons of $-CH_2SH$, alkyne attached $-CH_2$ and $-SH$[15b] had been found at 2.69, 2.4 and 1.65 ppm, respectively after making bond between Au and sulphur in **L4**, all these peaks were disappeared and merged between 2.3 and 1 ppm with remarkable shift towards up field. All the peaks in the aliphatic region were also

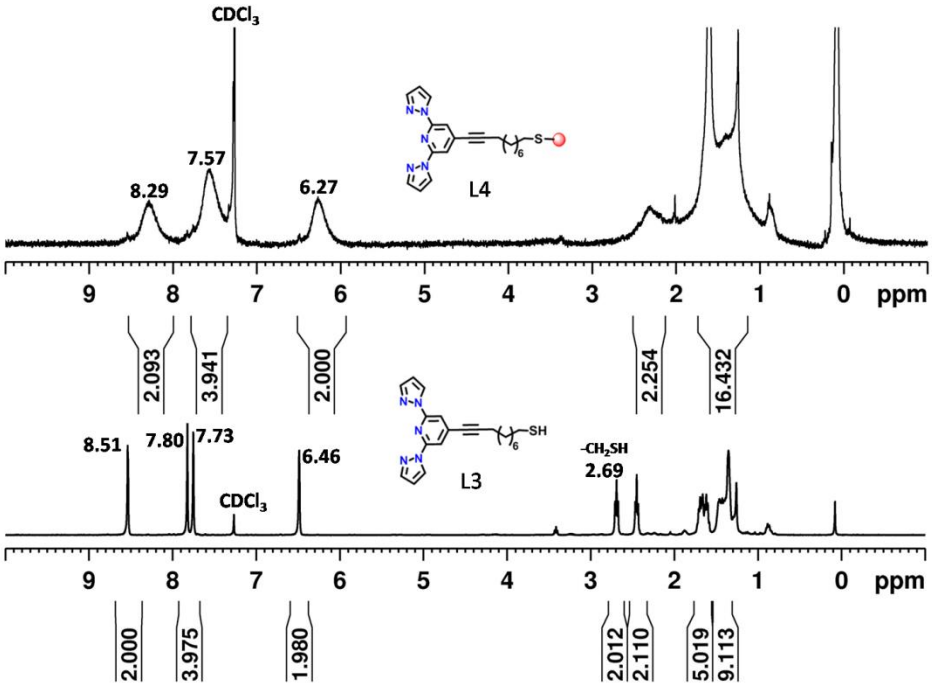

Figure 4.1**: Comparative [1]H NMR spectra of **L3** and **L4

broadened due to paramagnetic nature of Au NPs. Therefore, change in the chemical shift values and broadening of spectral lines in **L4** over **L3** indicates formation of **L4**.

4.3.5 UV-Visible spectroscopic studies for of L4 and 10:

UV-Visible spectroscopy studies of the Au NPs have exhibited SPR band under irradiation of UV-Visible electromagnetic radiation (*Figure 4.2*).[16] Generally Au NPs SPR region starts from ~520 nm and extend till near IR region depending on size and shape of Au NPs. Absorption spectra of **L3**, **L4** and **10** are shown in *Figure 4.2*, in which two bands observed at 270 nm and 310-350 nm due to $\pi \rightarrow \pi^*$ electronic transitions of the BPP. Interestingly, two broad SPR bands were also evolved in the region of ~520 nm and ~560nm corresponding to thiol functionalized Au-NPs **L4** and **10**, respectively along with absorption bands

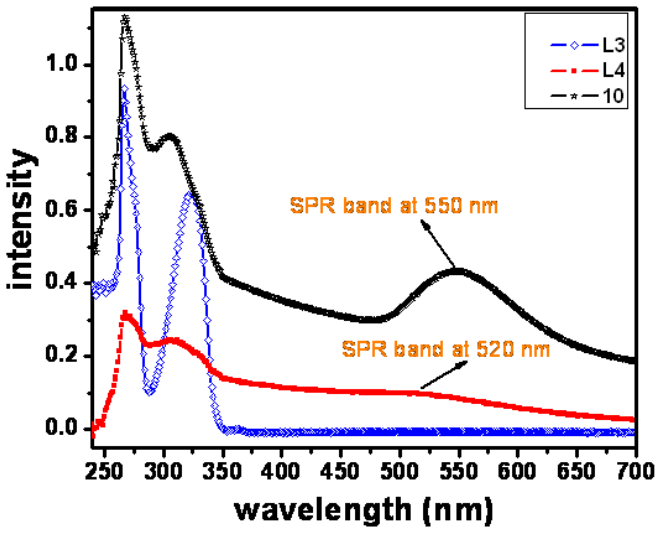

Figure 4.2**: Optical absorption spectra of **L3, L4** and **10.

of BPP. Moreover, there were remarkable blue shifts in the absorption bands of bpp towards lower wavelength in **L4** and **10** than those bands in thiol ligand **L3**. All these observations hint that Au NPs were probably capped by thiol ligand **L3**.

4.3.6 Determination of composition of L4 by TGA:

To estimate the composition of **L4** thermo gravimetric analysis (TGA) was performed (*Figure 4.3*). In the TGA data the decomposition of thiol ligand **L3** started from 200 °C and ended at ~460°C with a ~94 % of weight loss. In case of **L4**, the % of weight loss was found to be ~35% which corresponds to organic species of the compound **L4** and the remaining 65% can be attributed to Au NPs. Based on this measurement, it has been found that compound **L4** is composed of ~1:2 ratio of thiol capping unit (**L3**) and Au NPs, which matching with the stoichiometric ratios of the reactants used in the preparation of **L4**.

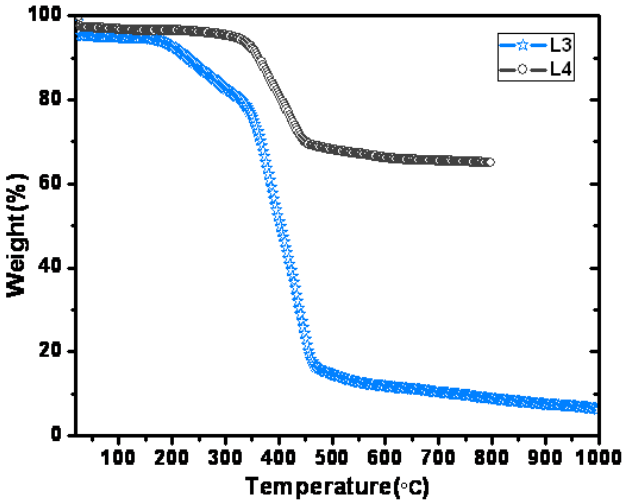

***Figure 4.3**: TGA graphs of **L3** and **L4**.*

4.3.7 TEM studies of thiol capped Au NPs (L4) and its Fe(II) complex (10):

TEM technique was employed to characterize the size and shape of Au NPs capped by **L3** (**L4**) and its Fe(II) complex (**10**). For the sample preparation a dilute solution of thiol capped Au NPs (**L4**) was dispersed in DCM and one drop of the resultant solution was drop casted on a copper grid coated with carbon film. Further, from the sample grid the solvent was allowed to evaporate to obtain stable NPs. TEM micrographs of **L4** revealed the presence nearly spherical morphology of Au NPs with different size distribution ranging from ~2.3 nm to~7 nm (*Figure 4.4a-c*). The energy dispersive X-ray spectrum (EDAX) of proved that the NPs are indeed composed of Au. Histogram of spherical Au NPs depicted in inset of *Figure 4.4b* showed the average size of Au NPs is ~4 nm. Furthermore, in high resolution transmission electron microscope (HRTEM) of spherical Au NPs (*Figure 4.4c*) showed fringe pattern which are inter planar distance of atoms stacked together (around 2.3 Å). It's difficult to say if the atoms are the light spots, or the dark spots, as this changes as a function of illumination (*Figure 4.4c right inset*). Moreover, the grain boundaries were also noticed clearly between different set of planes of Au NPs and the grain boundaries of a single NP is indicated by white arrows (*Figure 4.4c left inset*). The grid carbon support also can be seen as a back

ground noise. The selected area electron diffraction (SAED) pattern (*Figure 4.4d*) further showed the polycrystalline nature Au NPs.

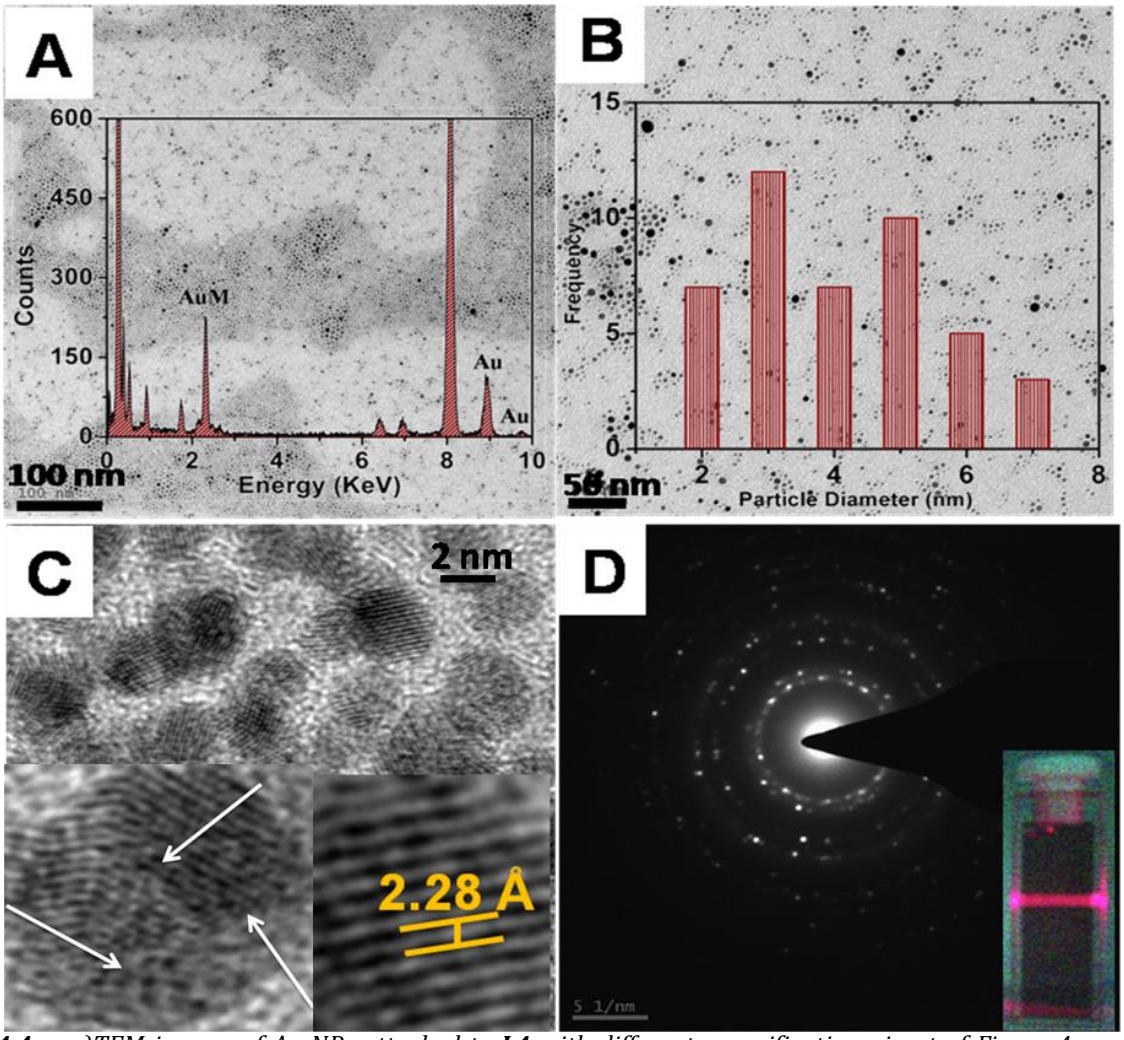

Figure 4.4: *a-c)TEM images of Au NPs attached to* ***L4*** *with different magnifications, inset of Figure 4a and 4b show the EDAX and the histogram of spherical Au NPs of different sizes, c) HRTEM image of spherical Au NPs insets show the grain boundaries and lattice spacing, d) SAED pattern of Au NPs, the inset shows the Tyndall effect.*

Interestingly in case of **10**, mixture of Au NPs such as spherical, cubic and triangular shape particles were observed during the TEM studies (*Figure 4.5a-c*). Comparatively, the size of Au NPs capped by **10** was bigger than those of **L4.** This size increase is probably occurred due to aggregation of spherical NPs of **L4** during the metal complex reaction in presence $Fe(ClO_4).H_2O$. The inter planar distance of irregular triangle and cubic Au NPs is in the range of 2.3 Å. The EDAX spectrum (*inset of Figure 4.5d*) supports the existence of Au and Fe(II) as part of thiol functionalized iron complex **10**. Moreover, the polycrystalline feature of Au NPs of **10** was also supported by SAED pattern (*Figure 4.5d*). Au NPs of **L4** and **10** were in brilliant deep brown and purple colors,

respectively, in addition to that, the colloidal solution of **10** also showed Tyndall effect under the irradiation of 633 nm laser (*see inset of Figure 4.4d and 4.5d*).

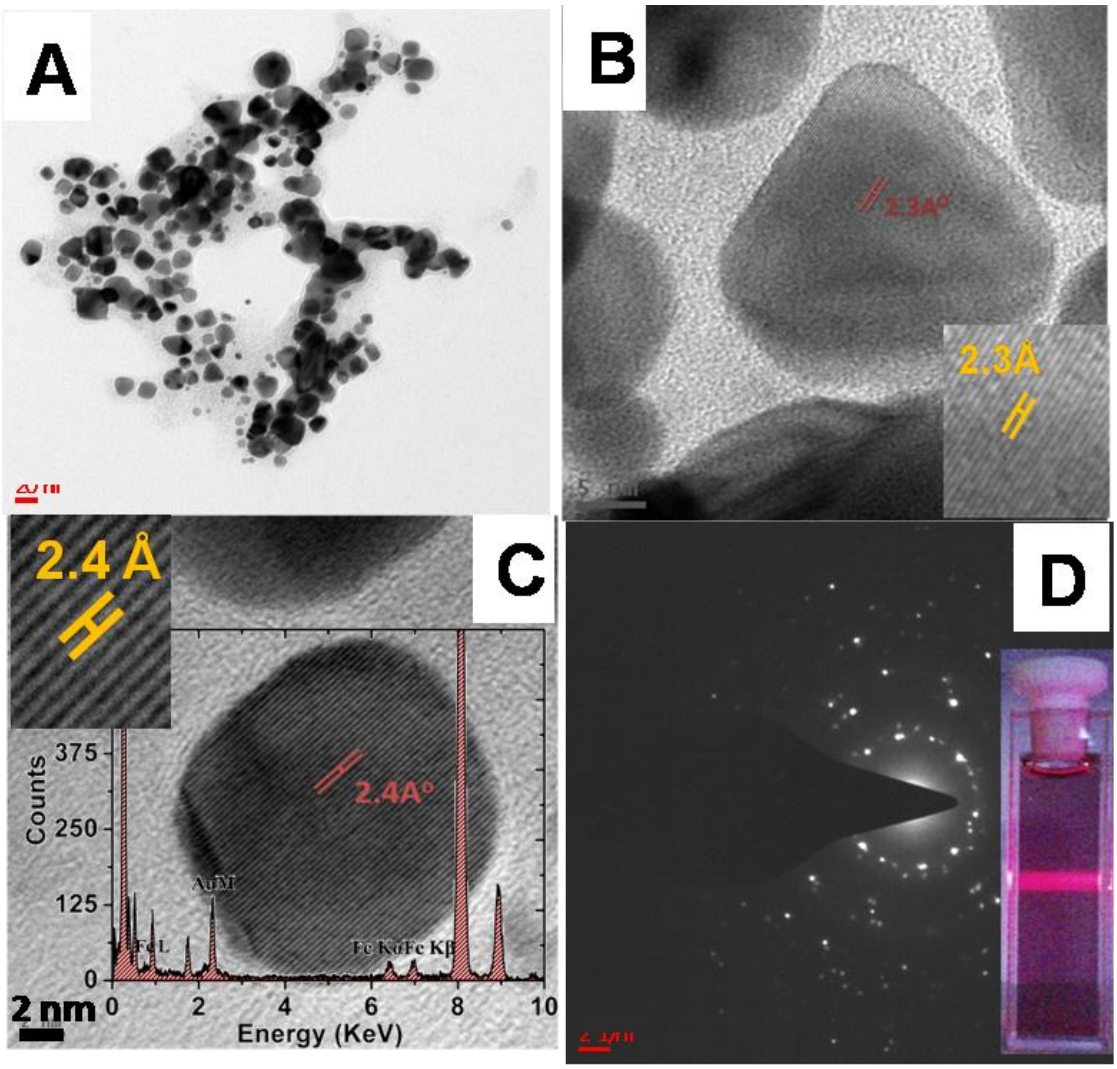

Figure 4.5*. 5A, B and C are TEM images of* ***10*** *in various magnifications displaying triangle, cubic Au NPs, inset of Figure 5C shows EDAX of* ***10****. 5D) SAED of* ***10*** *and the inset shows it's the Tyndall effect.*

4.3.8. Magnetic properties of 10:

Bulk magnetic measurement data of Fe(II) complexes **9** and **10** is shown in *Figure 4.6.* Both complexes had been exhibited SCO effect (*Figure 4.6a, b*) with a difference with respect to temperature in the temperature range of 320 K ↔2.5 K. Magnetic susceptibility (χT) of **9** was found to be 2.8 K mol^{-1} while heating and 0.28 K mol^{-1} under cooling. The HS state of compound was also above the experimental set-up temperature and the $T_{1/2}$was found to be in the room temperature range (*Figure 4.6a*). Temperature dependent magnetic susceptibility of complex **10** showed a

sluggish SCO behavior during the heating and cooling cycles. At 320 K the molar magnetic susceptibility (χT) was about 3.3 emu K mol^{-1}, which is slightly higher than the expected value for a

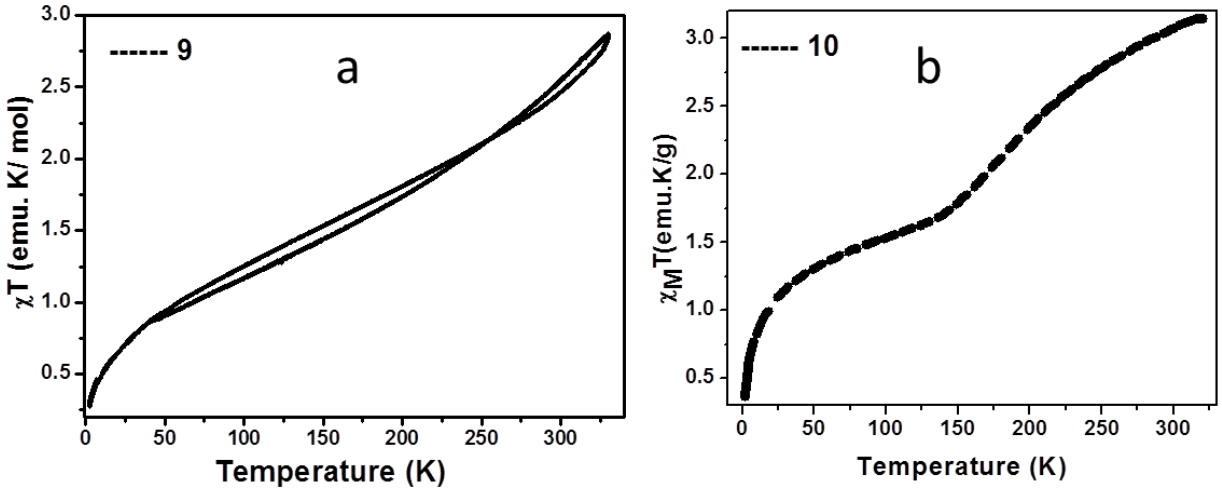

Figure 4.6**: χT vs T plots of **9** and **10.

HS iron(II) ion (S=2). At low temperature the observed high residual magnetic moment of ~1.5 emu K mol^{-1} is probably due to extra magnetic contribution from thiol stabilized Au N Ps connected to BPP via alkyl chain (*Figure 4.6b*). The origin of magnetism is still not well understood. Most commonly used theory is as follows; at the nanoscale the lattice distance contracts, as a result, inter atomic distance would be reduced. Due to this reason, there will be enhancement of inter electronic interaction of *d*-electrons such a way that number electrons and holes can be tuned in the 5d band of Au. Likewise when Au NPs were capped by thiol ligand, it has been found that number of holes is increased in 5d band, which is reason behind the display of magnetic behavior of Au NPs as compare to that of bulk.[18] Experiments are still under investigation to see consistency in magnetic data of complex **10**.

4.3.9. Fabrication of rectangle micro stripes by 10:

In the past literature Au NPs were put in a desired pattern by using electron beam lithography in order to control distance between adjacent particles such that plasmonic propagation to be occur along the pattern, leading into study of surface enhance Raman scattering effect.[19] In this chapter, to attempted to remotely excite the SCO NPs (**10**) by using propagating surface plasmon, for that an array of rectangle micro stripes composed of **10** were lithographically patterned to have close proximity between adjacent Au NPs. The procedure is as follows, two drops of diluted solution of **10** in DMF was drop casted on silica glass slide, further, it was covered by

replica of 0.5μm X 2μm polydimethylsiloxane (PDMS) mould and all the solvent was allowed to evaporate. The mould was subsequently peeled off to form micro stripes of **10** on the silica glass

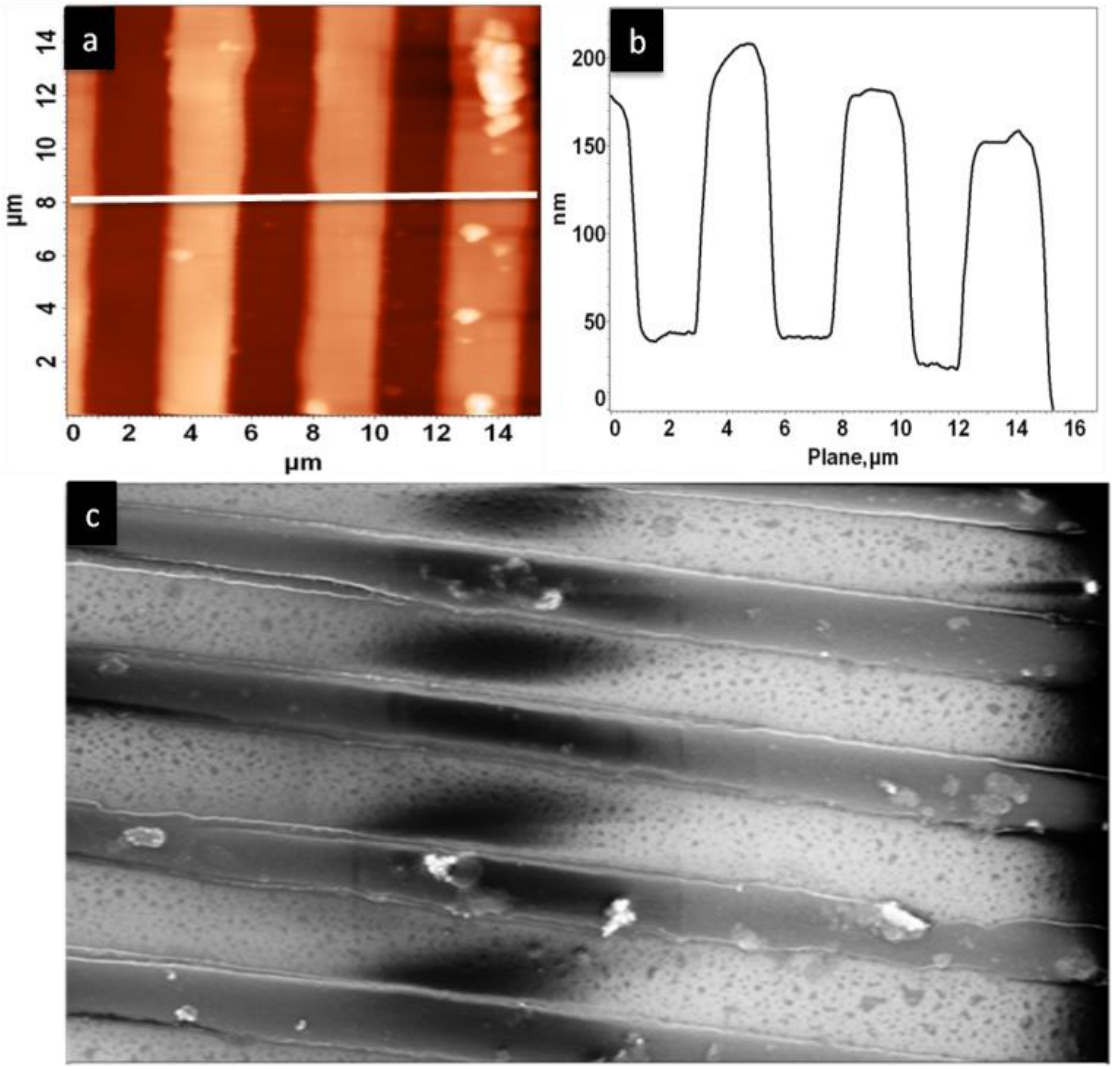

Figure 4.7*: a) AFM image of micro stripes composed of* ***10****. b) AFM topography profile of Figure 4.7a, c) FESEM image of micro stripes.*

slide. The rectangular micro stripes were characterized by AFM and FESEM. AFM topography (*Figure 4.7b*) of stripes showed their height and width in the range of ~150-200 nm and ~2 μm, respectively (see the white line drawn across the micro stripes in *Figure 4.7a*). Morphology of micro stripes provided by AFM was also affirmed by FESEM studies (*Figure 4.7c).* Study of SCO effect of iron complex **10,** through surface enhanced Raman scattering under light irradiation through plasmonic propagation is under progress. In addition to AFM and FESEM characterization of rectangular micro stripes, Raman imaging was also performed for micro stripes. A highly intense Raman Peak observed for **10**, due to SERS and for imaging an intense maker peak at 1529 cm^{-1}

(C=C) was selected to generate Raman imaging of rectangle microstripes in the area of 2 μm × 2 μm (*Figure 4.8*).

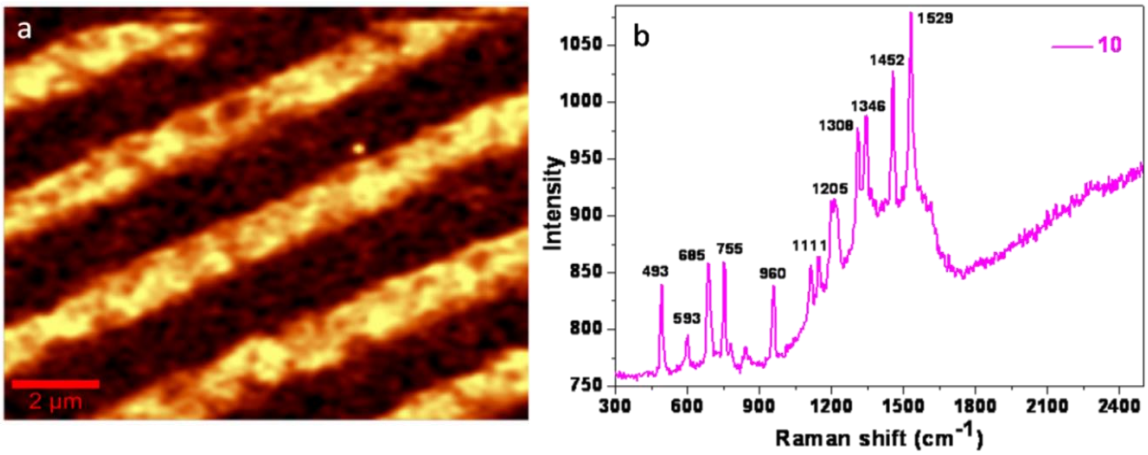

Figure 4.8**: a) Raman imaging of rectangle microstripes of **10**. b) Raman spectrum of **10.

4.4 Conclusions:

This chapter demonstrated novel synthesis and characterization of Au NPs (**L4** and **10**) protected by BPP unit carrying thiol functionality and its Fe(II) complex, respectively. Moreover a the size, shape and optical properties of Au NPs were also monitored in presence of $Fe(ClO_4)_2.H_2O$. Furthermore the fabrication of micro stripes of height and width in the range of ~150-200 nm and ~2 μm, respectively has been done via top-down approach. The stripes were used to pack the NPs create close proximity among Au NPs for plasmon propagation. This attempt has given a future opportunity to explore the SCO effect through plasmon propagation under light irradiation.

4.5 Synthetic procedures:

10-(2,6-di (1H-pyrazol-1-yl) pyridine-4-yl) dec-9-yn-1-ol (6):

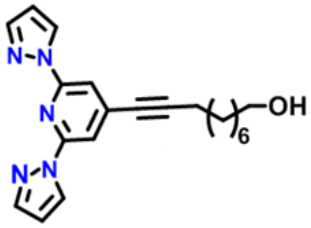

4-iodo-2,6-di(1H-pyrazole-1-yl)pyridine (**5**) (0.317 g,0.94 mmol), $Pd(PPh_3)_2Cl_2$ (0.032 g, 0.046 mmol), PPh_3(0.024 g, 0.0934 mmol), CuI (0.011 g, 0.062 mmol) were taken in a 100 mL two neck round bottom flask. To this solid mixture, high vacuum pump was applied through condenser for deoxynation. Subsequently dry triethylamine (15 mL), 1,4 dioxane (3 mL) were added slowly to the deoxynated solid mixture under N_2 atmosphere. After five minutes 9-Dec-yn-1-ol (0.217 g, 1.41 mmol) was added and refluxed it for 8 hours under N_2 atmosphere at 80°C. All the solvents were removed under reduced pressure through rotary evaporator and resultant crude product purified by column chromatography by using EtOAc : Hexane (3:7). Finally a pure compound **6** (90% yield) was

obtained as white colour solid. ^{1}H-NMR (400 MHz, $CDCl_3$): δ = 8.54 (d, 2H), 7.83 (S, 2H), 7.75 (d, 2H), 6.49 (M, 2H), 3.66 (m, 2H), 2.46 (m, 2H), 1.6-1.3(m, 2H) ppm. ^{13}C-NMR (200MHz, $CDCl_3$): δ = 149.9, 142.4, 137.6, 128.4, 111.5, 108.0, 97.4, 62.5, 32.6, 29.2, 25.6, 19.4 ppm. FTIR (KBr disc; ν in cm^{-1}): 3393, 3155, 2930, 2848, 2237, 1739, 1610, 1552, 1521, 1462, 1396, 1261, 1205, 1116, 1039, 954, 935, 868, 790, 760, 723. LCMS analysis m/z: Experimental value: 363.0, calculated value m/z: 363.46.

10-(2, 6- di(1H-pyrazol-1-yl) pyridine- 4-yl) Dec-9-ynyl-4-methylbezenesulphonate (7): To the suspension solution of **6** (0.3 g, 0.82 mmol) in DCM (15 mL) and NEt_3 (5 mL) solution, tosylchloride (0.314 g, 1.65 mmol) was added. The reaction mixture was stirred for 2 h at room temperature. Afterwards all the solvents were evaporated under reduced pressure and resultant black solid was purified by column chromatography with EtOAc/hexane (1:9), to obtain a colourless solid compound **7** (80%). ^{1}H-NMR (400 MHz, $CDCl_3$): δ = 8.5 (d, 2H), 7.8(s, 2H), 7.75 (d, 2H), 7.72 (d, 2H), 7.3 (d, 2H), 6.46 (m, 2H), 4.0 (m, -CH_2), 2.4 (m, 5H), 1.6 (m, 6H), 1.2(m, 6H) ppm. ^{13}C- NMR (200MHz, $CDCl_3$): δ = 150.0, 144.6, 142.5, 129.8, 129.6, 128.9, 127.8, 125.2, 111.54, 108.06, 97.19, 64.5, 29.6, 28.8, 25.7, 21.6, 19.4 ppm. FTIR (KBr disc; ν in cm^{-1}): 3115, 2922, 2852, 2224, 1784, 1730, 1610, 1552, 1523, 1464, 1398, 1358, 1267, 1207, 1176, 1113, 1049, 939, 900, 864, 821, 761, 661, 625, 574, 551, 474. LCMS analysis m/z: Experimental value: 518.14, calculated value: 517.64.

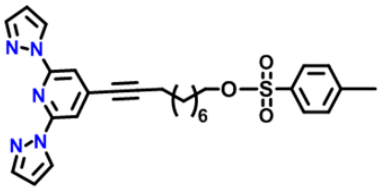

4-(10-bromodec-ynyl)-2, 6-di (1H-pyrazol-1-yl) pyridine (8): Compound **7** (0.13 g, 0.2511 mmol) was dissolved in dry acetone and lithium bromide (0.043 g, 0.502 mmol) was added to resultant solution. After 2 hours acetone has been removed by rotary evaporator under reduced pressure. Afterwards resultant mixture was extracted with DCM solvent in water. Evaporation organic layer (DCM) has produced white colour compound **8**, yield was found to be 75%. ^{1}H-NMR (400MHz, $CDCl_3$): δ = 8.48 (d, 2H), 7.78 (s, 2H), 7.71 (d, 2H), 6.4 (m, 2H), 3.39 (m, -CH_2), 2.43 (m, -CH2), 1.8 (m, -CH2), 1.58 (m, -CH_2), 1.43 (m, 4H), 1.27 (m, 4H) ppm. ^{13}C-NMR (200 MHz, $CDCl_3$): δ = 150.0, 142.3, 137.5, 127.0, 111.5, 108.0, 97.1, 78.4, 32.08, 28.9, 19.4 ppm. FTIR (KBr disc; ν in cm^{-1}): 3150, 3101, 2930, 2856, 2237, 1734, 1610, 1552, 1521, 1462, 1396, 1259, 1205, 1111, 1039, 954, 868, 790, 760, 626. LCMS analysis m/z: Experimental value: 426.0, calculated value: 426.35.

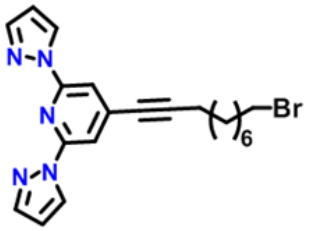

10-(2,6-di(1H-pyrazole-1-yl) pyridine-4-yl) dec-9-yne-1-thiol (L3): Compound **8**(0.100 g, 0.235mmol) was dissolved in 1:1 acetone/ethanol solution in a 100 mL round bottom flask. Thiourea (0.021, 0.282mmol) was added to this solution and left it for reflux at 80°C about 24 hours. Then all the solvents were evaporated and obtained crude was dispersed in NaOH (0.009 g, 0.235mmol) solution. This solution was refluxed for 1½ hour and cooled it to room temperature. Then obtained solid was purified by EtOAc/Hexane (1:9) solution, consequently, 50% of gel type colorless compound was observed. ^{1}H-NMR (400MHz, $CDCl_3$): δ = 8.51 (d, 2H), 7.80 (s, 2H), 7.73 (d, 1H), 6.46 (m, 2H), 2.7 (m, -SCH_2), 2.45 (m, 2H), 1.6 (m, 2H), 1.69 (m, 2H), 1.4 (m, 10H) ppm. ^{13}C-NMR (200MHz, $CDCl_3$): δ = 150.0, 142.4, 137.6, 127.0, 111.6, 108.0, 97.0, 78.3, 39.1, 29.7, 29.2, 29.1, 29.0, 28.8, 28.5, 28.2, 19.4 ppm. FTIR (KBr disc; ν in cm^{-1}): 3158, 3112, 2919, 2848, 2358, 2339, 2225, 1739, 1608, 1550, 1459, 1394, 1263, 1205, 1110, 1031, 956, 933, 862, 771. LCMS analysis m/z: experimental value: 380.10, calculated value: 379.21.

Synthesis of pure thiol complex (9): Ligand **L3** (0.050 g, 0.132 mmol) was first dissolved in 15 mL of acetonitrile solvent in 100 mL round bottom flask and Fe $(ClO_4).H_2O$ (0.0168 g, 0.066 mmol) was added to this resultant ligand solution followed by stirring at 60 °C about 1 hour. Then solution was allowed to cool till it reaches room temperature, further, it was poured in diisopropylether to achieve pure brown colour precipitate of thiol complex **2**, yield was calculated to be 60%. FTIR (KBr disc; ν in cm^{-1}): 3140, 3112, 2925, 2700, 2400, 2339, 2225, 1739, 1600, 1550, 1403, 1394, 1255, 1220, 1111, 1031, 940, 920, 862, 680. Raman (neat pellet; cm^{-1}): 2229, 1638 (C=C), 1452, 1384, 1215, 1021, 936, 801, 632, 479, 370, 243.

Synthesis of Au NPs capped by L3 (L4): $HAuCl_3.3H_2O$ (0. 186 g, 0.474 mmol) was taken in 2mL millipore water in 100 mL round bottom flask. Tetraoctylammonium bromide (TOAB) (0.518 g, 0.948 mmol) in DCM (2mL) and ligand **L3** (0.090 g, 0.237 mmol) in 2 mL DCM were introduced to this solution. Resultant mixture was stirred for 10 minutes at room temperature. Finally freshly prepared sodiumborohydride (0.143 g, 3.792 mmol) solution in 2mL millipore water was added drop by drop. Immediately a yellow colour solution has turned into dark brown which indicates that formation of Au NPs capped by thiol ligand **L3**. The resultant solution was left it for stirring for 15 minutes at RT and then organic layer was separated

and rest of aqueous layer washed with washed with extra amount of DCM solvent. Afterwards, all organic fractions were mixed and evaporated to get dark brown color solid with excess amount of TOAB. Excess amount of TOAB has been removed by washing with methanol solvent to achieve thiol capped Au NPs (**L4**) in pure form and it was characterized by UV-Visible spectroscopy, ^{1}H-NMR and TEM. ^{1}H-NMR (400MHz, $CDCl_3$): δ = 8.29 (d, 2H), 7.57 (s, 4H), 6.27 (d, 2H), 2.32 (m, 2H), 1.1-1.8 (m, 16H) ppm. UV-Visible ($\lambda_{abs\ max}$ in nm): 520, 334, 270. FTIR (KBr disc; ν in cm-1): 2921, 2854, 2337, 2225, 1623, 1556, 1523, 1457, 1405, 1340, 1268, 1214. Raman (neat pellet; cm^{-1}): 2239, 1632 (C=C), 1555, 1529, 1497, 1458, 1408, 1386, 1216, 1123, 1061, 1016, 929, 634, 253.

Synthesis Fe (II) complex of L4 (10):

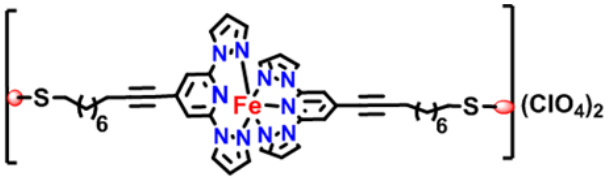

Initially ligand **L4** (0.05 g) was dissolved in 3:7 mixtures of DCM and acetonitrile in 100mL round bottom flask. To this solution, very dilute solution of $Fe(ClO4)_2$. H_2O was added slowly drop by drop and solution was left it for about 20 minutes at room temperature. Insoluble complex **10** was settled as black precipitate which was separated by decanting solvent without losing compound. The black solid was further washed with DCM and methanol to remove excess of ligand and metal ion. Now pure complex was characterized by ^{1}HNMR, UV-Visible spectroscopy and TEM. ^{1}H-NMR (400MHz, $CDCl_3$): δ = 8.5, 7.65, 6.40, 2.4, 17-0.8 ppm. UV-Visible ($\lambda_{abs\ max}$ in nm): ~ 500-600, 304, 270. FTIR (KBr disc; ν in cm^{-1}): 2931, 2854, 1627, 1529, 1452, 1403, 1263, 1230, 1099, 968, 860, 767. Raman (neat pellet; cm^{-1}): 1529, 1452, 1346, 1308, 1205, 1111, 960, 755, 685, 593, 493.

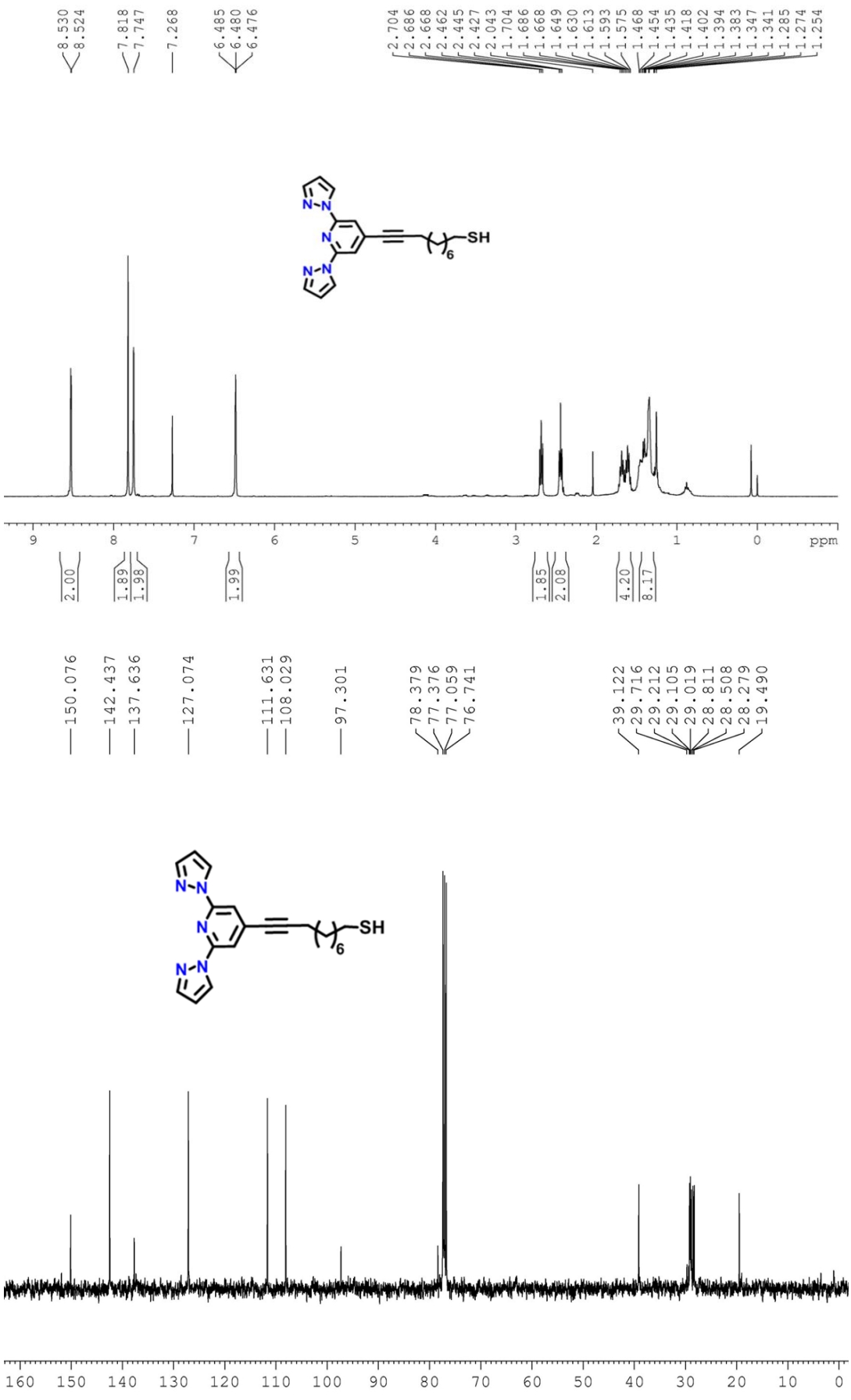
8.530
8.524
7.818
7.747
7.268
6.485
6.480
6.476
2.704
2.686
2.668
2.462
2.445
2.427
2.043
1.704
1.686
1.668
1.649
1.630
1.613
1.593
1.575
1.468
1.454
1.435
1.418
1.402
1.394
1.383
1.347
1.341
1.285
1.274
1.254
SH
6
9 8 7 6 5 4 3 2 1 0 ppm
2.00
1.89
1.98
1.99
1.85
2.08
4.20
8.17
150.076
142.437
137.636
127.074
111.631
108.029
97.301
78.379
77.376
77.059
76.741
39.122
29.716
29.212
29.105
29.019
28.811
28.508
28.279
19.490
SH
6
160 150 140 130 120 110 100 90 80 70 60 50 40 30 20 10 0

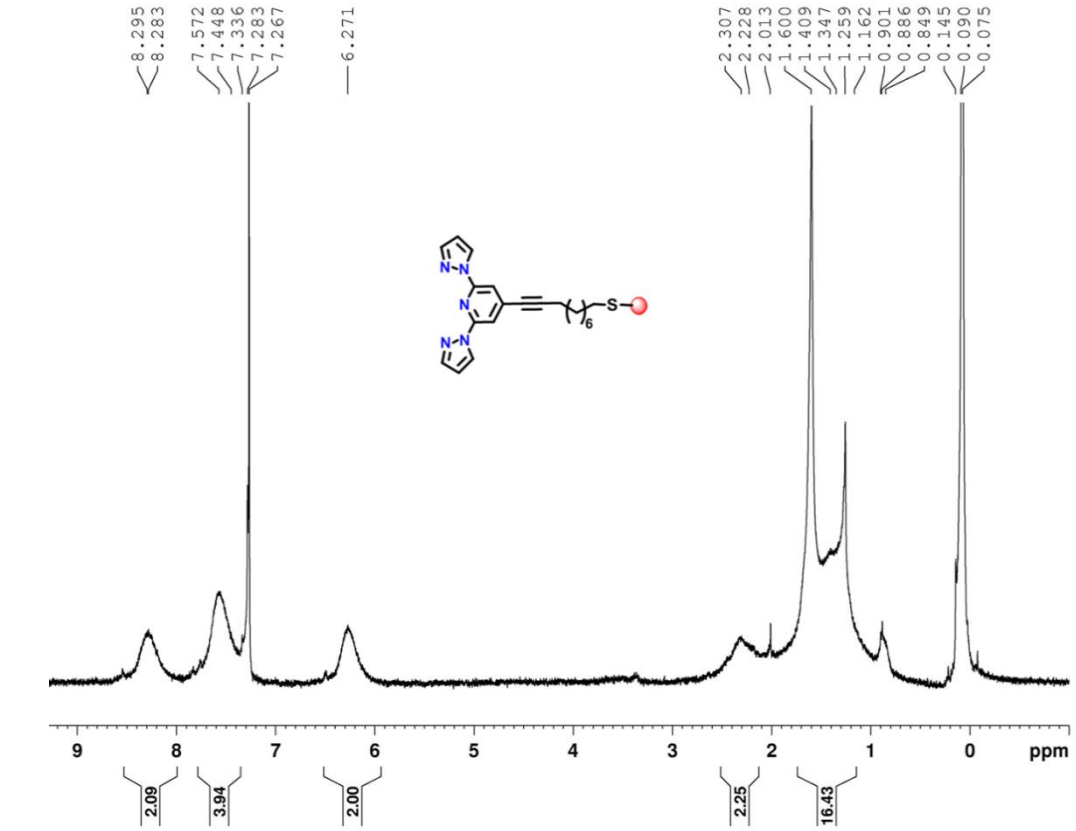
8.295
8.283
7.572
7.448
7.336
7.283
7.267
6.271
2.307
2.228
2.013
1.600
1.409
1.347
1.259
1.162
0.901
0.886
0.849
0.145
0.090
0.075
9
8
7
6
5
4
3
2
1
0
ppm
2.09
3.94
2.00
2.25
16.43

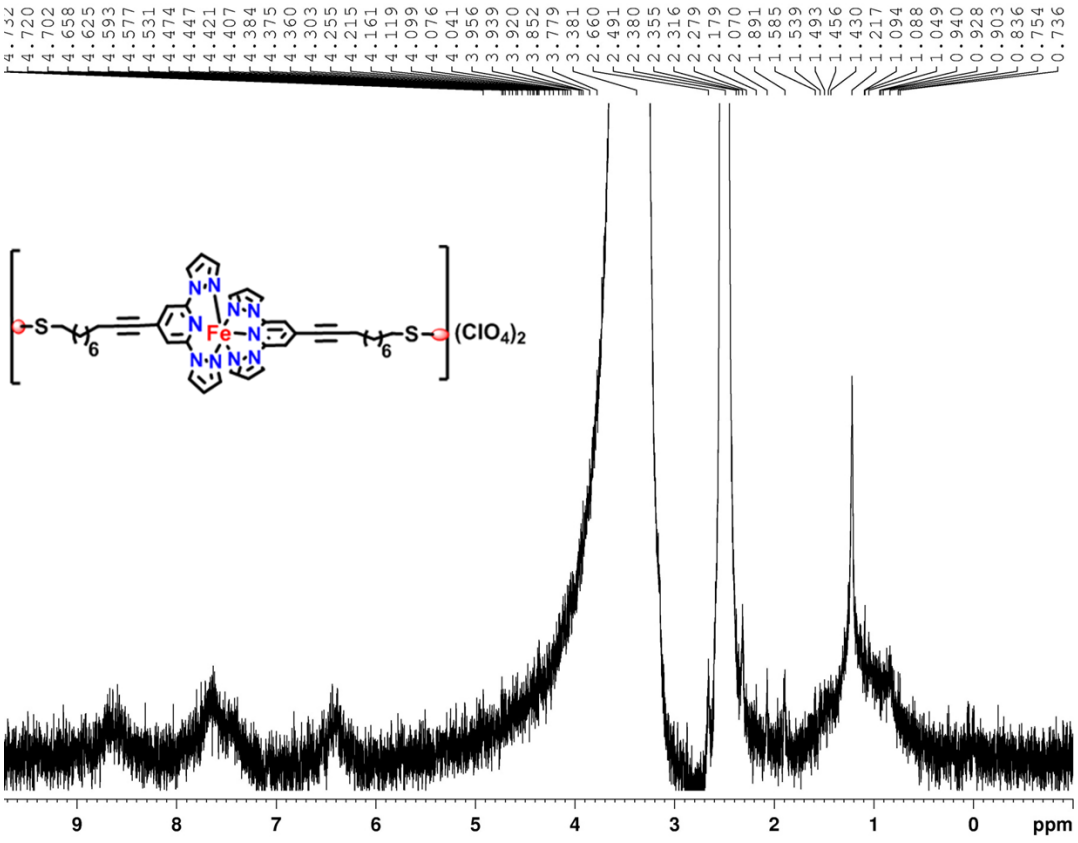
4.720
4.702
4.658
4.625
4.593
4.577
4.531
4.474
4.447
4.421
4.407
4.384
4.375
4.360
4.303
4.255
4.215
4.161
4.119
4.099
4.076
4.041
3.956
3.939
3.920
3.852
3.779
3.381
2.660
2.491
2.380
2.355
2.316
2.279
2.179
2.070
1.891
1.585
1.539
1.493
1.456
1.430
1.217
1.094
1.088
1.049
0.940
0.928
0.903
0.836
0.754
0.736
Fe
(ClO4)2
9
8
7
6
5
4
3
2
1
0
ppm

LCMS-2010A DATA REPORT
SCHOOL OF CHEMISTRY
UNIVERSITY OF HYDERABAD

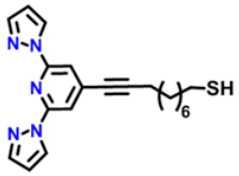

User : Admin
Sample : SH
Inj. Volume : 5.000
Data Name : C:\LCMSsolution\User\Data\SH-APCI-POS1.qld
Method Name : C:\LCMSsolution\User\Method\esi.qlm

LC Chromatogram

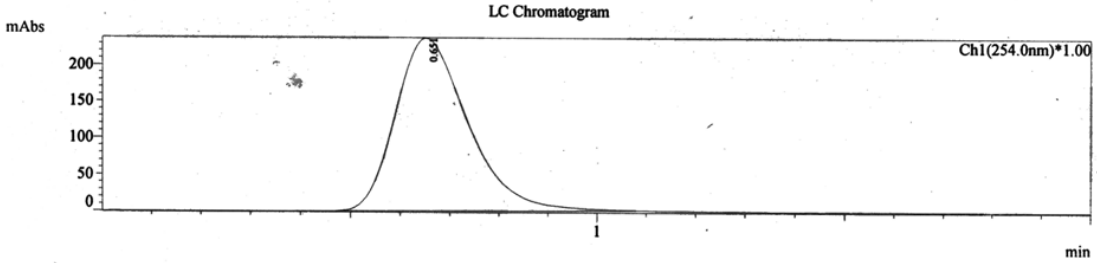

MS Spectrum

Line#:1 R.Time:0.795(Scan#:48) Positive
MassPeaks:318 BasePeak:380.25(12304297)
RawMode:Single 0.795(48)
BG Mode:Peak Start 0.577(35)

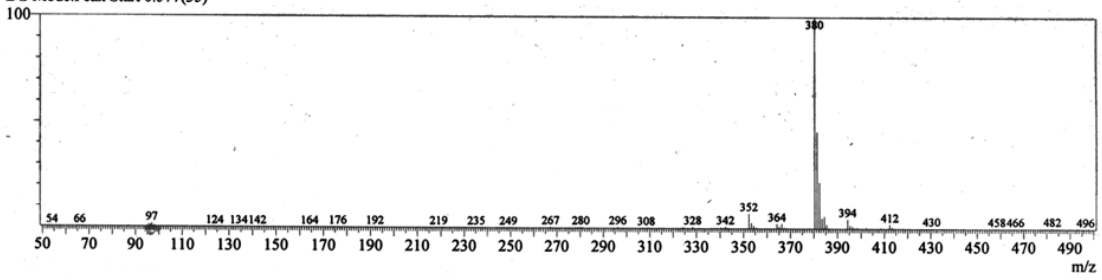

MS Peak Table

Peak#	R.Time	I.Time	F.Time	Area	Height	A/H	Mark	%Total	Name	Base m/z	Base Int.
1	0.795	0.577	1.010	304473890	24751492	12.30		100.00		380.25	12304297
				304473890	24751492			100.00			

OPERATOR

FLASH EA 1112 SERIES CHN REPORT
SCHOOL OF CHEMISTRY
UNIVERSITY OF HYDERABAD

Method filename:	E:\Program Files\Thermo Finnigan\Eager 300 for EA1112\DATA\Sys_data_ex
Sample ID:	BPPSH (# 14)
Analysis type:	UnkNown
Chromatogram filename:	UNK-13082013-14.dat
Sample weight:	1.118

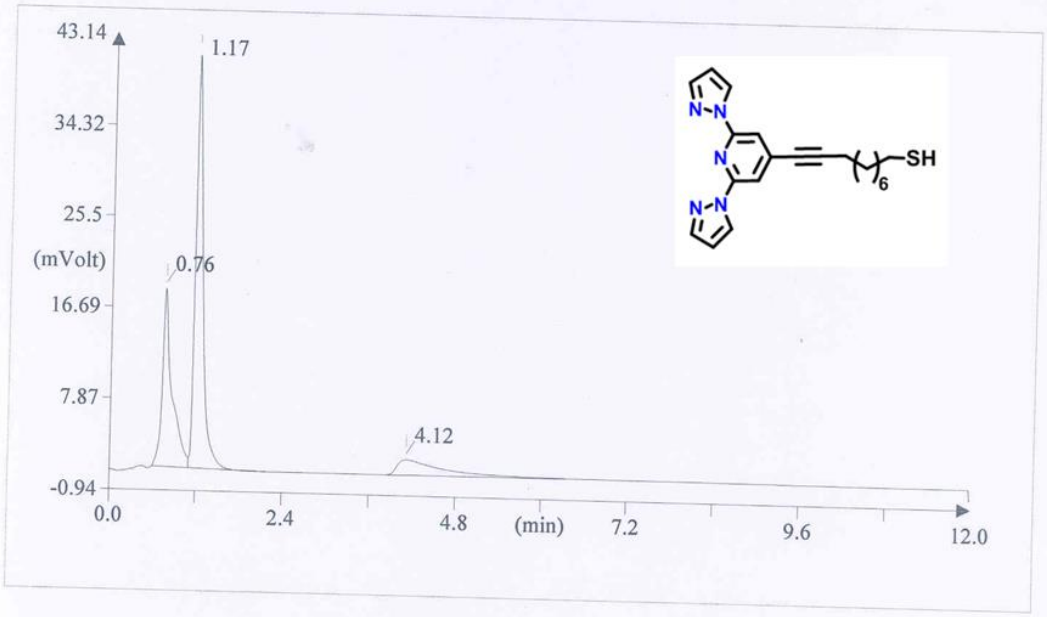

Element Name	Element %	Ret. Time
Nitrogen	18. 51	0. 76
Carbon	66. 32	1. 17
Hydrogen	6. 71	4. 12

References:

1. Schmid, G.; Simon, U. *Chem. Commun*. **2005**, 697-710.
2. Lez, B. R. G.; Burrows, A.; Watanabe, M.; Kielyb, C. J.; Marza, L. M. *J. Mater. Chem*. **2005**, *15*, 1755-1759.
3. Daniel, M.; Astruc, D. *Chem. Rev*. **2004**, *104*, 295.
4. (a) Brust, M.; Fink, J.; Schiffrin, D. B. D.J.; Kielyb, C. J. *Chem. Commun*. **1995**. (b) Chen, Y.; Ching Hung, Y.; Liau, I.; Huang, G. S. *Nanoscale Res. Lett*. **2009**, *4*, 858-864.
5. Wei, G.; Wang, L.; Sun, L.; song, Y.; Sun, Y.; Guo, C.; Yang, T.; Li, Z. *J. Phys. Chem. C*. **2007**, *5*, 1977.
6. Ulman, A. *Chem. Rev*. **1996**, *4*, 1535.
7. Pearson, R. G. *J. Am. Chem. Soc*. **1963**, *85*, 3533.
8. Love, J. C.; Estroff, L. A.; Keiebel, J. K.; Nuzzo, R. G.; Whitesides, G. M. *Chem. Rev*. **2005**, *105*, 1103-1169.
9. (a) Chandrasekhar, N.; Chandrasekar, R. *Dalton Trans*. **2010**, *39,* 9872-9878. (b) Chandrasekar. R.; Schramm, F.; Fuhr, O.; Ruben, M. *Eur. J. Inorg. Chem*. **2008**, 2649-2653.
10. (a) Gutlich, P. Nucl. Instr. Meth. Phys. Res. 1993, B76, 387.(b) Bousseksou, A.; Molna. G. R.; Matouzenko. G. *Eur. J. Inorg. Chem*. **2004**, 4353-4369.
11. Cavallini, M.; Bergenti, I.; Milita, S.; Ruani, G.; Salitros, I.; Qu, Z.; Chandrasekar, R.; Ruben, M. *Angew. Chem. Int. Ed*. **2008**, *47*, 8596-8600.
12. Chandrasekar, R.; Shramm, F.; Fuhr, O.; Ruben, M. *Eu. J. Inorg. Chem*. **2008**, 4860-4862.
13. Daniel, M.; Astruc, D. *Chem. Rev*. **2004**, *104*, 1.
14. Crespo, P.; Litran, R.; Rojas, T. C.; Multigner, M.; de la Fuenta, J. M.; Sanchez-Lopez, J. C.; Garcia, M.A.; Hernando, A.; Penades, S.; Fernandez, A. *Phy. Rev. Lett.* **2004**, *93*, 087204-1.
15. (a) Hasan, M.; Bethell, D.; Brust, M. *J. Am. Chem. Soc*. **2002**, *124*, 1132-1133. (b) Pramod, P.; Sudeep, P. K.; Thomas, K. G.; Kamat, P V. *J. Phys. Chem. B*. **2006,***110*, 42.
16. Eustis, S.; El-Sayed, M. A. *Chem. Soc. Rev*. **2006**, *35*, 209-217.
17. Lin, G.; Lu, W.; Cui, W.; Jiang, L. *Cryst. Growth Des*. **2010**, *10*, 3.
18. Crespo, P.; Litran, R.; Rojas, T. C.; Multigner, M.; de la Fuente, J. M.; Sanchez-Lopez, J. C.; Garcia, M. A.; Hernando, A.; Penades, S.; Fernandez, A. *Phy. Rev. Lett*. **2004**, *93*, 087204-1.
19. Mohiddon, M. A.; Sangani, L. D. V.; Krishna, M. G. *Chem. Phy. Lett.* **2013***, 588,* 160-166.

Chapter 5

Organic nano-vesicular cargoes for drug delivery: synthesis, esicle formation, controlling "pearling" states and terfenadine loading/release studies

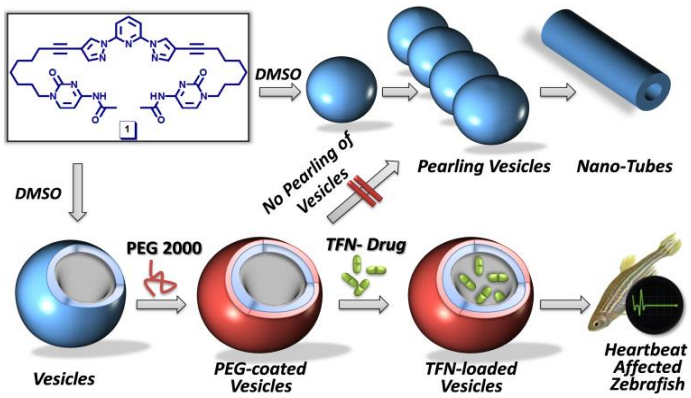

5.1 Abstract:

"Sustained drug delivery systems" which are designed to accomplish long-lasting therapeutic effect are one of the challenging topics in the area of nanomedicine. We developed an innovative strategy to prepare nontoxic and polymer stabilized organic nanovesicles (diameter: 200 nm) from a novel bolaamphiphile, where two hydrogen bonding acetyl cytosine molecules connected to 4,4"-positions of the 2,6-bispyrazolylpyridine through two flexible octyne chains. The nanovesicles behave like biological membrane by spontaneously self-assembling into "pearl-like" chains and subsequently forming long nanotubes (diameter: 150 nm), which further develop into various types of network-junctions through self-organization. For drug loading and delivery applications, the nanovesicles were externally protected with biocompatible poly(ethyleneglycol)-2000 to prevent them from fusion and ensuing tube formation. Nontoxic nature of the nanovesicles was demonstrated by zebrafish teratogenicity assay. Biocompatible nanovesicles were loaded with "Terfenadine" drug and successfully utilized to transport and release drug in sustained manner (up to 72 h) in zebrafish larvae, which is recognized as an emerging in vivo model system.

5.2 Introduction:

Synthetic nano-/microscale vesicles are of great interest because they emulate complex properties of biological cell membranes.[1–4] Most of the biological membranes are flexible; therefore they show multidimensional shape transformation to form zero-dimensional (0D) microspheres, one dimensional (1D) cylinders and long flexible tubular structures. Hence mimicking the properties of naturally occurring vesicles by polymer, peptide, or dendrimer based synthetic vesicles is of great interest since they are potential tool for nanomedicine, biosensors, and biophysical and bioelectronic applications.[5–8] For instance, in the budding area of nanomedicine, nontoxic vesicles act as tiny spherical containers for storage and delivery of chemicals/reagents in biochemical reactions. Nanodrug delivery systems protect drug from degradation and deliver drug at specific sites there by increasing efficacy of treatment.[5, 9, 10] Sometimes, multiple vesicles fuse due to the interaction of surface molecules between many vesicle membranes, a phenomenon known as "pearling," which leads to the formation of nanotubular vesicles (NTVs).[11] Synthetic NTVs are also proposed for the transportation of chemicals between vesicles. Hence laboratory synthesis of nontoxic bioinspired molecules capable of mimicking the biological membrane is a challenging task, since they can act as life-saving drug delivery and sustained drug release cargoes. Although a plethora of block copolymer based vesicles are explored for drug delivery applications, vesicles from small biologically inspired designer molecules are rare. Earlier, we have found that aromatic rigid core 2,6-bispyrazolylpyridine (BPP) connected with long alkyl groups forms vesicles.[12] Hence for drug loading application, the use of rigid molecules decorated with one of the base pairs found in DNA and RNA is a promising starting point to achieve nontoxic drug delivery systems. One of the ingredient problems with soft vesicles is their tendency to form tubes through fusion mechanism.

In this chapter we present our strategy to prepare nontoxic and polymer stabilized vesicles from a novel bolaamphiphile **L5**, that is, two hydrogen bonding N4-acetyl cytosine molecules connected to 4, 4"-positions of the BPP using two flexible octyne chains. The vesicles are loaded with terfenadine (TFN) drug and successfully utilized to transport and release drugs in zebrafish larvae, which is utilized as an emerging in vivo model system (*Figure 5.1*). Since heart function of Zebrafish is resembles with human beings, ECG of human beings and Zebrafish are found be sam. Therefore Zebrafish became good model for drug assessment. In this chapter we present the synthesis of **L5** and prevention of fusion driven nanotubes formation by protecting the nanovesicles (NV) with biocompatible PEG 2000, TFN drug loading, and its sustained drug releasing tendency. The nanovesicles were thoroughly characterized using scanning electron microscope (SEM), transmission electron microscope (TEM), and atomic force microscopy (AFM).

5.3 Synthetic scheme of L5:

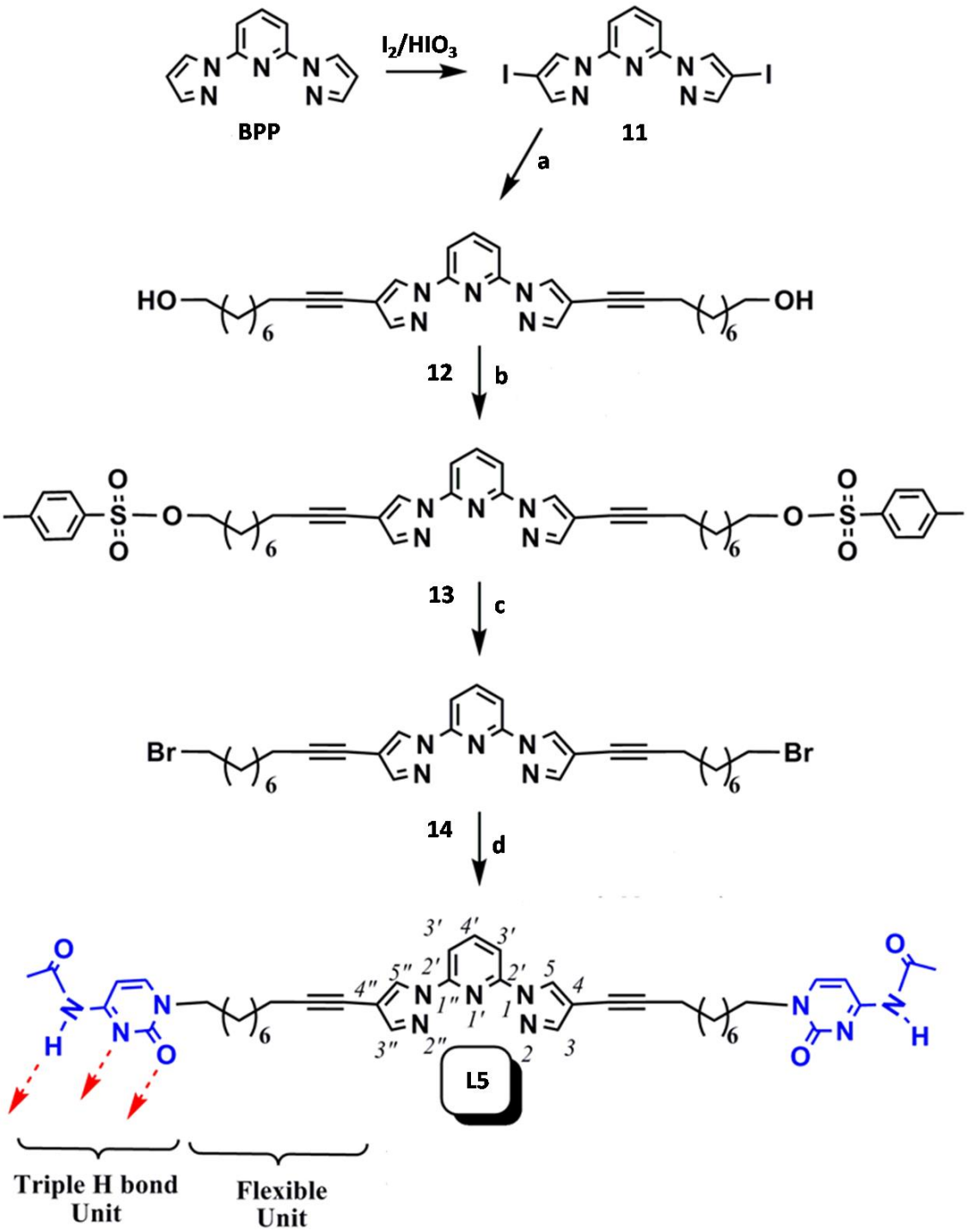

Scheme 5.1*: Synthesis of cytosine decorated to 2,6-bispyrazolyl-pyridine derivative (**L5**). General reaction conditions: (a) **2** (1.07mmol), $Pd(PPh_3)_2Cl_2$ (0.106mmol), PPh_3 (0.21mmol), CuI (0.14mmol), Et_3N/1,4 dioxane, N_2, 9-dec-yn-1-ol (1.41mmol), 80℃, 8 h, 80%; (b) **3** (0.58mmol), tosyl chloride (2.32mmol), DCM/NEt_3, RT, 2h, 75%; (c) **4** (0.24mmol), LiBr (0.97mmol), dry acetone, RT, 2h, 89%; (d) N4-acetyl cytosine (1.40mmol), K_2CO_3 (1.81mmol), dry DMF, **5** (0.47mmol), 80°C, 16 h, 55%.*

5.4 Results and discussion:

5.4.1 Synthesis of bolaamphiphileL5:

Molecule **L5** was synthesized in six steps from BPP (*Scheme 5.1*). Iodination of the BPP had yielded compound**11**in as per our reported procedure.[13, 14] Attachment of "linker molecule" decyn-1-ol to **11** was achieved by adopting Sonogashira cross-coupling conditions to get **12** in good yields (80%). Compound **12** was tosylated in DCM solvent in presence of triethylamine as base to give **13** in 75% yields. Compound **14** was prepared in excellent yield (89%) upon treatment of **13** with LiBr in acetone at room temperature. The target bola-amphiphile **L5** containing water soluble end groups connected to a hydrophobic alkyl chains was obtained in 55% yield, by treating **14** with N4-acetyl cytosine in presence of potassium carbonate at 80 °C.

5.4.2 Variable temperature of ^{1}H-NMR:

Since ^{1}H-NMR technique is very sensitive in detecting inter and intra molecule hydrogen bonding in several kinds of organic molecules. Therefore variable temperature ^{1}H-NMR of **L5** was

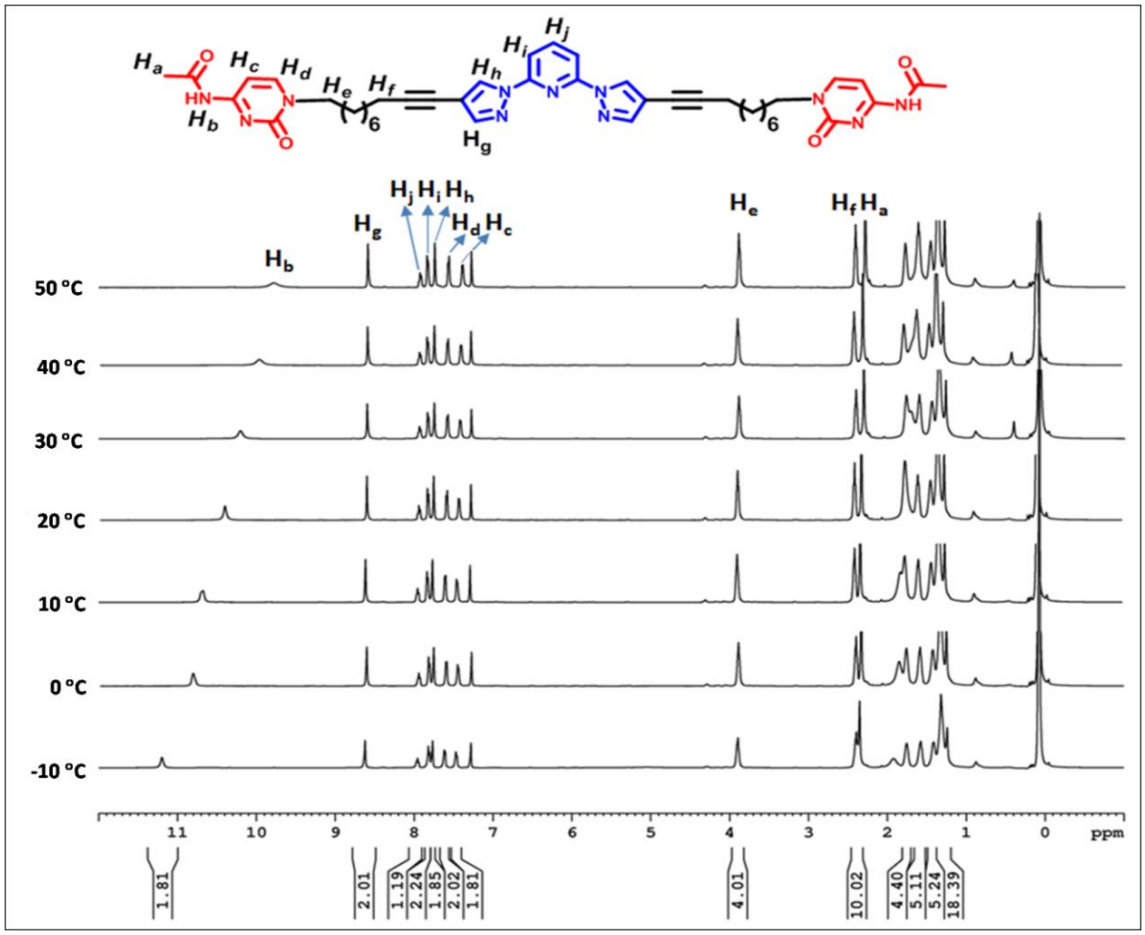

Figure 5.1*: Variable temperature NMR of* ***L5*** *in* $CDCl_3$.

perfomed. 10 mg of Compound **L5** was taken in NMR tube and dissolved it in 0.5mL of $CDCl_3$ and to obtain spectra at different temperature intervals, starting from -10 °C till 50 °C. As a result of this experiment, variation of chemical shift of H_b (-NH) proton of **L5** was monitored while varying temperature. With rising temperature, chemical shift increases gradually towards up field and finally reaches the value 9.8 ppm. While decreasing the temperature till -10 °C, chemical shift found to be 11.2 ppm because of strong interaction between neighboring molecules. Comparative NMR spectra of **L5** were depicted in *Figure 5.2* at various temperatures.

5.4.3 Investigation of nanostructures of L5:

To study the aggregation driven nanostructure formation, a solution containing 2 mg of compound **L5** in DMF (12 mL)/water (6 mL) was prepared and stabilized for an hour. Drop casting this solution on silica followed by SEM analysis showed the formation of clear tubular networks of several microns long (*Figure 5.2*). To understand the mechanism of formation of nanotubular network assemblies, the same solution of **L5** was drop casted immediately without stabilization on a carbon coated TEM grid. Interestingly, the TEM micrographs showed the presence of tiny vesicles of size in the range of 200 nm (*Figure 5.3a*) and some aggregated pearl-chain linked vesicles of size in the range of ~150 nm (*Figure 5.3b*). Additionally the generation of 1D pearl chain-like assembly by the fusion of vesicles indicates the formation of nanotubular network (*Figures 5.3c*, *d*). To further verify the fusion of spherical vesicles into nanotubes on silica surface AFM studies were

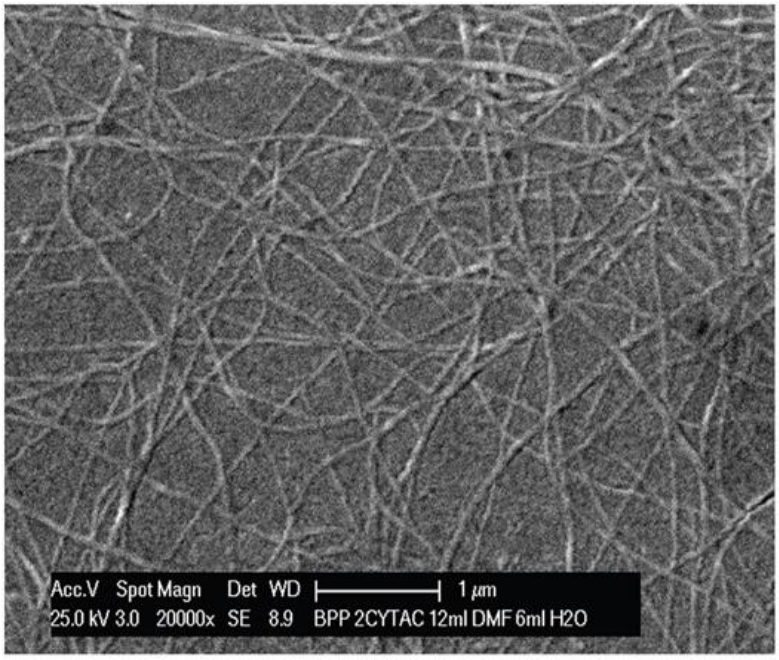

Figure 5.2*: SEM micrographs of nanotubular network assemblies formed from compound **L5** in DMF/water.*

undertaken. The AFM topography clearly revealed the presence of nanovesicles (NVs) of sizes ~200 nm (*Figures 5.4a, b*). Interestingly, some of the samples showed spontaneous formation of pearl-chain like vesicular assemblies or nanotube integrated vesicles, pointing out to vesicles fusion. For every 1 μm chain length ca. 5 fused vesicles were found, which is matching with the average diameter of the vesicles (*Figures 5.4c, d*). Continuous AFM measurement revealed the evolution

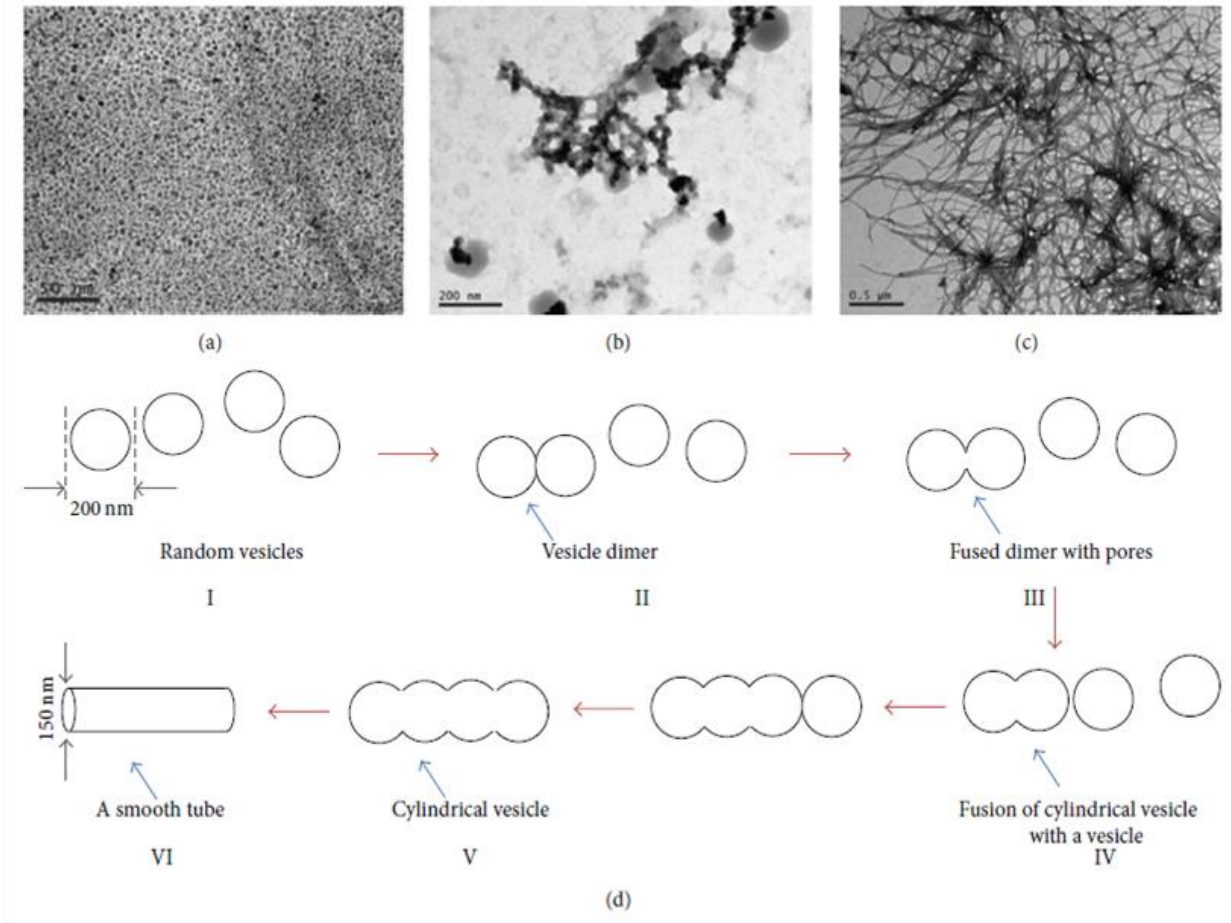

Figure 5.3*: TEM micrographs of nanostructures obtained from compound* ***L5*** *in DMF/water mixture: (a) distribution of nanovesicles; (b) pearl chain like fused nanovesicles; (c) nanotubes; (d) proposed mechanism of nanotube formation by vesicle fusion.*

of smooth nanotubular structures of diameter 160 nm from the pearl-chain like vesicular assemblies due to the molecular reorganization (*Figures 5.4e* and 5.*4f*). The finally formedtubes diameter (~160 nm) is less than the initial vesicle diameter of a single isolated vesicle (~200 nm) due to the stretching of the fused vesicles during the 1D tube formation. The diameter of the tube is determined by the balance between surface tension and tube bending rigidity, preventing membrane collapse. The outer surface of the tubes is very smooth with a roughness smaller than 1 nm (*Figures 5.4g* and 5.*4h*). This result demonstrated the flexible nature of the presented synthetic

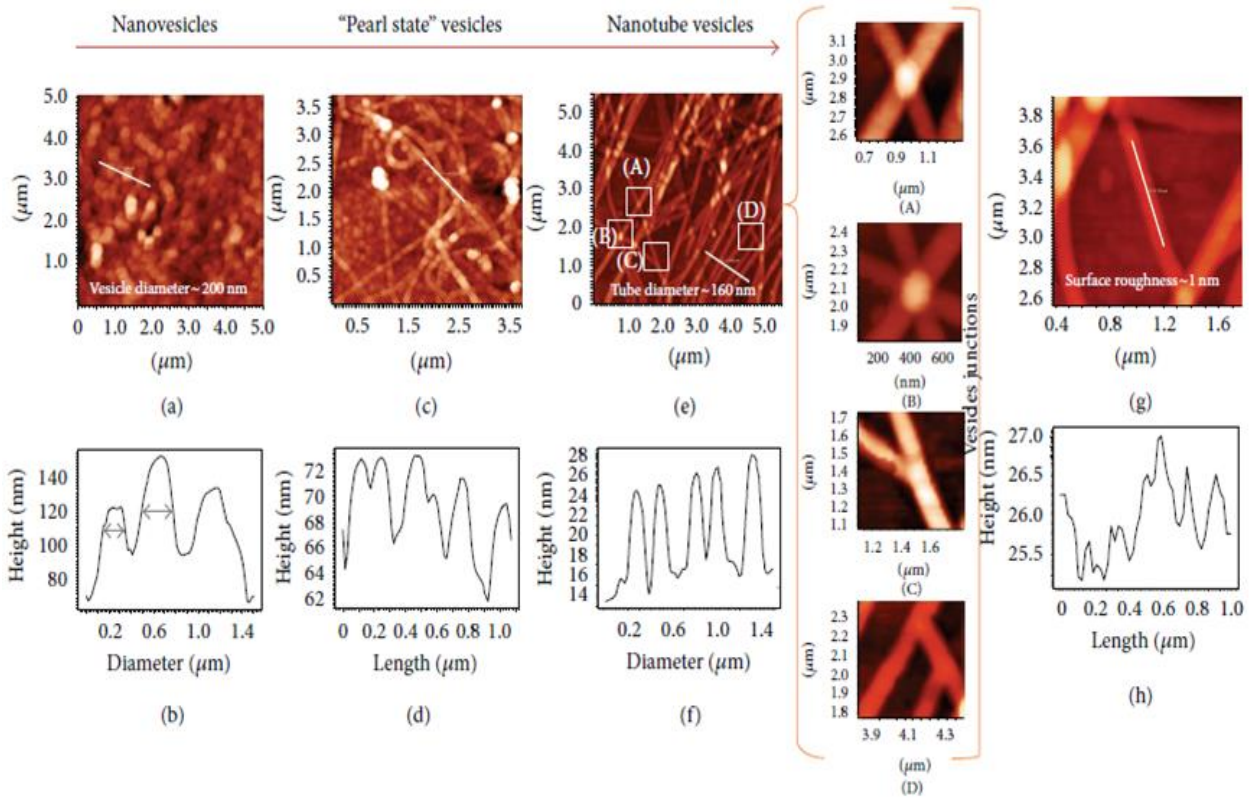

Figure 5.4: *AFM mechanistic analysis of the formation of nanotubes from nanovesicles: (a) randomly distributed vesicles, (c) fusion of vesicles to form pearl-chain like structures, (e) nanotubes, and (g) roughness of a tube. The corresponding profile analyses are shown in (b), (d), (f), and (h), respectively.*

membrane composed of **L5**. Another interesting finding of the nanotubes is their tendency to form various types of network junctions through self-organization (*Figure 5.4e*, insert).

5.4.4 Zebrafish studies: (This work has been done in collobration with Dr. M. Rajadurai and Dr. P. Kulakarni, DRILS, UOH).

Zebrafish teratogenicity assessment: Zebrafish maintenance, breeding, and embryo collection was carried out by methods described previously.[15,16] Briefly, wild-type adult Zebrafish (5-6 months old)were maintained at 28 °C under a 14 : 10 h light and dark cycle. Fish were allowed to breed (in a ratio of 2 females: 3 males) in the morning under the stimulation of light. Embryos were collected into petri dish containing embryo medium and incubated at 28 °C temperature. The teratogenicity study was performed using 6 embryos that were incubated with vehicle, positive control, and various concentrations of test compound **L5** until 5 dpf. The embryos were then anesthetized using 0.008% tricaine solution and various phenotypic parameters were evaluated; namely, body shape, somites, notochord, tail, intestine, fins, brain, upper jaw, heart, lower jaw, liver, and swim bladder were observed for defects in morphology.[17] Each embryo was scored based on their level of toxicity from 5 being nontoxic and 0.5 being highly toxic. The scoring was conducted by blinded observers

***Table 5.1*:** Results of Zebrafish embryo toxicity study with toxicological indices and major organs/systems affected in positive control and at MTC in test compounds *(- no effect,* **x-** *slightly toxic,* **xx-** *moderately toxic,* **xxx-** *severely toxic*).

	Tested compound (L5)	**Phenobarbital**
Test Concentrations (µM)	0.03, 0.1, 0.3, 1, 3, 10, 30	3000
Statistically Significant Toxic Concentration (µM)	-	Positive Control
No Observed Adverse Effect Level (NOAEL) (µM)	30	
Minimal Toxic Concentration (MTC) (µM)	-	
Parameters of toxicity at MTC		
Body Shape	**x**	**Xxx**
Somites	-	**Xxx**
Notochord	-	**Xxx**
Tail	-	**Xxx**
Fins	-	**Xxx**
Brain	-	**Xxx**
Upper jaw	-	**Xxx**
Heart	-	**Xx**
Intestine	**x**	**Xxx**
Lower jaw	-	**Xx**
Liver	-	**Xxx**
Swim Bladder	**x**	**Xxx**

and was done according to the procedures described earlier.[18] *Table 5.1* reveals that, score of Zebrafish is same at different concentration of compound **L5** where as in case of Phenobarbital, the Zebrafish score was less comparatively. Zebrafish teratogenicity assay study has been said that compound **L5** found to be nontoxic until the concentrations tested.

5.4.5 Control over nanostructure using stabilizing agents:

To demonstrate application of NVs for drug delivery, in the first step, different conditions were screened to stabilize vesicles in solution state and prevent formation of tubular structures. We

intended to use polyethylene glycol (PEG) as stabilizing agent since it is biologically neutral and furthermore FDA approved biocompatible polymer well suitable for pharmaceutical applications.[19] PEG-400 and PEG-2000 were employed for stabilization of nanovesicles. In a typical procedure a DMSO solution of compound **L5** (0.5mg in 0.5 mL) was rapidly injected into a deionized water containing PEG (0.6 g in 50 mL) under vigorous stirring for 5 minutes at RT. NVs PEGylated with polymer of lower molecular weight (PEG- 400) did not demonstrate high stability; however the use of PEG-2000 stabilized the vesicles up to 108 h. Even at that time point a significant amount of vesicles retained their structure, although their surface was not as smooth as it was at 24 and 48 hours. The size distribution of the NVs was in the range of <60nm to 130 nm; an insignificant amount of bigger vesicles (~250 nm) was also observed (*Figures 5.5a* and *b*).

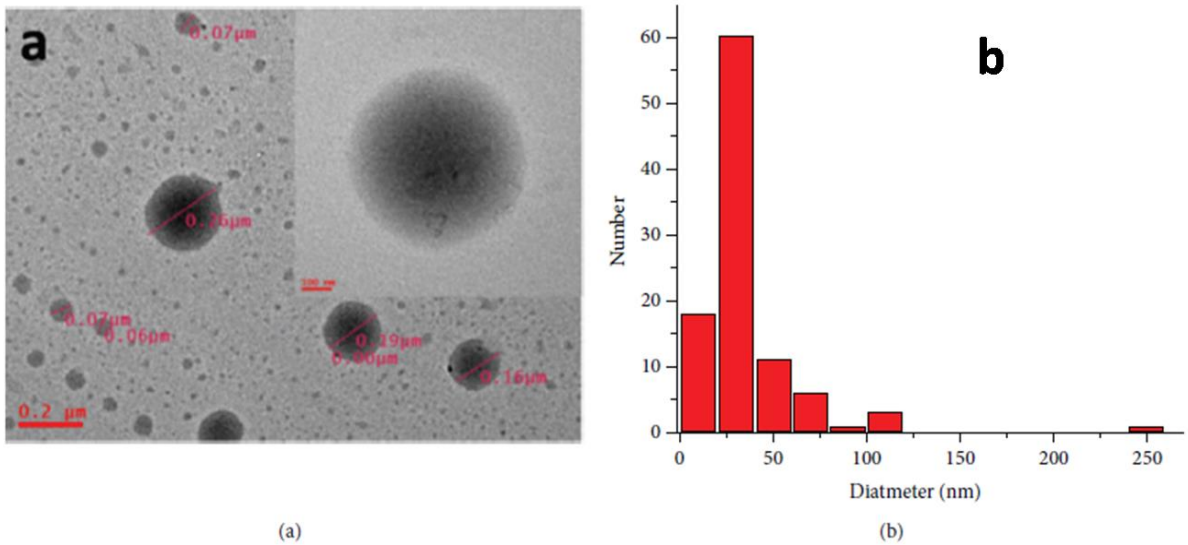

Figure 5.5: *(a) TEM micrograph image of nanovesicles stabilized by PEG-2000; (b) Size distribution histogram obtained for stabilized nanovesicles*

5.4.5.1 Synthesis of nanovesicles stabilized by PEG-400: Compound **L5** (0.5mg, 0.00063mmol) was dissolved in 0.5mL of DMSO and rapidly injected at vigorous stirring in 50 mL of deionized water, containing predissolved PEG-400 (0.6 g, 0.0003mmol). After 5 minutes of stirring at RT, solution was drop casted on silica and analyzed by TEM, AFM, and micro-Raman spectroscopy. Remaining solution was left at moderate stirring at RT for 120h, and sample was collected and analyzed every 24h.

5.4.5.2 Synthesis of nanovesicles Stabilized by PEG-2000:

The experiment was performed as described above; PEG-2000 was used instead of PEG-400.

5.4.6 Synthesis of TFN-loaded stabilized nanovesicles:

Stock solution of terfenadine (TFN) was prepared by dissolving 2mg of TFN in 1mL of deionized water. Compound **L5** (0.5mg, 0.00063mmol) was dissolved in 0.45mL of DMSO, mixed

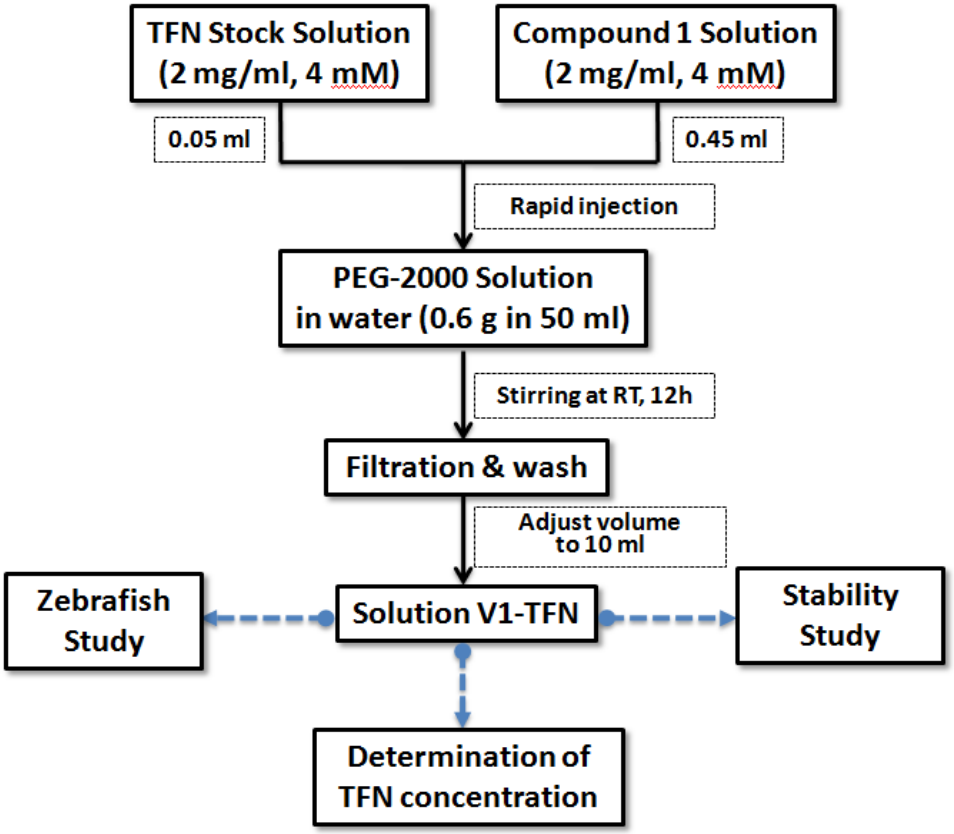

Figure 5.6*: Schematic representation of TFN-loaded nano-vesicles preparation*

with 0.05mL of TFN stock solution, and rapidly injected at vigorous stirring in 50mL of deionized water, containing predissolved PEG-2000 (0.6 g, 0.0003mmol). After 12 h of stirring at RT solution was filtered through syringe with hydrophilic syringe filter (Millipore, pores size 0.45 μm, hydrophilic, PVDF) to remove an excess of TFN and PEG-2000 and then vesicles were washed with deionized water and final volume was adjusted to 10mL (solution V1-TFN). This solution was used to identify concentration of TFN in vesicles, stability of drug loaded vesicles and for Zebrafish studies. See also schematic representation of the experiments mentioned below (*Figures 5.6 and 5.7*). TFN is known to heart beat of regularity in Zebrafish.[20]

5.4.7 Determination of concentrations of TFN in surrounding media:

TFN concentration in solution resulting from leakage from the nanovesicles was investigated at different time points following procedure (*Figure 5.9*) described below: 1mL of solution V1-TFN was collected, filtered through hydrophilic syringe filter, and washed 1 time with 1mL of deionized water.

TFN was extracted from filtrate with diisopropyl ether; solvent was evaporated and remaining TFN was redissolved in 2mL of acetonitrile. Concentration of TFN in this solution was measured according to modified published procedure.[21, 22] TFN solution in acetonitrile (2 mL) was mixed with 2mL of DDQ solution (5 mg/mL). The colored species were generated and absorbance intensity was measured immediately at 457 nm and compared with calibration graphs, which were constructed by plotting the absorbance of the formed CT complexes versus the final concentration of the drug (μg/mL). This study was repeated for the samples collected every 24 h up to 120 h.

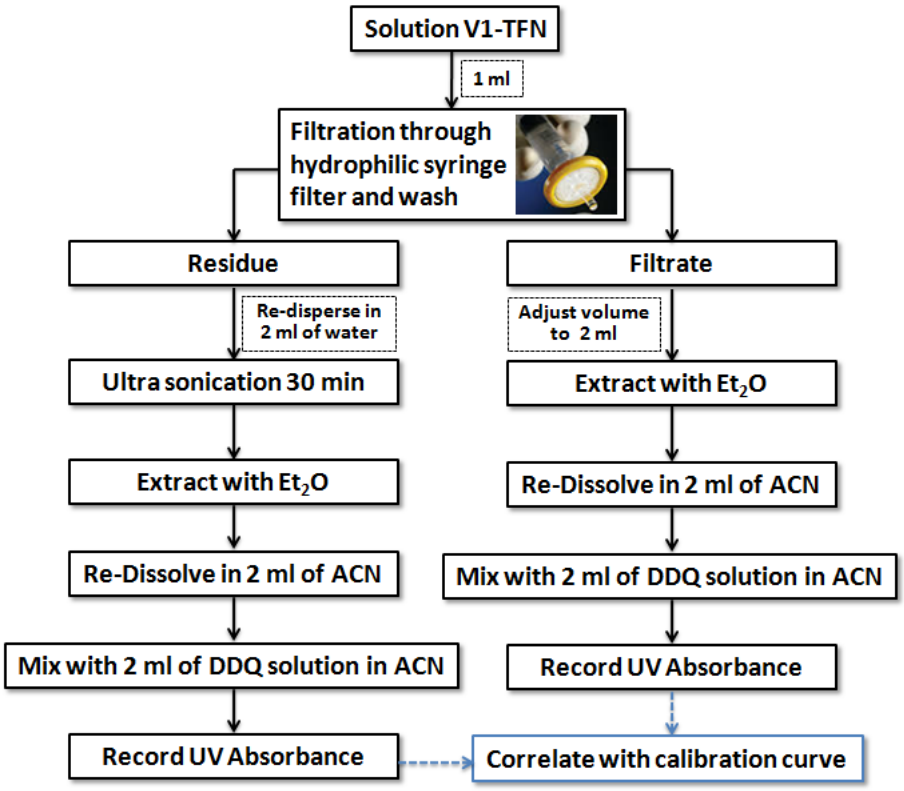

Figure 5.7: *Determination of TFN concentration inside vesicles and in surrounding media (repeated at different time points).*

5.4.8 Determination of concentrations of TFN inside nanovesicles:

Concentrations of TFN inside vesicles at different time points were investigated following procedure described below: 1mL of solution V1-TFN was collected, filtered through hydrophilic syringe filter, and washed 1 time with 1mL of deionized water to remove excess of the drug and PEG-2000, and residue was redispersed in 2mL of water and subjected to sonication for 30min at RT to break down all vesicles and release TFN. The ability of ultra sound to induce localized and controlled drug release from liposomes, synthetic diblock copolymers, and polymersomes is well

known phenomena.[23,24] Next, TFN was extracted from this solution with large volume of diisopropyl ether; solvent was evaporated and remaining TFN was redissolved in 2mL of acetonitrile. Replacement of solvent with ACN was necessary because it showed super priority over other solvents for the formation of CT complex, at the same time facilitating charge-transfer from donor to acceptor. Absorbance intensity of TFN solution in ACN was then measured at selected absorption maximum (457 nm) and obtained value was compared with values of calibration curve obtained using solutions of TFN:DDQ complex of known concentrations. The concentration of TFN calculated applying Beer-Lambert law was 37.5 μM, which allowed us to find out drug loading efficiency using the following equation.

$$\text{Loading Efficiency} = C_1/C_0 \times 100\% \longrightarrow \quad (1)$$

Where C_0 is an initial concentration of TFN in solution, whereas C_1 is concentration of TFN in vesicles after loading. This study was repeated for the samples collected every 24 h up to 120 h.

5.4.9 UV-Visible spectroscopy for determination of unknown drug concentration:

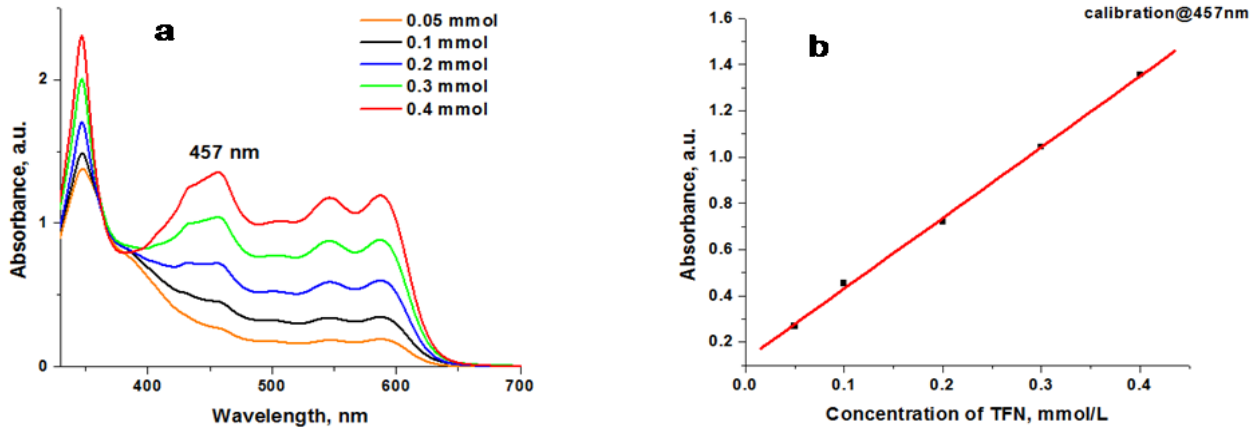

Figure 5.8*: (a) Absorbance of TFN at different concentrations in acetonitrile as CT complex with DDQ (DDQ concentration was maintained constant: 22mM for all samples) and (b) calibration graphs derived from (a) accordin to Beer-Lambert law.*

Determination of TFN concentration in biological samples is a challenging analytical task. Straightforward application of spectroscopic methods (for instance, measuring intensity of UV absorption and fluorescent emission) is not applicable as there is no correlation between obtained values and drug content. The majority of current reported methods (e.g., HPLC or NMR) lack sensitivity to measure the drug level at concentrations below 10 μg/mL. Hence spectrophotometric determination method based on the charge-transfer (CT) reactions of TFN with 2,3-dichloro- 5,6-dicyano-1,4-benzoquinone (DDQ) was opted. This technique is one of the simplest, rapid, and accurate methodologies developed till now. In this method, TFN acts as n-electron donor which forms a highly

colored charge transfer (CT) complex upon spontaneous reaction with strong π-acceptor DDQ. In order to implement this procedure and find out initial concentration of the drug loaded in vesicles, we have developed an in-house protocol (*Figures 5.8-5.9*). For unknown solution of drug TFN can also be determined by making CT complex with DDQ and measured absorbance at all-time points as depicted in figure. Comparing absorbance values at 457 nm with calibration curve in figure, the calculated drug loading e efficiency into the vesicles was ~35 ± 1%.

5.4.10 Stability of drug loaded nanovesicles:

In order to prove that there is no drug leakage from vesicles into surrounding media over time, we performed stability control experiment: drug-loaded vesicles were gently stirred at RT up

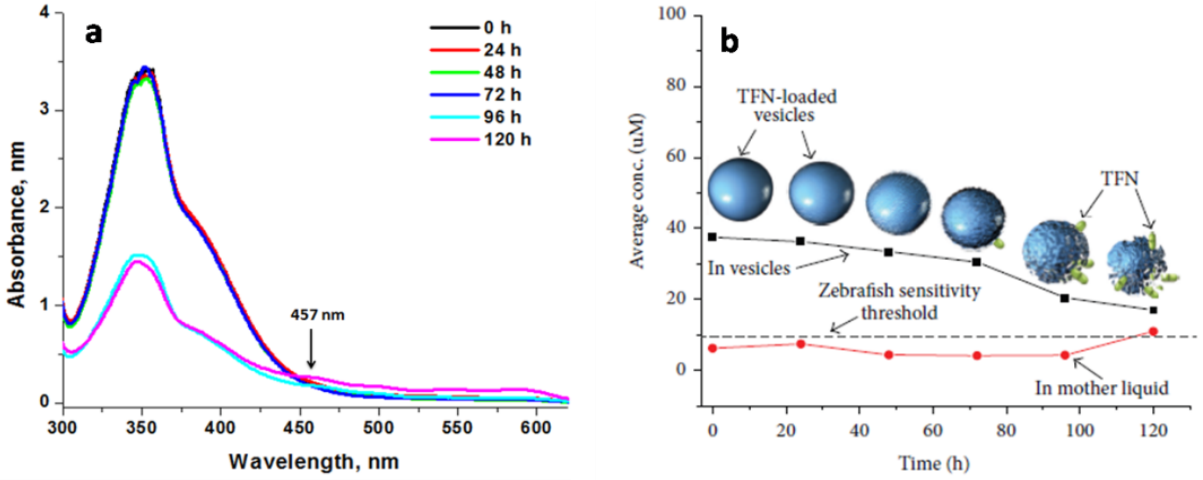

Figure 5.9: *(**a**) Absorbance of TFN:DDQ complex in acetonitrile at different time points (to determine concentration, the value of absorbance intensity at 457 nm was recorded and compared with value in calibration curve). (**b**) TFN concentration change inside vesicles and in mother liquid at different time points. Cartoon represents slow deformation of vesicles and TFN "burst" drug release after 72 h*

to 120 h, collecting sample every 24 h and detecting concentration of TFN inside vesicles and in mother liquid (solution collected prior to sonication) at every time-point as described in *Figure 7*. The experiment revealed that there is no major leakage observed up to 72 h (*Figure 5.9*) and concentration of TFN in media remains below 10 μM, which is Zebrafish sensitivity threshold (fish development and heart beat are not affected below this concentration of TFN. Subsequently, drug burst release was observed after 72 h, when TFN concentration in mother liquid suddenly increased and crossed10 μM. Simultaneously, TFN concentration inside NVs decreased dramatically after 72 h. We assumed that slow dissolution of PEG coating resulted in deformation of NVs and sudden drug release. These data correlate well with TEM data recorded for vesicles at different time points. *Figures 5.10a* and b represent TEM images of the vesicles at 24 and 72 h, respectively.

At 24 h NVs have well-structured defined shape (*Figure 5.10b*), while at 72 h we observe degradation of NVs and decrease of NVs amount (*Figure 5.10b*). This explains well drug burst release after 72 h, an effect commonly seen in case of nano-/microsphere or nano-/microvesicles systems.[25, 26]

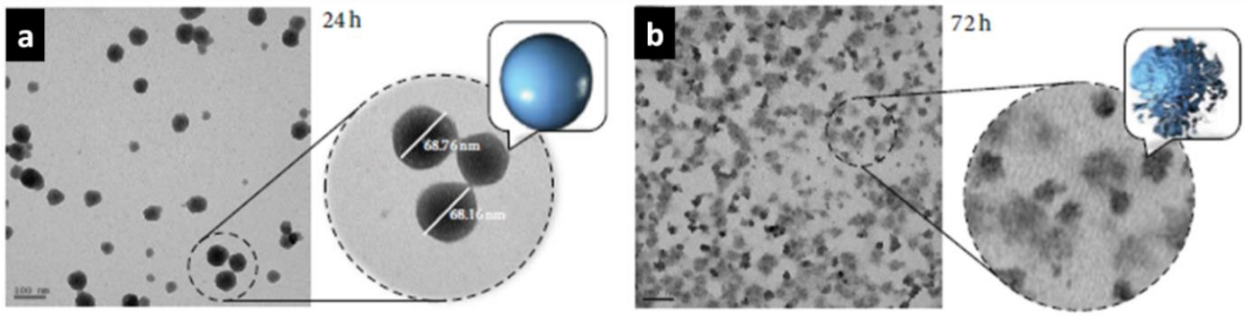

Figure 5.10*: TEM micrograph images of TFN-loaded nanovesicles (**a**) at 24 h; scale bar is 100 nm; (**b**) at 72 h; scale bar is 100 nm; cartoon shows vesicles deformation over time.*

5. 4. 11 Protocol for Zebrafish treatment with TFN-loaded nanovesicles:

For TFN-NV assessment, 3 dpf (days post fertilization) larvae were distributed in 24-well plate along with 250 μL of 0.1% DMSO solution. Each well contained 6 embryos with various treatments and the larvae were observed at time points of 24 h, 48 h, and 72 h. Embryos were then treated with different concentrations of TFN loaded micro vesicles (5 μM, 10 μM, 20 μM, and 40 μM). TFN alone at 20 μM concentration was used as a positive control and 0.1% DMSO was used as a negative control. The embryos were incubated in 24-well plate and atrial and ventricular rates were observed at different time points after treatment. All embryos were observed for mortality arising out of effect of TFN. Results of Zebrafish embryo toxicity study are summarized in Table 5.1.

5.4.12 Sustained Drug Delivery of TFN-Loaded Nanovesicles in Zebrafish Larvae:

Zebrafish larvae were treated with TFN loaded nanovesicles (TFN-NV) at four different concentrations (5 μM, 10 μM, 20 μM, and 40 μM of TFN) and were observed at the time points of 24h, 48h, and 72h to investigate mortality caused by TFN after drug treatment (*Figure 5.11*). TFN alone at a concentration of 20 μM was used as positive control. The observations showed that all larvae in positive control (TFN alone, 20 μM) died within 12 h. For larvae exposed to TFN-NV at low concentrations (5– 10 μM) first cases of mortality (and therefore drug effect) were observed at 24 h. Concentration can be based on the fact that the TFN-NV at 40 μM form aggregates (*Figure 5.11b*) and therefore might not enter the systemic circulation in the larval Zebrafish; however by 72 hours TFN-NV would release all TFN causing late mortality. Vesicles stability study and TEM data (*Figure*

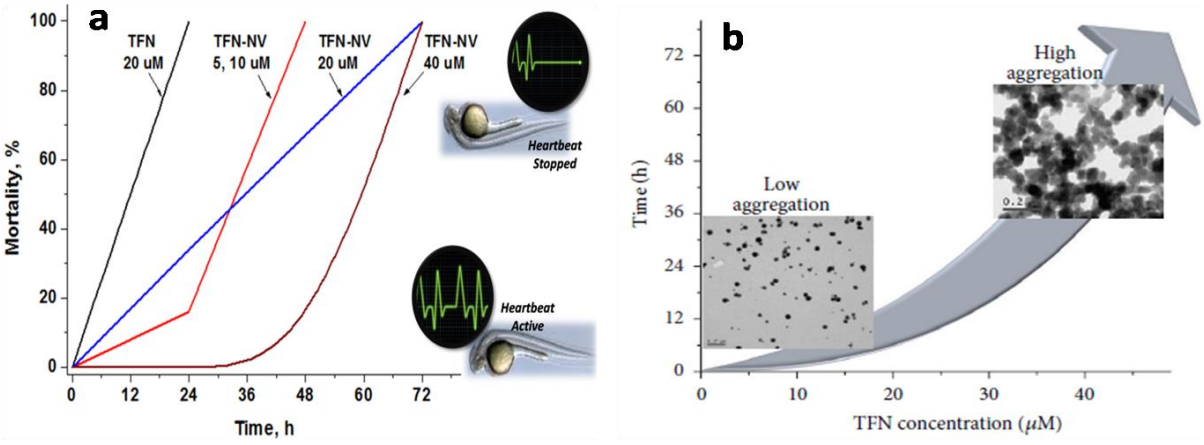

Figure 5.11: *(a) Percentage mortality in zebrafish larvae exposed to various concentrations of TFN-loaded nanovesicles (TFN-NV) at different time points; (b) Graphical representation of increased aggregation and therefore slow drug release depending on time and TFN concentration. Inserts show TEM micrographs of TFN-loaded nanovesicles; scale bar is 0.2 μM.*

5.10) support this explanation. Apart from that, we observed precipitation of nanovesicles from 40 μM solution if left undisturbed. The delayed mortality seen in other concentrations is suggestive of a sustained/delayed release of TFN from TFN-NV in vivo, which can be controlled by changing concentration of nanovesicles. As we did not observe major leakage of the drug from nanovesicles up to 72 h (the concentration of the drug in mother liquid was below Zebrafish sensitivity threshold), we conclude that effect of TFN below 72 h is observed only after the drug is released inside Zebrafish organism.

5.5 Conclusions:

Nontoxic and polymer stabilized organic nanovesicles as drug delivery cargoes are prepared from a novel bio inspired 2, 6-bispyrazolylpyridine derivative decorated with cytosine moieties. Spontaneous self-assembly of nanovesicles into “pearl-like” chains and subsequent fusion into nanotubes are investigated and protocol is developed to prevent pearling by protecting nanovesicles with biocompatible PEG-2000.Further the vesicles are loaded with terfenadine drug and successfully utilized to transport into zebrafish larvae and release the drug in sustained manner up to 72 h. Although polymeric or block copolymer based vesicles are extensively explored for drug delivery applications, nanovesicles prepared from *small bioinspired organic molecule* were utilized for drug delivery for the first time. We demonstrated that TFN release in vivo at desired time point can be controlled by altering nanovesicles concentration. The mechanism of the drug release in vivo is a subject of separate study. Nevertheless, current experiment undoubtedly demonstrated possibility of nanovesicles application as sustained-release drug delivery system.

5.6 Synthetic procedures:

10, 10'-(1,1'-(pyridine-2,6-diyl) bis(1H-pyrazole-4,1-diyl)) bis(dec-9-yn-1-ol) (12): Compound **2** (0.5 g, 1.07 mmol), Pd $(PPh_3)_2Cl_2$ (0.075 g, 0.106 mmol), PPh_3 (0.050 g, 2.140 mmol), CuI (0.027 g, 1.44 mmol) were taken in a 100 mL two neck round bottom flask. To this solid mixture, High vacuum pump was applied through condenser for deoxynation. Subsequently, Solvents dry triethylamine (15 mL), 1, 4 Dioxane (3 mL) were added to this mixture under N_2 atmosphere. After five minutes 9-Dec-yn-1-ol (0.217 g, 1.41 mmol) was added and refluxed it for 8 hours under N_2 atmosphere at 80°C. The solvents were removed under reduced pressure and crude product was purified by column chromatography using 5% methanol/DCM. After washing the compound with diethyl ether, pure **3** was obtained as white solid (80% yield). ^{1}H-NMR (400 MHz, $CDCl_3$-d_1): δ = 8.6(S, 2H), 7.9 (m,1H), 7.8 (d,2H), 7.7 (s, 2H), 3.6 (m, -OCH_2), 2.4 (m,4H), 1.6 (m,12H), 1.4 (m, 12H) ppm. ^{13}C-NMR (100 MHz, $CDCl_3$): δ = 149.4, 144.6, 141.5, 129.0, 109.5, 106.5, 92.6, 70.6, 62.9, 32.7, 31.9, 29.7, 29.2, 28.8, 25.7, 22.6, 19.4ppm, FTIR (KBr disc; ν in cm^{-1}):

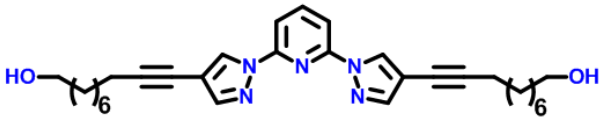

3616.86, 3398.88, 3146.18, 3055.52, 2928.21, 2851.05, 1726.45, 1601.06, 1481.46, 1497.1, 1402.38, 1354.15, 1265.42, 1219.12, 1186.33, 1055.16, 1028.15, 972.21, 952.92, 896.98, 864.19, 800.53, 738.80, 706.01,655.86. LCMS analysis m/z: experimental value: 515, calculated value =514.2, Anal. Calcd for $C_{31}H_{41}N_5O_2$: C, 72.20; H, 8.01; N, 13.58 Found: C, 72.36; H, 8.12; N, 13.49.

10, 10'-(1,1'-(pyridine-2,6-diyl) bis(1H-pyrazole-4,1-diyl)) bis(dec-9-yne-10,1-diyl) bis(4-methylbenzenesulfonate) (13): To the suspension solution of **3** (0.3 g, 0.58 mmol) in the mixture of

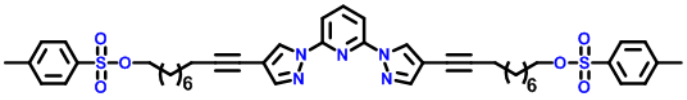

DCM (15 mL) and NEt_3 (5 mL), tosyl chloride (0.443 g, 2.32 mmol) was added. The reaction mixture was left for stirring about 2 hours at room temperature. All the solvents were evaporated under reduced pressure and crude was purified by column chromatography with EtOAc/hexane (2:8), Colorless solid compound was obtained (75% yield). ^{1}H-NMR (400 MHz, $CDCl_3$-d_1): δ = 8.5 (s, 2H), 7.9 (m, 1H), 7.8 (s, 4H), 7.7 (S, 2H), 7.3 (m, 4H), 4.0 (m, -OCH_2), 2.4 (S, 6H), 2.35 (m, 4H), 1.6 (m, 8H), 1.5 (m, 4H), 1.4 (m, 4H), 1.2 (m, 12H) ppm. ^{13}C-NMR (100MHz, $CDCl_3$-d_1): δ = 149.4, 144.6, 141.5, 133.2, 129.8, 128.9, 127.8, 109.6, 106.5, 92.5, 70.6, 28.9, 28.6, 25.3, 21.6, 19. 4 ppm. FTIR (KBr disc; ν in cm^{-1}): 3483, 3148, 3109, 3055, 2932, 2856, 1718, 1604, 1469, 1398, 1358, 1288, 1219, 1176, 1099, 1024, 951, 806, 777, 731, 661. LCMS analysis m/z: experimental value: 684.6,

calculated value =683.8, Anal. Calcd for $C_{45}H_{53}N_5O_6S_2$: C, 65.59; H, 6.48; N, 8.50; Found: C, 65.48; H, 6.42; N, 8.61.

2, 6-bis(4-(10-bromodec-1-ynyl)-1H-pyrazol-1-yl)pyridine (14): To the suspended solution of compound **4** (0.20 g, 0.242 mmol) in dry acetone was added Lithium bromide (0.0842 g, 0.970 mmol). After 2 hours, acetone was evaporated under reduced pressure and it was extracted with DCM solvent in water. After evaporation DCM solvent, compound **5** was obtained as white solid (89%yield). ^{1}H-NMR (400 MHz, $CDCl_3$-d_1): δ = 8.5 (S, 2H), 7.9 (m, 1H), 7.8 (d, 2H), 7.7 (S, 2H), 3.4 (m, -CH_2Br), 2.4 (m, 4H), 1.9 (m, 4H), 1.5 (m, 4H), 1.4 (m, 8H), 1.3 (m, 8H) ppm. ^{13}C-NMR (100MHz, $CDCl_3$-d_1): δ = 149.4, 144.6, 141.5, 129.0, 109.5, 106.5, 92.5, 70.7, 34.0, 32.7, 28.9, 28.8, 26.4, 19.4 ppm. FTIR (KBr disc; ν in cm^{-1}): 3437, 2924, 2854, 1720, 1651, 1599, 1481, 1390, 1101, 1014, 954, 800. LCMS analysis m/z: experimental value: 502, calculated value = 501.2, Anal. Calcd for $C_{31}H_{39}Br_2N_5$: C, 58.04; H, 6.13; N, 10.92 Found: C, 58.12; H, 6.17; N, 24.87.

N,N'-(1,1'-(10,10'-(1,1'-(pyridine-2,6-diyl)bis(1H-pyrazole-4,1-diyl))bis(dec-9-yne-10,1-diyl))bis(2-oxo-1,2-dihydropyrimidine-4,1 diyl)) diacetamide (L5):Acetyl cytosine in dry DMF (0.333g, 1.404 mmol) was taken in 100 mL round bottom flask. K_2CO_3 (0.258 g, 1.814 mmol) was added this solution to make a salt with –NH proton. After stirring at room temperature about 15 minutes, compound **5** was added. After reflux for 16 hours at 80°C, all DMF was removed by rotary evaporator under reduced pressure. Obtained crude was extracted with chloroform. Chloroform fraction was washed with 0.1MHCl (20 mL) and saturated NaCl solution (10 mL). Mixtures of compounds were observed after evaporation of chloroform. This was purified by silica column chromatography with 5% methanol/DCM. White solid was obtained (55% yield). ^{1}H-NMR (400 MHz, $CDCl_3$-d_1): δ = 10.4 (S, -NH), 8.5 (S, 2H), 7.9 (m, 1H), 7.8 (d, 2H), 7.7 (S, 2H), 7.6 (d, 1H), 7.4 (d, 1H), 3.8 (m, -NCH_2), 2.4 (m, 4H), 2.3 (S, 6H), 1.7 (m, 4H), 1.5 (m, 4H), 1.4 (m, 16H) ppm. ^{13}C-NMR (100 MHz, $CDCl_3$-d_1): δ = 171.3, 162.8, 155.7, 149.4, 148.8, 144.6, 141.5, 129.0, 109.5, 106.9, 96.7, 92.5, 70.6, 51.1, 36.5, 31.4, 29.7, 28.9, 26.4, 24.8, 21.2, 19.4 ppm. : 3325, 3136, 2926, 2852, 1697, 1662, 1556, 1479, 1429, 1381, 1307, 1219, 1178, 1028, 952, 866, 800, 655, 617. LCMS analysis m/z: experimental value: 785.93, calculated value = 786.40, Anal. Calcd for $C_{43}H_{51}N_{11}O_4$: C, 65.71; H, 6.54; N, 19.60 Found: C, 65.86; H, 6.51; N, 19.51.

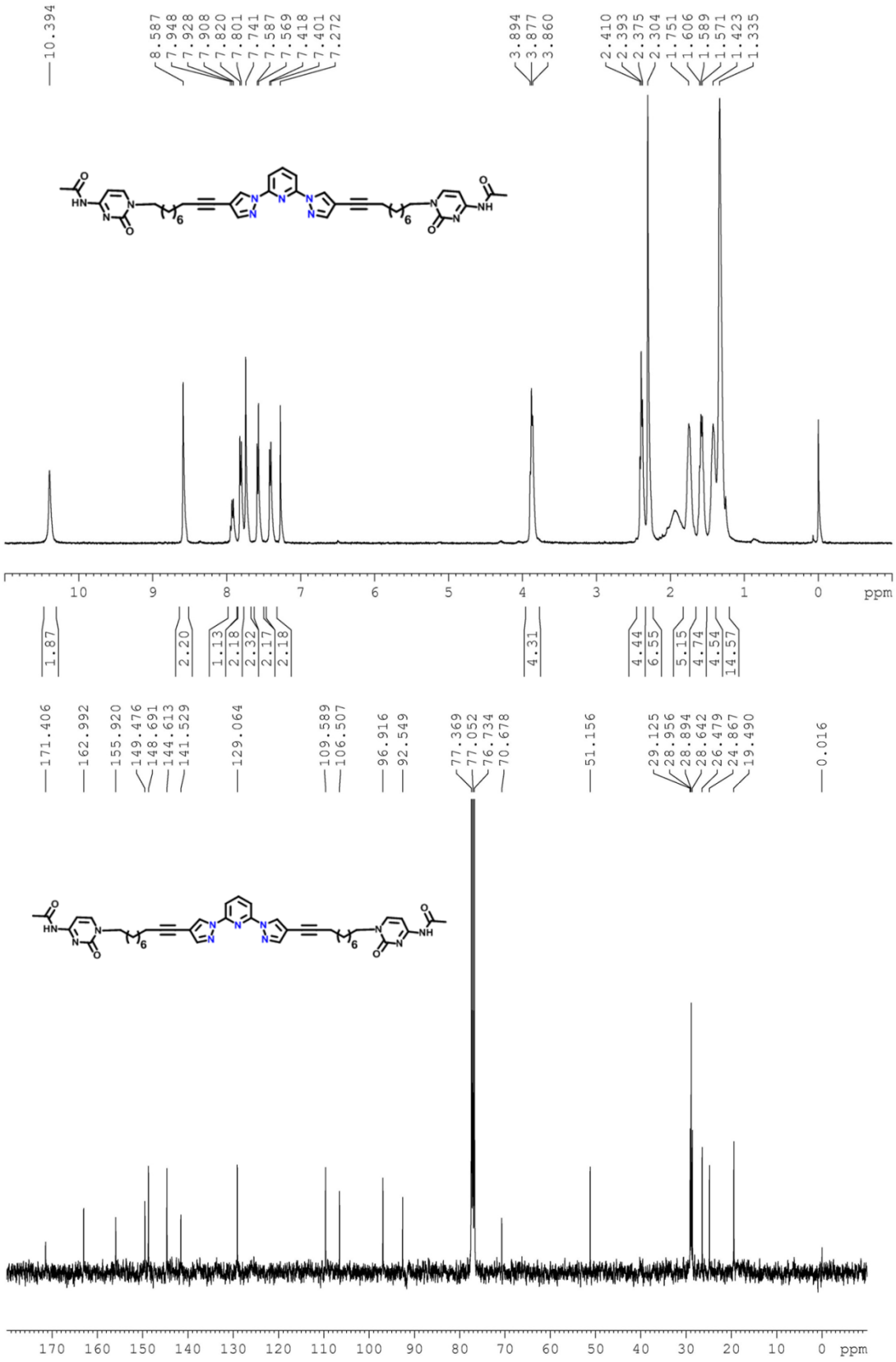
10.394
8.587
7.948
7.928
7.908
7.820
7.801
7.741
7.587
7.569
7.418
7.401
7.272
3.894
3.877
3.860
2.410
2.393
2.375
2.304
1.751
1.606
1.589
1.571
1.423
1.335
ppm
1.87
2.20
1.13
2.18
2.32
2.17
2.18
4.31
4.44
6.55
5.15
4.74
4.54
14.57
171.406
162.992
155.920
149.476
148.691
144.613
141.529
129.064
109.589
106.507
96.916
92.549
77.369
77.052
76.734
70.678
51.156
29.125
28.956
28.894
28.642
26.479
24.867
19.490
0.016
ppm

Display Report

Display Report

Analysis Info

Analysis Name	D:\Data\2012\Dr.R.C\JAN\BPP2CYTAC.d	Acquisition Date	1/2/2012 12:57:08 PM
Method	tune_wide_Pos.m	Operator	UOH
Sample Name	BPP2CYTAC-DCM-MeOH	Instrument	maXis 10138
Comment			

Acquisition Parameter

Source Type	ESI	Ion Polarity	Positive	Set Nebulizer	0.3 Bar
Focus	Not active	Set Capillary	3800 V	Set Dry Heater	180 °C
Scan Begin	50 m/z	Set End Plate Offset	-500 V	Set Dry Gas	4.0 l/min
Scan End	2500 m/z	Set Collision Cell RF	2500.0 Vpp	Set Divert Valve	Source

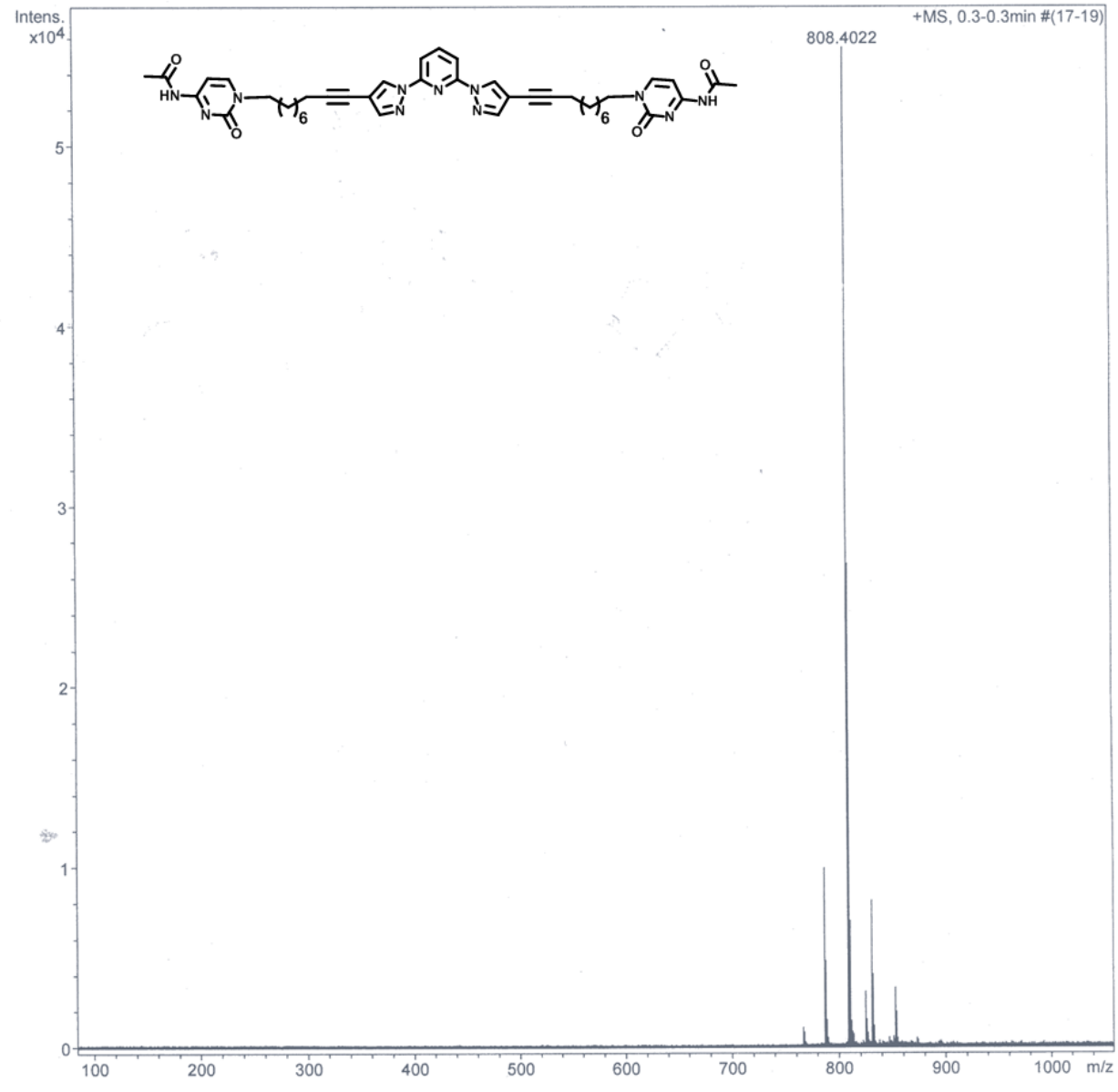

FLASH EA 1112 SERIES CHN REPORT
SCHOOL OF CHEMISTRY
UNIVERSITY OF HYDERABAD

Method filename:	E:\Program Files\Thermo Finnigan\Eager 300 for EA1112\DATA\Sys_data_ex
Sample ID:	BPP2CYTAC (# 17)
Analysis type:	UnkNown
Chromatogram filename:	UNK-13082013-17.dat
Sample weight:	1.121

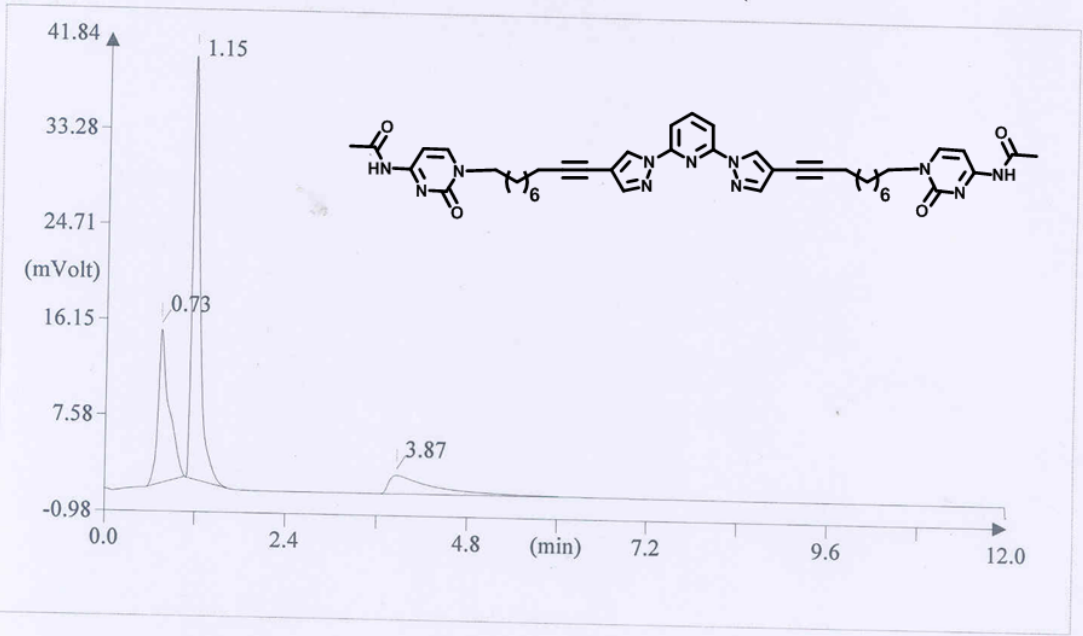

Element Name	Element %	Ret. Time
Nitrogen	19. 51	0. 73
Carbon	65. 86	1. 15
Hydrogen	6. 51	3. 87

References:

1. Soussan, E.; Cassel, S.; Blanzat, M.; Rico-Lattes, I. *Angew. Chem.* **2009***, 48, 274-288.*
2. Farokhzad, O. C.; Langer, R. *ACS Nano*. **2009**, *3*, 16-20.
3. Langer, R. *Science*. **1990**, *249*, 1527–1533.
4. Zhao, F.; Ma. M. L.; Xu, B. *Chem. Soc. Rev*. **2009**, *38*, 883–891.
5. Du, J.; OReilly, R. K. *Soft Matter*. **2009**, *5*, 3544-3561.
6. Sahoo, S. K.; Labhasetwar, V. *Drug Discov. Today*. **2003**, *8*, 1112–1120.
7. Duan*, Q.;* Cao*, Y.;* Li*, Y.;* Hu*, X.;* Xiao*, T.;* Lin*, C.;* Pan*, Y.;* Wang*, L. J. Am. Chem. Soc*. **2013**, *135*, 10542–10549.
8. Shi, D. *Adv. Funct. Mater*. **2009**, *19*, 3356–3373.
9. Kumar, G. P.; Rajeshwarrao, P. *Acta Pharm Sin B.* **2011**, *4*, 208–219,
10. Jang, S. C.; Kim, O. Y.; Yoon, C. M.; Choi, D. S.; Roh, T. Y.; Park, J. *ACS Nano*. **2013**, *7*, 7698–7710.
11. Gao, L.; Shi, L.; Zhang, W.; An, Y.; Liu, Z.; Li, G.; Meng, Q. *Macromolecules*. **2005**, *38*, 4548–4550.
12. Narayana, Y. S. L. V.; Chandrasekar, R. *Chem. Phys. Chem*. **2011**, *12*, 2391-2396.
13. Zoppellaro, G.; Baumgarten, M. *Eur. J. Org. Chem*. 2005, 14, 2888–2892.
14. Narayana, Y. S. L. V.; Basak, S.; Baumgarten, M.; Mullen, K.; Chandrasekar, R. *Adv. Fun. Mater*. **2013**, *23*, 5875-5880.
15. Khaled, E. *Talanta*. **2008**, *75*, 1167–1174.
16. Al-Majed, A. A.; Al-Zehouri, J.; Belal, F. *J. Pharm. Biomed. Anal.* **2000**, *23*, 281-289.
17. Schroeder, A.; Kost, J.; Y. Barenholz, Y. *Chem. Phys. Lipids*. **2009**, *162*, 1–16.
18. Pangu, G. D.; Davis, k. P.; Bates, F. S.; Hammer, D. A. *Macromol. Biosci*. **2010**, *10*, 546–554.
19. Banote, R. K.; Koutarapu, S.; Chennubhotla, K. S.; Chatti, K.; Kulkarni, P. *Epilepsy Behav.* **2013**, *27*, 212–219.
20. Westerfield, M.; *The Zebrafish Book. A Guide for the Laboratory Use of Zebrafish (Daniorerio)*. University of Oregon Press, Eugene, USA, 4th edition, **2000**.
21. Nakhi, A.; Rahman, M. S.; Seerapu , G. P. K.; Banote, R. K.; Kumar, K. L.; Kulkarni, P.; Haldar, D.; Pal, M. *Org. Bio. Chem*. **2013**, *11,* 4930–4934.
22. Panzica-Kelly, J. M.; Zhang, C. X.; Danberry, T. L.; Flood, A.; DeLan, J. W.; Brannen, K. C.; Augustine-Rauch, K. A. *Birth Defects Res B Dev. Reprod. Toxicol*. **2010**, *89*, 382–395.
23. Milton Harris, J.; Chess, R. B. *Nat. Rev. Dru. Discov*. **2003**, *2*, 214–221.
24. Basu, S.; Sachidanandan, C. *Chem. Rev*. **2013**, *113*, 7952–7980.

25. Reddy, E. R.; Banote, R. K.; Chatti, K.; Kulkarni, P.; Rajadurai, M. S. *Chem. Bio. Chem*. **2012**, *13*, 1889–1894.
26. Chan, P. K.; Lin, C. C.; Cheng, S. H. *BMC Biotechnology.* **2009**, *9*, article 11.

Chapter 6

Conclusions:

This thesis entitled **"Synthesis, Self-Assembly, Processing and Materials Aspects of 2, 6-(Bis-pyrazolyl-pyridine) Derivatives and Their Spin Crossover Compounds"** described the synthesis and characterizations of spin crossover (SCO) compounds appended to tridentate BPP ligand. The main aim of the thesis was to use these Fe(II) SCO materials and ligands to fabricate nano-vesicles, nano-tapes, nano-tubes and nano-rods using top-down and bottom-up nano-technological approaches. For this various BPP ligands were prepared. For example BPP unit carrying ligand and its SCO complex was used to prepare thiol (-SH) stabilized gold nanoparticles to study SCO effect through plasmonic propagation. Furthermore this thesis also focused on the preparation nano-drug carriers (vesicles) based on BPP ligand connected with acetyl cytosine nucleic base for drug loading and drug delivery in zebrafish model system.

Most of the metallo-supramolecular polymers are insoluble in common solvents, therefore Chapter 2dealt with the novel synthesis of highly soluble and solution processable SCO coordination polymer **1** with above room temperature SCO temperature at $T_{1/2} \sim 302$ K. Here, the octyl chains connected to BPP facilitated good solubility and enabled the self-assembly of **1** into isotropically distributed nano-tapes. Further lithographically controlled wetting technique was employed to fabricate well-aligned 1D array of SCO nanotapes from a THF/water solution of**1**.

Moreover the study of SCO effect was extended to describe the synthesis and characterization of organic nanorods (ONRs) coated by Fe(II) coordination nanoparticles formed through reverse micelle mechanism (Chapter 3). Both coordination nanoparticles and coordination polymers showed SCO with the change in the SCO curves due change in the chemical environment. Furthermore ONRs coated by coordination nanoparticles have shown passive waveguiding properties under the illumination of 488 nm argon laser, which had given a future possibility for the study of SCO in the nano level under light irradiation.

Furthermore a seven step synthetic protocol was made in chapter 4 to synthesize thiol stabilized Au NPs appended to BPP ligand (Chapter 4). Various shapes of NPs were synthesized like spherical, triangle and cubic with sizes ranging from ~1.3 nm to ~15 nm. Moreover rectangle micro stripes composed of thiol functionalized Fe(II) complex **10** was fabricated to make close proximity between NPs, which facilitate exploration of SCO effect in future via plasmon propagation under light irradiation.

In addition to SCO effect, the chemistry of BPP has been extended to biology to study terfenadine (TFN) drug assessment in zebrafish. In chapter 5, BPP connected with acetyl cytosine (**L5**) was prepared by four step synthetic protocol. Interesting nanostructures were achieved for **L5** such as nanovesicles, pearl like nanostructures and nanotubes. Since molecule **L5** is biologically non-toxic, nanovesicles protected by PEG were used as drug carrier. Consequently, TFN was incorporated polymer protected nanovesicles were used for drug assessment in zebrafish vivo. Zebrafish is a good model for drug assessment since its body function resembles with human, especially heart. Stability of drug encapsulated PEG-protected nanovesicles found to be 72 hours. The amount of drug encapsulated by nanovesicles was ~35 ± 1%.

Appendix A

Materials

Citrazinic acid	**Aldrich, 98%**
CuI	Avra synthesis Pvt. Ltd. 98%
(Pd(PPh3)4)	Aldrich, 99%
Tetramethyl ammonium chloride	Avra synthesis Pvt. Ltd. 98%
K-metal	Aldrich, 98%
Diglyme/ diethylene glycol dimethylether	Aldrich, 99.5%
KI	Merck chemicals Pvt.Ltd. 99%
I	Finar reagents, 99.5%
NaN3	Avra synthesis Pvt. Ltd. 98%
LiOH	Avra synthesis Pvt. Ltd. 98%
NaNO2	Merck chemicals Pvt.Ltd. 99%
POCl3	Avra synthesis Pvt. Ltd. 98%
PPh3	Avra synthesis Pvt. Ltd. 98%
(COCl)2	Avra synthesis Pvt. Ltd. 98%
Triflouro acetic acid	Aldrich, 99%
K2CO3	Avra synthesis Pvt. Ltd. 98%
2, 6-dibromo pyridine	Aldrich, 99.5%
cytosine	Avra synthesis Pvt. Ltd. 99%
HAu(III)Cl3	Aldrich, 99.5%
TOAB	Aldrich, 99.5%
NaBH4	Avra synthesis Pvt. Ltd. 98%
Fe(ClO4)2X H2O	Aldrich, 99.5%
Tosyl chloride	Finar reagents, 99.5%

Appendix B

Instrumentation

Nuclear Magnetic Resonance Spectroscopy:

^{1}H and ^{13}C NMR spectra were recorded on a Bruker 400 MHz NMR spectrometer. Spectra were recorded using the solvent peaks as the internal standard.

Mass Spectroscopy:

Shimadzu LC-MS 2010A equipment was used to record the mass spectra of the isolated compounds following atmospheric pressure chemical ionization (APCI) technique.

Elemental Analysis:

Elemental analysis was carried out on a Thermo Finnigan Flash EA-1112 series) CHNS analyzer.

Infrared Spectroscopy:

FT-IR spectra were recorded on a JASCO FT/IR-5300 or Nicolet 5700 FT-IR. Solid samples were recorded as KBr pellets.

UV-vis Absorption Spectroscopy:

Absorption spectra were recorded on a Shimadzu UV-3600 UV-Vis-NIR Spectrophotometer or Cary 100 Bio UV-Visible spectrophotometer.

Fluorescence Spectroscopy:

Steady state fluorescence emission and excitation spectra were recorded on a Jobin Yvon Horiba model Fluoromax-3 spectrofluorimeter.

Transmission Electron Microscopy:

Size and morphology of the shape-shifting nanostructures were examined by using a Philips XL30 ESEM Scanning Electron Microscope (SEM) using a beam voltage of 20 kV and a Tecnai G2 FEI F12 Transmission Electron Microscope (TEM) at an accelerating voltage of 200 kV. FESEM measurements were performed on a Hitachi S-4500 SE/N instrument operating at 20 kV. Carbon coated TEM grids (200 Mesh Type –B) were purchased from TED PELLA INC. USA.

Scanning Electron Microscopy: SEM and FESEM images were recorded on a Philips XL30 ESEM and a HITACHI S-4300SE/N FESEM respectively using beam voltages of 20 kV. The samples were fixed on aluminum platforms using carbon tapes; a conducting connection was made between

samples and aluminum platform by silver paint. Samples were coated with a thin layer (3 – 5 nm) of sputtered gold prior to imaging.

Atomic Force Microscopy (AFM):

AFM imaging was carried out on NT-MDT Model Solver Pro M microscope using a class 2R laser of 650 nm wavelength having maximum output of 1 mW. All calculations and image processing was carried out by a software NOVA 1.0.26.1443 provided by the manufacturer. The images were recorded in a semi-contact mode using a noncontact mode tip purchased from NT-MDT, Moscow. The dimensions of the tip are as follows: Cantilever length = 95 (±5) μm, Cantilever width 30 (±5) μm, and Cantilever thickness = 1.5-2.5 μm, Resonate frequency = 140-390 kHz, Force constant = 3.1-37.6 N/m, Chip size = 3.4×1.6×0.3 mm, Reflective side = Au, Tip height = 14-16 μm, Tip curvature radius = 10 nm, and Aspect ratio 3:1-5:1.

Thermogravimetric Analysis (TGA):

TGA of samples were carried out on a (Netzsch STA 409PC) TG-DTA instrument from 30 to 800 °C with a scanning rate of 10 °C/min.

Confocal Laser Scanning Microscopy:

The luminescence behavior of the samples was observed with a Leica Laser scanning confocal microscope, Germany [model No - TCS – SP2 (spectral confocal microscope)] equipped with an Acousto-Optical Beam Splitter (AOBS) emission filter. The wavelength and amplitude of the ultrasound can be changed (programmed) to deflect certain band of wavelength and its amount passing through the field to collect emissions in high efficiency. The topographic structural data were directly coupled with the spectroscopic properties of the specimen. The emission spectral curves were recorded in XYλ (spectral scan mode) scan mode, and the images were recorded in XYT mode (time scan mode). Argon-ion Laser (Power- 280 mW) was used as UV excitation source. Scanning was done by a 20.0X optical lens, later it was further magnified by a factor 3.45 using digital magnification by the Leica confocal software (LCS). The data were recorded with a (Continuous scan) scanning speed of 400 Hz (image lines per second) with a scan format of 512 pixel × 512 pixel resolution. The active emission colors were detected using the different color detection channels of the photomultiplier tube (PMT). The pinhole size was 36 μm and six frames were taken to make an average of the final frame.

Confocal Raman Micro Spectroscopy Studies: Raman spectra of the samples were recorded on a WI-Tec confocal Raman spectrometer equipped with a Peltier-cooled CCD detector. Using a 600

grooves/mm grating BLZ = 500 nm, the integration time was typically 2.0000 s. Ten accumulations was performed for acquiring a single spectrum. For imaging the integration time was typically 2.000 s, keeping in mind that the x or y resolution is ~250 nm four points per line and four line per image was taken for imaging of a 1 μm × 1 μm area. A He-Ne 633 nm or *Argon-Ion 488nm*laser was used as an excitation source for the Raman scattering.

Bulk Magnetic Studies:

The temperature dependent magnetic susceptibility of complexes in the powder state was measured on a Quantum Design vibrating sample magnetometer (VSM-SQUID) setup in the temperature range of 340 ↔ 2 K at continuous cooling (↓) and heating (↑) cycles with an applied direct current (DC) magnetic field of 0.5 T. Heating and cooling rate of the sample was kept at a 10 K interval in sweep mode.

Appendix C

RESEARCH PUBLICATIONS

1. **Botcha, A. K**.; Basak, S.; Chandrasekar, R. Lithographically oriented 1D nano-tape arrays composed of solution processable above room temperature spin cross-over iron(II) coordination polymers.
   RSC Advances, **2014**, *4*, 34760.
2. **Botcha, A. K**.; Dulla, B.; Reddy, E. R.; Chennubhotla, K. S.; Kulkarni, P.; Chadrasekar, R.; Rajadurai, M. S. Organic Nanovesicular Cargoes for Sustained drug Delivery: Synthesis, Vesicle Formation, Controlling pearling states and terfenadine loading/ Release studies, *Journal of Nanotechnolgy*, **2014**, ID 369139.
3. S. Basak, **Botcha, A. K**.; Md. T. Ansari, and R. Chandrasekar, Optical Waveguding organic Nano-Rods Coated with Reversily Switchable Fe(II) Spin Transition Nanoparticles. *Indian J Mater.Science.* **2013**, Article ID 136178.
4. **Botcha, A. K**, S. Basak, and R. Chandrasekar, Synthesis of gold nanoparticles stabilized by novel thiol functionalized Fe (II)complex to study Spin crossover effect through plasmonic propagation. **2015**, (Manuscript is in preparation).

PRESENTATIONS IN CONFERENCES AND SYMPOSIUMS

1. Botcha, A. K.; S. Basak, and R. Chandrasekar, Synthesis of gold nanoparticles stabilized by novel thiol functionalized Fe(II) complex to study Spin crossover effect through plasmonic propagation. Poster presentation at 3rd International conference at IIT Gauhati, November 2013.

2. Participant in Indian science congress local symposium held at University of Hyderabad, October 2014.

3. Botcha, A. K.; S. Basak, and R. Chandrasekar, Synthesis of gold nanoparticles stabilized by novel thiol functionalized Fe(II) complex to study Spin crossover effect through plasmonic propagation.

Poster presented in Chemfest-2013, 10th Annual In-House Symposium held at University of Hyderabad, Hyderabad, India.

4. Botcha, A. K.; Synthesis of gold nanoparticles stabilized by novel thiol functionalized Fe (II) complex to study Spin crossover effect through plasmonic propagation.

Delivered an oral presentation as well as a poster presentation in CHEMFEST-2014 held in University of Hyderabad, Hyderabad, India.

5. Participant in the first Indo-Taiwan symposium on recent trends in chemical sciences (RTCS) organized by school of chemistry, University of Hyderabad, November 17-18, 2014.